NTNU
Norwegian University of
Science and Technology

Fluid Structure Interaction Analysis of Abnormal Wave Slamming Events

Louise Ankerstjerne Rolland

Marine Technology
Submission date: June 2018
Supervisor: Jørgen Amdahl, IMT
Co-supervisor: Hagbart Alsos, Sintef Ocean

Norwegian University of Science and Technology
Department of Marine Technology

NTNU
Norges teknisk-naturvitenskapelige universitet
Institutt for marin teknikk

MASTER THESIS 2018

For

Stud. Louise Ankerstjerne Rolland

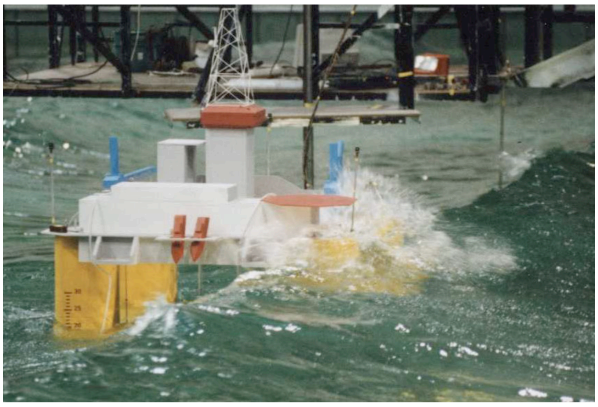

Fluid Structure Interaction Analysis of Abnormal Wave Slamming Events

Koplet væske-konstruksjonsresponsanalyse av abnormale bølgeslagshendelser

Following the COSL Innovator accident on the 30th of December 2015, the current industry practises for calculating air gaps and slamming loads on deck box in the case of negative air gap have been put under review. Platforms with negative air gap, i.e. the distance between wave crest and bottom of steel, may experience large loads due to wave impacts. Common practise is to use linear diffraction analysis combined with model tests in order to determine the loads.

Recent model tests have revealed that also the impact loads on the columns from breaking, or near breaking, waves are significant and possible considerably higher than what is indicated in the relevant rules and regulations. The loads are characterized by short durations, large spatial variations and high values, which put the measurement system at a considerable stress. Further, the interpretation of the test results is challenging for several reasons:

- Froude scaling may not be appropriate
- Large fluctuations in the measurements may indicate a dynamic load (possibly entrapped air), or unforeseen dynamic responses in the measurement system
- The statistical distributions of the extreme loads are not well behaved or do possibly not follow a Gumbel distribution
- The measurement systems used in experiments have so far have only been representative for and *elastic* structural response with small deformations. Are they also relevant for abnormal slamming actions, where the response will be *elasto-plastic* with large deformations?

In spite of the challenges above, the model test results are at this stage the best there is. Currently there is a push from both the industry and the academia to resolve the uncertainties, but it is likely that any results will not be available in the short term.

Traditional design, accompanied with traditional analyses, will not be sufficient to prove that the semi columns will be able to withstand the measured wave impact loads. As such, the work should focus on local structural integrity/capacity of the column designs for a semi-submersible subject to slamming loads from breaking waves. Non-linear structural analyses shall be performed in order to investigate the structural capacity for different slamming loads with different horizontal and vertical extent, duration and slamming pressure. Variations to the global design (column width, square vs. round), as well as local design (girder spacing, plate thickness etc) may be studied.

The purpose of the project thesis is to investigate the theory and established engineering practise for how to conduct dynamic response of a stiffened plated vertical surface on a floating platform and to familiarize with nonlinear finite element analysis the response to slamming loads.

The project work is proposed carried out in the following steps:

1. Drop tests with stiffened panels revisited. Perform static analysis of the panel subjected to uniformly distributed load and prepare static pressure–deformation curves. Compare with the results obtained with simplified methods, refer Yu et.al.: *Large inelastic deformation resistance of stiffened panels subjected to lateral loading* J. of Marine Structures, 2018. Evaluate what the current shell boundary conditions imply from a beam point of view. It is of interest that stress resultant histories for stiffener and associated plate flange can be established. Identify the bi-axial membrane stress state for the plating also show the effect of transverse membrane stresses may be taken into account the beam type formulations.

2. Using the static pressure-deformation resistance curve, calculate the maximum deformation using a one degree-of-freedom (1 DOF) analogy similar to that used for blast loads, refer NORSOK N-004 App.A /DNV-GL RPC204. Propose any modification that could improve the accuracy of the results using the 1 DOF analogy.

3. Investigate if elastic initial conditions for slamming (breaking) wave (profile and kinematics) can be established for integrated analysis with LS-DYNA. If this is found possible perform introductory studies for a stiffened panel.

4. Investigate if simple panel drop test can be conducted in SINTEF Ocean laboratories. If yes, prepare a plan for the tests, required instrumentation etc. Perform numerical analysis of the tests and compare with laboratory results.

5. Perform further studies of the response of stiffened panels subjected to drop tests or slamming loads depending on the results of pt. 3. Special emphasis shall be placed on realistic modelling of boundary conditions, which may be varied.. The panels shall be representative of platform columns/decks that may be subjected to slamming loads. It is expected that the basic panels will be taken into the large deformation range The strength of the stiffeners may be varied by varying size or span. For all cases compare results with those obtained with simplified methods. What values should be adopted for the added mass according to the simulations and theory when the panels undergo large deformations?

6. Discuss the results of the simulations from a 1 DOF perspective. How can pressure-time

histories (impulses) from hydro-elastic tests/simulations (ULS) be used in ALS design, i.e. hydro-elasto-plastic response?

7. Simulate slamming events (drop tests or breaking wave) for a relatively large section of a stiffened column. Dimensions to be determined in collaboration with the supervisors. Compare the results with 1 DOF models.
8. On the basis of the experience obtained during the master thesis work, prepare a procedure that may be used to check the design of stiffened panels in the accidental limit state (ALS)
9. Conclusions and recommendations for further work.

Literature studies of specific topics relevant to the thesis work may be included.

The work scope may prove to be larger than initially anticipated. Subject to approval from the supervisor, topics may be deleted from the list above or reduced in extent.

In the thesis the candidate shall present his personal contribution to the resolution of problems within the scope of the thesis work.

Theories and conclusions should be based on mathematical derivations and/or logic reasoning identifying the various steps in the deduction.

The candidate should utilise the existing possibilities for obtaining relevant literature.

The thesis should be organised in a rational manner to give a clear exposition of results, assessments, and conclusions. The text should be brief and to the point, with a clear language. Telegraphic language should be avoided.

The thesis shall contain the following elements: A text defining the scope, preface, list of contents, summary, main body of thesis, conclusions with recommendations for further work, list of symbols and acronyms, references and (optional) appendices. All figures, tables and equations shall be numerated.

The supervisor may require that the candidate, in an early stage of the work, presents a written plan for the completion of the work. The plan should include a budget for the use of computer and laboratory resources, which will be charged to the department. Overruns shall be reported to the supervisor.

The original contribution of the candidate and material taken from other sources shall be clearly defined. Work from other sources shall be properly referenced using an acknowledged referencing system.

The report shall be submitted in two copies:
- Signed by the candidate
- The text defining the scope included
- In bound volume(s)

- Drawings and/or computer prints which cannot be bound should be organised in a separate folder.

Supervisor:
Prof. Jørgen Amdahl

Co-supervisors
Post Doc Zhaolong Yu
SINTEF OCEANS: Bjørn Christian Abrahamsen
Hagbart S.Alsos

Deadline: June 11, 2018

Trondheim, January 15 2018

Jørgen Amdahl

Jørgen Amdahl

Preface

The following work is a master thesis in Marine structures as a part of the MSc in Marine Technology at NTNU during the spring semester of 2018. The thesis is a continuation of the project thesis on the same topic written during the autumn semester in 2017.

Although the specialisation of this master thesis is in Marine structures, the topic of slamming impacts should be studied from both a structural and hydrodynamic point of view. It has been enjoyable and challenging to combine both aspects of the problem in this thesis. It has also been very interesting to perform the slamming experiments in cooperation with Sintef Ocean. The experimental drop test provided insights to the slamming phenomenon that would be challenging to obtain from the numerical simulations and simplified methods alone. The experimental tests were carried out as a part of the SLADE: Slamming Loads in Structural Design - project with Sintef Ocean.

Trondheim 22.06.2018

Louise Rolland

Louise Rolland

Acknowledgement

de Firstly, I would like to thank my supervisor Jørgen Amdahl for excellent guidance and motivation during this semester. The discussions and suggestions for the master thesis have been essential for the thesis, and are much appreciated.

I would also like to thank Hagbart Alsos and Bjørn Abrahamsen at Sintef Ocean for their guidance and enthusiasm for the slamming impact experiments. The advice concerning the hydrodynamic aspects of the fluid-structure interaction was especially helpful.

Furthermore, I would like to thank Zhaolong Yu for useful discussions during the guidance meetings, and also for good help with the LS-Dyna software and the Vilje cluster.

In addition, I want to thank Egil Fagerholt at SIMLab for his help with post procession of the results from the DIC field measurements from the experimental drop tests.

Summary

In critical sea states, slamming wave loads may cause severe structural damage to marine structures. The slamming loads are associated with fluid-structure impacts with high pressures and short durations. The structural components subjected to the abnormal slamming loads may undergo large plastic deformations.

Previous model tests of slamming impacts have focused on the elastic structural response, or the pressure variation on rigid structures. There is a lack of experimental data for elasto-plastic response with large deformations. Experimental data is crucial for verification of numerical simulations and theoretical models. In this master thesis, a combination of experimental, numerical and theoretical methods has been applied to investigate abnormal wave slamming events. Drop tests with a panel that falls though air and impacts the water have been used to represent the slamming phenomenon.

Drop tests of unstiffened aluminium plates have been performed in the Ocean Basin Laboratory and simulated in the finite element software LS-Dyna. The drop tests were performed at different drop heights with a deadrise angle of 0 or 4 degrees. Drop tests with identical impact conditions had a small scatter in the displacements and the the deformation pattern of the plate. Digital image correlation, henceforth DIC, was used to measure the instantaneous response of the plate field during the impact. Although the DIC technique had previously not been applied to the fluid-structure interaction problem, the DIC measurement was successful.

The simulations of the experimental drop tests in LS-Dyna compared well with the DIC measurements. The response coincided well during the first part of the impact, but the numerical simulations did not exhibit the same elastic recovery in the plates as measured by DIC. In conclusion, LS-Dyna has proven to be an useful tool for the simulation of the slamming impact event.

Simplified methods were applied to establish the resistance curve and the maximum plate deflection due to slamming loads on a stiffened steel plate. The simplified resistance curves underestimated the deformation capacity of the plate for materials with hardening and large membrane effects. The estimation of the maximum response from established engineering practice agreed well with the numerical estimations from LS-Dyna. In conclusion, the simplified methods were useful for quick assessments of the capacity and response of the stiffened panel, but should be validated with numerical simulations and, if available, experimental data.

Sammendrag

I ekstreme sjøtilstander kan bølgeslag føre til store lokale deformasjoner i marine konstruksjoner. Lastene fra bølgeslagene er forbundet med voldsomme væske-struktur interaksjoner med høyt trykk og kort varighet. Komponentene som treffes av ekstreme bølgeslag forventes å gjennomgå store plastiske deformasjoner.

Tidligere modellforsøk med bølgeslag har hovedsakelig vært rettet mot elastisk konstruksjonsrespons og trykkvariasjon på stive konstruksjoner. Det er derfor en mangel på eksperimentell data for elasto-plastisk respons fra bølgeslag. Data fra modellforsøk er nødvendig for verifisering av numeriske simuleringer og analytiske metoder. I denne masteroppgaven har modellforsøk, numeriske elementberegninger i LS-Dyna og teoretiske metoder blitt brukt for å estimere konstruksjonsrespons fra bølgeslag. Selve bølgeslaget har blitt forenklet til en «dropp test» hvor en plate med en gitt starthastighet faller gjennom luft og treffer vannets overflate.

Dropptester med ustivede aluminiumsplater har blitt utført i Havbassenget på NTNU. Modellforsøkene har deretter blitt gjenskapt i elementmetode programvaren LS-Dyna. I modelltestene ble aluminiumsplaten sluppet fra forskjellige høyder med 0 og 4 graders vinkel mot vannoverflaten. Platene med identiske startbetingelser hadde en veldig liten spredning i deformasjon. Digital bildekorrelasjon, DIC, ble benyttet for å måle deformasjonen av aluminiumsplaten gjennom hele sammenstøtet. Forskjellenene mellom DIC-målinger og manuelle målinger av permanente deformasjoner var neglisjerbare. Plateresponsen fra simuleringene i LS-Dyna og DIC stemte godt overens. Disse deformasjonen var spesielt sammenfallende i starten av bølgeslagstøtet, men responsen fra LS-Dyna hadde ikke den samme elastiske avlastningen som målt ved DIC. I denne oppgaven har LS-Dyna vært et nyttig verktøy for å estimere konstruksjonsresponsen fra bølgeslagene.

Forenklede metoder har blitt anvendt for å etablere motstandskurver og for å finne den maksimale platenedbøyningen i en stivet plate som følge av krefter fra bølgeslag. De forenklede motstandskurvene undervurderte deformasjonskapasiteten til platen for materialer med fastning og store membraneffekter. Beregningen av maksimal respons stemte godt overens med den største plateresponsen fra LS-Dyna. De forenklede metodene som har blitt brukt i denne oppgaven var nyttige for en rask vurdering av platekapasitet og respons, men bør verifiseres med data fra elementmetodesimuleringer og modellforsøk.

Contents

Preface i
Acknowledgement ii
Summary iii
Sammendrag iv
Nomenclature xvi

1 Introduction **1**
1.1 Background 1
1.2 Objectives 2
1.3 Literature Review 2
    1.3.1 State of the Art 2
    1.3.2 Rules and Guidelines for Estimation of Loads and Response 4
1.4 Limitations of the Report 5
1.5 Structure of the Report 5

2 Theory **7**
2.1 Slamming 7
2.2 Hydroelastic Structure Response 9
    2.2.1 Criteria for Hydroelastic Response 9
    2.2.2 Analytical Hydroelastic Calculations 11
2.3 Scaling of Model Tests 12
    2.3.1 Scaling Factors 12
    2.3.2 Non-Dimensional Scaling 13
2.4 Structural Response Analysis 14
    2.4.1 Categorisation of Loading Domains 14
    2.4.2 Yield Line Mechanism 16
    2.4.3 Resistance Model for Stiffened Plate Subjected to Lateral Loads 17
    2.4.4 Single Degree of Freedom Analogy 20
    2.4.5 Added Mass for Rectangular Plates 22
2.5 Material Behaviour 24

2.5.1 Calibration of Stress-Strain Curves from Tensile Tests 24
2.5.2 Nonlinear Material Parameters from RP C208 24
2.5.3 Strain Rate Hardening 25
2.5.4 Johnson-Cook Constitutive Relation 25
2.6 Limit State Conditions 26
2.7 Background Theory for LS-Dyna 27
2.7.1 Arbitrary Lagrangian–Eulerian Formulation 27
2.7.2 ALE in LS-Dyna 27
2.7.3 Penalty Algorithm 28
2.7.4 Equation of State 29
2.7.5 Explicit Time Integration Scheme 30
2.7.6 Added Mass in LS-Dyna 30

3 Simplified Method for Deformation Resistance to Lateral Loads 31
3.1 Finite Element Model of Stiffened Panel 31
3.2 Material Selection 33
3.3 Parameters for Analytical Resistance Curve 34
3.4 Results from Static Analyses in LS-Dyna 36
3.4.1 Effect of Boundary Conditions and Plastic Material Properties 36
3.5 Discussion of Simplified Method 38

4 Drop Tests for 3D Stiffened Panels 41
4.1 ALE Formulation in LS-Dyna 41
4.2 Finite Element Model in Drop Test 42
4.3 Conduction of Drop Tests 44
4.4 Results from Numerical Simulations 45

5 Single Degree of Freedom Analogy for Drop Test Response 49
5.1 Beam Analogy for Stiffened Plate 49
5.2 Calculation of Added Mass for Rectangular Plate 50
5.3 SDOF Parameters from Analytical Resistance Model 51
5.4 SDOF Parameters from FEA Resistance Model 51
5.5 Response Calculation in Biggs Charts with SDOF analogy 52
5.6 Response for Drop Test with 0° Impact Angle 54
5.7 Response for Drop Test with 3° Impact Angle 55
5.8 Modified Biggs Response Charts 57
5.9 Discussion of Results 61

6 Studies of the Effect of Hydroelasticity and Limit State Conditions 63

6.1 Finite Element Model 63
6.2 Pressure Development 64
6.3 Drop Test Responses 65
6.3.1 Response with Hydroelastic Behaviour 65
6.3.2 Response from Rigid Pressure Impulse 66
6.3.3 Elasto-plastic Response from Elastic Pressure Impulse 67
6.4 Parameter Study on the Effect of Hydroelasticity 68
6.5 Parameter Study for ULS Prediction of ALS response 69
6.6 Discussion of Results 70

7 Experimental Drop Tests of Unstiffened Plates 73
7.1 Background 74
7.2 Objective 74
7.3 Scaling of the Experimental Model 75
7.4 Experimental Set-up 78
7.5 Test Conditions 82
7.6 Results from Drop Test Experiments 84
7.6.1 Deformations with 0° Impact Angle 84
7.6.2 Deformations with 4 ° Impact Angle 86
7.6.3 Results from DIC Measurements 88
7.6.4 Results from High-speed Underwater Camera 92
7.6.5 Accelerometer and pressure sensors 93

8 Drop Tests of Unstiffened Plate in LS-Dyna 95
8.1 Modelling of Water and Air 95
8.2 Material Calibration 96
8.2.1 Quasi-static Tensile Test 96
8.2.2 Calibration of Johnson-Cook Parameters 99
8.3 Finite Element Model 99
8.3.1 Convergence Tests 101
8.4 Drop Test Conditions 104
8.5 Results 105
8.5.1 Simulations in LS-Dyna 105
8.5.2 The Effects of Strain Rate Sensitivity in Johnson-Cook 109
8.5.3 Comparison of LS-Dyna and DIC Measurements 110
8.5.4 Deformation Profiles 112

9 Discussion 119

9.1 Experimental Drop Tests 119
  9.1.1 Effect of Impact Conditions and Measurement Techniques 119
  9.1.2 Scale Effects 120
  9.1.3 Effect of Initial Curvature from Thermal Expansion 121
  9.1.4 Effect of Entrapped Air 121
  9.1.5 Effect of the Dent in the Plate 122
9.2 Numerical Simulations of Experimental Drop Tests 122
  9.2.1 Limitation of LS-Dyna 122
  9.2.2 Simplification of Drop Test Impact 122
  9.2.3 Simplification of Material Formulation 124
  9.2.4 Effect of ALE formulation and Entrapped Air 124
9.3 Discussion of Design Procedure for Slamming Loads 125
9.4 Validation of Design Method 127

10 Conclusion and Recommendations for Further Work 129
10.1 Conclusion 129
10.2 Recommendations for Further Work 130
  10.2.1 Numerical Model in LS-Dyna 130
  10.2.2 Theoretical Methods 131

References I

Appendix IV

A Convergence tests for stiffened plate V

B Transformation Factors For Beams VII

C Stress-strain curves for steel S355 IX

D Parameter tests for unstiffened plate XI

E Tensile test specimens of A1050 H111 XIII

F Deformation profiles from LS-Dyna and Mitutoyo XV

List of Tables

2.1 Scaled parameters according to Froude's scaling law 13

2.2 EOS Gruneisen for aluminium, steel, water and air 30

3.1 Structural dimensions of the stiffened panel 32

3.2 Linear material properties of S355 steel 33

3.3 Plastic material properties of steel S355 33

3.4 Nonlinear material properties of steel S355 from (DNVGL, 2013) 33

3.5 Structural parameters for the deformation resistance of the stiffened plate response for clamped beam 35

3.6 Elastic response parameters from FEA static analysis 38

4.1 Material properties for water in LS-Dyna 42

4.2 Finite element discretisation of the stiffened drop test panel 43

4.3 Linear material properties for the dropped panel 44

5.1 Analytical resistance parameters in the elastic domain for the stiffened plate . . 51

5.2 Generalised mass and stiffness in elastic domain for the clamped beam in SDOF analysis 51

5.3 FEA resistance parameters in the elastic domain for the stiffened plate 51

5.4 Mass and stiffness for the clamped beam in SDOF analysis 52

5.5 Summary of the SDOF response from Biggs chart for the plate with FEA resistance model and $0t_d$ rise time 54

5.6 Summary of the SDOF response from Biggs chart for the plate with analytical resistance model and $0t_d$ rise time 54

5.7 Summary of the SDOF response from Biggs chart for the plate with FEA resistance model and $0.5t_d$ rise time 56

5.8 Summary of the SDOF response from Biggs chart for the plate with analytical resistance model and $0.5t_d$ rise time 56

5.9 Explanation of graphs in numerical Biggs charts in figure 5.9, 5.10 and 5.11 . . . 58

5.10 Summary of predicted maximum responses for the SDOF system with modified load curve and resistance curve in Biggs charts 61

6.1 Linear material properties for the dropped panel 64
6.2 Relative difference [%] between the responses with and without hydroelastic effects 69
6.3 Relative difference [%] between elasto-plastic responses due to a elastic or elasto-plastic pressure pulse 70

7.1 Scaling parameters for panel drop test 76
7.2 Model and full scale parameters scaled according to correct membrane capacity N_p 77
7.3 Test specifications for the different drop impacts 82
7.4 Maximum permanent out-of-plane deformations measured with dial gauge and Mitutoyo measuring equipment for plate impacts with zero deadrise angle 84
7.5 Maximum permanent out-of-plane deformations with dial gauge and Mitutoyo measuring equipment for plate impacts with 4 ° deadrise angle 86
7.6 Maximum and permanent plastic deformations measured by DIC 89

8.1 Material properties for water in LS-Dyna 96
8.2 Main dimensions of the test specimen 97
8.3 Linear material properties for the unstiffened plate 101
8.4 Summary of dimensions and finite element discretization for numerical drop test simulation with unstiffened plate 104
8.5 Calculated impact velocities from experimental drop test 104
8.6 Maximum deformations from drop tests simulated in LS-Dyna representing the experimental drop tests 105
8.7 Comparison between the maximum displacements predicted by LS-Dyna and measured by DIC cameras 110

List of Figures

2.1 Wave slamming loads on the COSL innovator rig 7
2.2 The formation of a plastic hinge for a simply supported beam from Megson (2005) 16
2.3 Plastic hinge line pattern in a fully clamped rectangular plate subjected to a uniformly distributed lateral pressure from Norman (1971) 16
2.4 Plastic resistance curve from Norsok Standard (2013) for different non-dimensional spring stiffness c 17
2.5 Beam collapse mechanism in the simplified model for a general loading condition 18
2.6 Biggs chart for a SDOF system subjected to a triangular load pulse with rise time $0.5t_d$ from DNVGL (2016a) 21
2.7 Non-linear resistance curve approximated by an equivalent tri-linear system DNVGL (2016a) 21
2.8 Added mass parameters for 3D rectangular plates in infinite fluid 23
2.9 Definition of true stress-true strain curve according to RP C208 (DNVGL, 2013) 25
2.10 Illustration of the penalty coupling algorithm from Aquelet et al. (2006) 29

3.1 Finite element model of stiffened plate used for the quasi-static pressure analyses in LS-Dyna 32
3.2 True stress-true strain curve for steel S355 with different nonlinear material properties 34
3.3 Coefficient for estimation of the effective flange $s_e = C_e s$ from RP C101 (DNVGL, 2015) 35
3.4 Static resistance-deformation curves from LS-Dyna for different plastic properties of steel compared with the resistance curve from the simplified formulation 36
3.5 Static resistance-deformation curves for different longitudinal boundary conditions 37

4.1 Convergence test for FSI drop test problem. Same elements size for master and slave elements . . . 43
4.2 Discretised model of stiffened plate used in the drop tests in LS-Dyna . . . 44
4.3 Pressure-time variation with 0° and 3° impact angle and velocity 11.19 m/s . . . 45
4.4 Lateral deformation pattern for elasto-plastic plate with 0° impact angle (left column) and 3° impact angle(right column) . . . 47
4.5 Maximum lateral plate deformation with 0° and 3° impact angle and velocity 11.19 m/s . . . 47
4.6 Pressure and response history for drop test with stiffened plate . . . 48
4.7 Von mises stress at 18 ms for stiffened plate with zero impact angle . . . 48

5.1 Resistance curve for the stiffened steel plate obtained from static analysis in LS-Dyna compared with a standard tri-linearisation of the resistance curves with $k_1 = 60$ MN/m . . . 53
5.2 Resistance curve for the stiffened steel plate obtained from the simplified approach compared with a standard tri-linearisation of the resistance curves with $k_1 = 91.5$ MN/m . . . 53
5.3 Triangular load pulse with $0t_d$ rise time fitted to drop test pressure-time history for the stiffened plate with 0° impact angle . . . 54
5.4 Biggs chart in RP C204 for dynamic response of a SDOF system subjected to a triangular load with $0t_d$ rise time . . . 55
5.5 Triangular load pulse with $0.5t_d$ rise time fitted to drop test pressure-time history for the stiffened plate with 3° impact angle . . . 55
5.6 Biggs chart in RP C204 for dynamic response of a SDOF system subjected to a triangular load with $0.5t_d$ rise time . . . 56
5.7 Modified tri-linear approximation to the theoretical and FEA resistance curve for the stiffened plate . . . 57
5.8 Modified "triangular" load history for the pressure history from the drop tests in LS-Dyna . . . 58
5.9 Biggs curves from Fortran for the dynamic response of a SDOF system equivalent to the drop test of a stiffened plate with 0 ° impact angle. FEA resistance curve is applied . . . 59
5.10 Biggs curves from Fortran for the dynamic response of a SDOF system equivalent to the drop test of a stiffened plate with 3 ° impact angle. FEA resistance curve is applied . . . 60
5.11 Biggs curves from Fortran for the dynamic response of a SDOF system equivalent to the drop test of a stiffened plate with 0 ° impact angle. Analytical resistance curve is applied . . . 60

6.1 Pressure variation on the stiffened steel plate with β = 0° and V = 11.19 m/s for different material response behaviour . . . 65
6.2 Maximum deflection for drop test of for stiffened plates with β = 0° and V = 11.19 m/s . . . 66
6.3 Structural response of stiffened panel with material density ρ_a subjected to a rigid load pulse . . . 67
6.4 Elasto-plastic response of stiffened panel with ρ_a subjected to an elastic load pulse . . . 67
6.5 Mid-plate deformations from drop test with the elasto-plastic stiffened plate with various impact conditions . . . 68
6.6 Surface plots of the mid-plate elasto-plastic deformation with and without hydroelastic effects for different deadrise angles and impact velocities . . . 69
6.7 The effect of impact angle and velocity for the prediction of ALS elasto-plastic response with ULS elastic load history . . . 70

7.1 Idealisation of a slamming load impact against the column of a semi-submersible to a drop test where the structure falls and impacts the calm water surface . . . 73
7.2 Examples of stiffened plates covering the hull and topside of offshore structures from SLADE (2018) . . . 75
7.3 Pictures of impactor, rigid steel box and aluminium plate from the drop test . . 78
7.4 Dimensions [cm] of the rigid impactor, rigid steel box, and flexible aluminium plate . . . 79
7.5 CAD-drawing of the drop test rig from SLADE (2018) . . . 79
7.6 Installed drop test rig at the "Trim-dokka" basin . . . 80
7.7 Illustration of the experimental set-up . . . 81
7.8 Installation of high-speed cameras for the drop test experiment . . . 81
7.9 Illustration of flat and inclined drop test impacts . . . 83
7.10 Equipment applied to measure the permanent lateral plate deformations . . . 83
7.11 Lateral plate displacement measured by Mitutoyo for drop tests with 0° impact angle . . . 85
7.12 Deformed aluminium plates from drop test experiment . . . 86
7.13 Lateral plate displacement measured by Mitutoyo for drop tests with 4° impact angle . . . 87
7.14 Contour shapes of the out-of-plane deformations for the aluminium plates from DIC field measurements. The changes in the speckle pattern have beem calibrated to a finite element mesh . . . 88
7.15 Deformation profiles from DIC and Mitutoyo . . . 89
7.16 Lateral deformation for drop test impacts with zero deadrise angle . . . 90

7.17 Lateral deformation for drop test impacts with 4° deadrise angle 90
7.18 Comparison of maximum deformation for drop test 12 with 0 ° impact angle and test 8 with 3 ° impact angle 91
7.19 Pictures taken by the underwater high speed camera for drop test 12 with zero deadrise angle and drop height 44.4 cm 92
7.20 Pictures taken by the underwater high speed camera for drop test 9 with 4° deadrise angle and drop height 44.4 cm 93
7.21 Acceleration and velocity derived from the accelerometers. T=0 ms refer to global time t=20.13 s 94

8.1 Tensile test samples nr. 1-6 of aluminium A1050 H111 with material 1 used in the tensile test 96
8.2 Main dimensions of the tensile test specimen 97
8.3 Engineering stress-strain curve calibrated from the tensile test 98
8.4 True stress - true strain curve calibrated from the tensile test 98
8.5 Calibration of Johnson Cook constitutive relation 99
8.6 Finite element model of impactor in LS-Dyna 100
8.7 Simplified finite element model of impactor in LS-Dyna 100
8.8 Convergence tests for the numerical model of the drop test with the unstiffened plate with $\beta = 0$ and V=3.8 m/s 102
8.9 Maximum out-of-plane deflection for drop tests with zero impact angle in LS-Dyna 106
8.10 Maximum out-of-plane deflection for drop tests with plates with 4 degree impact angle in LS-Dyna 107
8.11 Displacement of the inclined plate in drop test 8. The submersion of the plate is marked on the deformation curve 107
8.12 Comparison between *ALE single material and void* and *ALE multimaterial* formulation for drop test 3 in LS-Dyna 108
8.13 Maximum deformations for test 3 with Johnson Cook material formulation with various values for the strain rate sensitivity parameter C 109
8.14 Comparison of maximum lateral plate deflection from LS-Dyna simulations and DIC measurements for drop tests of plates with zero impact angle 111
8.15 Comparison of maximum lateral plate deflection from LS-Dyna simulations and DIC measurements for drop tests of plates with 4° impact angle 111
8.16 Deformation profiles from LS-Dyna and DIC for test 12 with drop height 44.4 cm and zero impact angle 112

8.17 Deformation profiles from LS-Dyna and DIC for test 12 in the xz-plane along the middle of the plate. The deformation profiles are plotted for the dotted time steps in figure 8.16 114

8.18 Deformation profiles from LS-Dyna and DIC for test 8 with drop height 44.4 cm and 4 ° impact angle 115

8.19 Deformation profiles from LS-Dyna and DIC for test 8 in the xz-plane along the middle of the plate. The deformation profiles are plotted for the dotted time steps in figure 8.18 117

A.1 Convergence test for static analysis of stiffened plate V

B.1 Transformation factors for a simply supported beam in SDOF system VII

B.2 Transformation factors for a clamped beam in SDOF system VII

C.1 Stress-strain curve for steel S355 according to DNV C208 t ≤ 16 mm IX

C.2 Stress-strain curve for steel S355 according to DNV C208 16 < t ≤ 40 mm IX

D.1 Variation of yield stress for aluminium plate with plate thickness t = 2 mm 4° impact angle XI

D.2 Variation of plate thickness for aluminium plate with σ_y = 40 MPa and 4° impact angle XII

E.1 Results from quasi-static tensile test from A1050 H111 Material 1 XIII

F.1 Deformation profiles in the xz-plane from simulations in LS-Dyna and measurements by Mitutoya XVI

Nomenclature

Abbreviations

ALS	Accidental limit state
DIC	Digital image correlation
DLF	Dynamic load factor
EOS	Equation of state
FEM	Finite element method
FE	Finite element
FSI	Fluid structure interaction
HS	High speed
OTG	Offshore technical guidelines
RP	Recommended practice
SDOF	Single degree of freedom
ULS	Ultimate limit state

Symbols

β	Impact angle

λ	Scaling factor
σ_y	Yield stress
σ_{ts}	Ultimate tensile strength
ξ	Non-dimensional hydroelasticity parameter
c	Non-dimensional translational stiffness
EI	Bending stiffness
F_{max}	Equivalent load amplitude of triangular pulse
k	Translational axial stiffness towards inwards motion
k_1	Elastic stiffness
M_p	Plastic moment capacity in pure bending
N_p	Membrane capacity
R	Lateral deformation resistance
R_o, R_{el}	Plastic collapse resistance in pure bending
t_d	Duration of impact
T_n	Eigen period
V	Impact velocity
w_{el}	Maximum elastic displacement
C, p	Strain rate hardening parameter
K, n	Power law parameters

Chapter 1

Introduction

1.1 Background

The slamming phenomenon is a highly nonlinear impact problem between water and structure. The violent impact between the slamming wave loads and the structure may induce severe local structural damage. In 2015 a steep, horizontal wave hit the deck box of the COSL innovator drilling rig operating in the North Sea. The slamming impact caused severe structural damage and one casualty. The accident shed light on the lack of accurate guidelines and requirements concerning events of horizontal, breaking waves on platforms.

Slamming loads are characterised with short durations and high peak pressures. The impact will commonly induce large plastic deformations to the structure, which means that the structural response should be handled with nonlinear theory. The large, nonlinear response will also affect the fluid flow surrounding the plate during the impact.

Depending on the required level of accuracy, experimental tests, numerical simulations and simplified methods can be applied to model the slamming impact problem. Experimental tests are among the best tools for modelling the slamming impact problem. However, to fully capture the effect of the local structural deformation, several gaps in the model test need to be tackled. So far, most experiments on slamming impacts have only been conducted for the elastic structural response. It is expected that the slamming impacts may cause large plastic deformations, and thus, experimental data for the plastic response should be available.

Numerical simulations may be a feasible option to the model tests. Contrary to experiments, the numerical codes allow for more flexibility, and are generally less time consuming. The finite element software LS-Dyna is well suited for nonlinear fluid-structure interaction problems, henceforth FSI, of short duration with high pressure and velocity gradients. Hence, LS-Dyna is a suitable software for simulation of slamming events. Simplified methods can provide a quick and realistic assessment of the structural response, which is especially valuable during the early design phase of the structural component. However, experimental data is still crucial for verification of both numerical codes and simplified methods.

1.2 Objectives

The main objective of this master thesis has been to investigate how simplified methods, numerical simulations and experiments can be applied to represent the slamming phenomenon. The focus has been directed towards finding the limitations of each of the different methods and how they correspond to each other.

In the first part of the thesis, the aim was to apply established simplified methods for estimating the dynamic response of a stiffened panel. The analytical estimations have been compared and validated with non-linear structural analyses in LS-DYNA where the slamming impact has been recreated as a drop test.

Due to the lack of available experimental data for the plastic response to slamming loads, the experiments aimed to perform slamming impacts causing large plastic deformations. The purpose of the model tests was to use the experimental data to validate the numerical simulations in LS-DYNA and to obtain a better understanding of the physical effects of the slamming phenomenon.

1.3 Literature Review

1.3.1 State of the Art

In the late 1920s, pioneering analytical studies on how to establish slamming loads for water entry problems were first initiated by Von Kármán (1929). The impact phenomenon was simplified to the water entry of a 2D rigid wedge impacting a calm water surface. The work of Von Kármán (1929) was later improved by Wagner (1932) to also account for the local uprising of water around the wedge and the details of the spray root.

In the 90s, the term *hydroelasticity* was introduced to describe the mutual interaction between the fluid flow and the structural response. Extensive research showed that the fluid flow was, given certain conditions, strongly influenced by the structural response, and vice versa. Hydroelastic modelling of slamming against wetdecks of steel and aluminium were studied theoretically by Faltinsen (1997), Kvålsvold and Faltinsen (1995) and Faltinsen et al. (1997), and experimentally by Aarsnes (1994) and Kvålsvold et al. (1995). In the experimental studies, the slamming impacts were performed as a drop test with horizontal, elastic plates impacting regular waves. Rotational springs were connected at the ends of the plate to simulate the stiffness of an adjacent structure. In the theoretical studies, 2D potential flow theory based on the Wagner's method was applied for the hydrodynamics, and 2D Euler beam theory was assumed for strips of the plate. The theoretical and experimental results showed good agreement, and significant hydroelastic effects were demonstrated. The relative importance of hydroelasticity for an elastic hull with wedge shaped cross section impacting a calm surface was studied in Faltinsen (1999). The studies showed a strong influence from hydroelastic effects for small impact angles and for small ratios between the impact duration and the natural period of the structure.

The theoretical methods that are applied to describe the slamming phenomenon simplify many aspects of the impact problem. A benefit of finite element models is that they can accommodate a wider range of parameters, and require fewer simplifications of the actual impact event. If FSI-solvers are available in the FEM code, then finite element solvers may solve the FSI in one single system. This procedure is beneficial as it enables fully coupling of the FSI problem. A limitation for these single system solvers is that small meshes and time steps are required, which makes the simulation more computationally demanding. Stenius et al. (2011) analysed the water entry of different elastic panels with wedge-shaped cross sections with an explicit Arbitrary Lagrange-Eulerian formulation in the nonlinear finite element code LS-Dyna. The results showed good agreement between simulations and linear theory. In Cheon et al. (2016), the explicit ALE formulation in LS-Dyna was also applied to solve the FSI problem for an elasto-plastic panel with zero deadrise angle impacting a calm surface.

Model tests are necessary for verification of the numerical models. It can be challenging to make a realistic representation of a breaking wave. Thus, the slamming impact may be simplified to a drop test. These drop tests are mostly performed either with free falling test specimens or with specimens connected to an apparatus that ensures constant velocity towards the water surface. One example of the latter is found in Stenius et al. (2013) where a servo-hydraulic slam testing system launches rigid and flexible panels with constant velocity towards the free surface.

Aarsnes (1994) performed free falling drop tests with elastic plates of steel and aluminium with zero deadrise angle. Luo et al. (2012) studied the elastic response of stiffened steel plates with wedge-shaped cross section that impacts the free surface with a 22 ° deadrise angle. Although most experiments in the literature have been conducted to find the elastic responses, or the pressure variation on rigid or elastic structures, a few exceptions are found. Seo et al. (2018) have performed free falling drop tests of unstiffened steel wedges. The permanent deformation after every test was measured in order to investigate the elastic-plastic response of the wedges.

1.3.2 Rules and Guidelines for Estimation of Loads and Response

After the COSL innovator accident in the North Sea, new offshore technical guidelines, henceforth OTG, in OTG 13 (DNVGL, 2016b) and OTG 14 (DNVGL, 2016c) for requirements and predictions of minimum air gap and horizontal wave loads, were issued by DNV-GL. The design guidelines in both of the OTG's only address ultimate limit state (ULS) design conditions, i.e. they are only valid in the elastic range. OTG 14 (DNVGL, 2016c) provides guidelines for the horizontal wave impact loads that should be used for local design of vertical structures in a 100 years storm. The pressure loads that should be applied for the evaluation of the local structural integrity are defined in terms of peak pressures, relative upwelling and the area over which the pressures should be applied.

The recommended practice, henceforth RP, in RP C205 (DNVGL, 2014) also provides methods for estimating the horizontal wave-in-deck forces. The horizontal loads consist of a drag, inertia and slamming component. Simplified formulas for estimation of slamming loads are provided in the RP.

In RP C204 (DNVGL, 2016a) and Norsok Standard (2013) N004, a simplified approach for calculation of the dynamic response to explosion loads is formulated. Because the characteristics of slamming loads and explosions are similar, the methods for response estimation from explosion loads may also be applied for the slamming impact. If the pressure-time series of the load pulse is known, the maximum deformation can be found in so-called *Biggs charts* as a function of the load duration relative to the natural period of the structural component. The goal of the accidental limit state (ALS) design method in RP C204 (DNVGL, 2016a) is to ensure that the structural component maintains its load-bearing function during an accidental event.

1.4 Limitations of the Report

At the beginning of the master thesis, it was uncertain whether the experimental drop tests would be conducted before the deadline of the thesis. As the semester progressed and the plan for the drop test became certain, the preparation and execution of the experiments became a much larger part of the master thesis than initially anticipated. Some of the parts in the original structure of the thesis was therefore removed after discussion with my supervisor Jørgen Amdahl. The modelling of the breaking wave in LS-Dyna was removed from the thesis. This is because the behaviour of a breaking wave is a very complex hydrodynamic phenomenon that is challenging to represent correctly in a finite element simulation. It was also decided not to perform simulations in LS-Dyna on a larger section of a stiffened column. The preparation of a procedure used to check ALS design of the stiffened panels have also been removed from the thesis. The stiffeners in the panel have not been varied in size or span. However, the boundary conditions, impact angle, impact velocity and material behaviour have been changed. In the experimental drop tests, focus has been placed on comparing the plastic response and deformation pattern with the numerical simulations. The pressure history and stress variations in the plate have not been studied.

1.5 Structure of the Report

The thesis is structured as follows.

- **Chapter 2:** The theoretical background for the thesis is presented.
- **Chapter 3:** The deformation resistance of a stiffened plate exposed to lateral loads is established from a simplified formulation. The results are compared with simulations in LS-Dyna.
- **Chapter 4:** Drop test impacts with a stiffened plate with 0° and 3° impact angle are performed in LS-Dyna. The stiffened steel panel has the same dimensions as the panel in chapter 3.
- **Chapter 5:** Simplified methods for calculation of the response to explosions loads in RP C204 are applied to find the maximum lateral deflection of the stiffened panel. The predicted response from the simplified approach are compared with the finite element deformations obtained in chapter 4.

- **Chapter 6:** The effect of hydroelasticity is studied for finite element drop tests of the stiffened plate in LS-Dyna with various impact angles and impact velocities. The possibility of applying the ULS pressure variation to predict the ALS response is also investigated.

- **Chapter 7:** Drop tests with unstiffened aluminium plates are performed in the Ocean Basin Laboratory with Sintef Ocean and SIMLab.

- **Chapter 8:** The experimental impacts of the unstiffened aluminium plate are recreated in finite element analyses in LS-Dyna. The deformations in LS-Dyna are compared with the measured deformations from the experiment.

- **Chapter 9:** Discussion of results.

- **Chapter 10:** Conclusion and recommendations for further work.

It should be emphasised that the stiffened steel plate in chapters 3-6 is not representative of the full scale stiffened plate of the experimental model in chapter 7-8. Hence, no comparison of the results has been performed.

Chapter 2

Theory

2.1 Slamming

A slamming impact is a highly nonlinear FSI problem characterised by high pressure peaks localised in time and space. The duration of the slamming force imposed on the body is typically in the order of milliseconds. A slamming event commonly occurs when the angle between the body surface and the fluid surface is small, leading to a rapid expansion of the contact region between the fluid and body. After the initial high-intensity pressure peak, a lower residual pressure follows. This type of pressure variation is also characteristic for explosion loads.

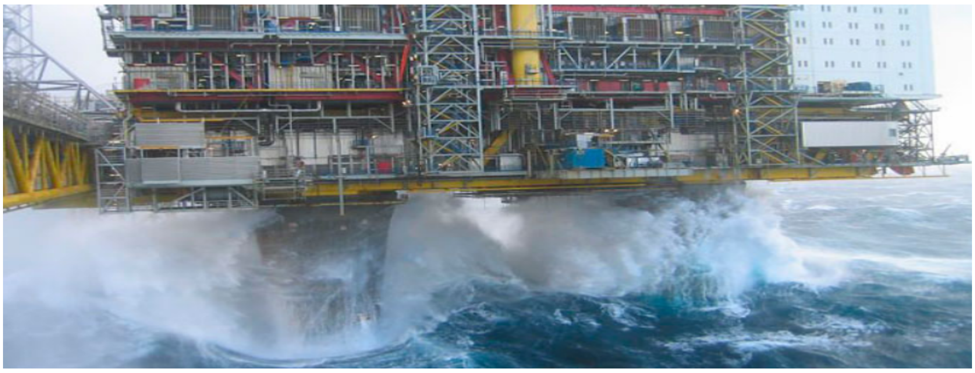

Figure 2.1: Wave slamming loads on the COSL innovator rig

Typical examples of slamming events are when the ship bottom hits the water surface at high velocity; when steep waves break near the column of a semi-submersible, or violent fluid motion inside partially filled tanks. The slamming loads can lead to severe structural damage and may be a problem for the local structural integrity as well as the global behaviour.

According to Faltinsen (2000), different physical phenomena can take place during a slamming event. For small impact angles, air cushions may form between the body and the fluid. When the structural component deforms due to the slamming load, the structural response induces changes to the surrounding fluid flow. This mutual interaction between fluid and structure is called *hydroelasticity*. From a structural point of view, the most important time scale is when the maximum strains occur. This time scale is governed by the wet eigen period of the component. Many of the physical effects have associated time scales different from the wet eigen period, and may therefore often have a negligible effect on the maximum deformations.

In Faltinsen (1990), the impact angle β and the impact velocity V have been identified as the two main parameters for characterising the features of the slamming loads. The severity of the local slamming loads increases for increasing impact velocity and decreasing impact angle. Even though the pressure peaks in such extreme conditions are high, the peaks will, according to Faltinsen (2005), not be of primary importance for the structural response. The most important parameter for the maximum strains is the pressure impulse.

Based on Wagner's slamming model description, a simplified boundary value problem for the impact between a 2D-body and water have been solved in Faltinsen (2005). In equation 2.1, the hydrodynamic pressure on an impacting structure is expressed as a function of the velocity potential. The density ρ is the density of the fluid and ϕ is the velocity potential.

$$p \cong -\rho \frac{\partial \phi}{\partial t} \tag{2.1}$$

$$\phi = -V(t)\sqrt{c(t)^2 - x^2} \tag{2.2}$$

The velocity potential is given for a 2D flat-plate body with a total wetted length 2c(t). The equivalent flat-plate body perforates the free surface with an impact velocity $V(t)$. By inserting equation 2.2 in 2.1, the hydrodynamic pressure on the plate can be expressed by equation 2.3.

$$p = \left[\rho V \frac{c}{\sqrt{c^2 - x^2}} \frac{dc}{dt}\right] + \left[\rho \frac{dV}{dt} \sqrt{c^2 - x^2}\right] \tag{2.3}$$

The first term in equation 2.3 is called the slamming pressure term, and is proportional to the rate of change of the wetted surface. The added mass pressure is commonly identified as the pressure term in phase with the acceleration of the impacting body. Thus, the second term in equation 2.3 is viewed as the added mass pressure term.

In equation 2.3 it is obvious that for a flat plate with zero impact angle, the slamming pressure will be infinite. Since this is unphysical, pressure cannot be found directly from equation 2.3 for impacts with $\beta = 0°$. For constant impact velocity, equation 2.3 can be simplified to 2.4 where the slamming pressure is proportional to the velocity squared.

$$p = \frac{1}{2}\rho C_p V^2 \tag{2.4}$$

where C_p is the pressure coefficient. The maximum slamming pressure on a wedge proposed by Zhao and Faltinsen (1993) is given by equation 2.5.

$$p_{max} = 0.5\rho\left(\frac{\pi}{4}\right)^2 \cot\beta^2 V^2 \tag{2.5}$$

2.2 Hydroelastic Structure Response

2.2.1 Criteria for Hydroelastic Response

Hydroelasticity is a physical phenomenon that may occur during a slamming impact with high pressures of very short duration. During a hydroelastic impact, the hydrodynamic pressure from the water will act on the structure, which will cause the structure to deform. Simultaneously, the vibration of the structure will influence the pressure field in the fluid flow. Hence, there will be a coupled interaction between the fluid flow and structural response. RP C205 (DNVGL, 2014) argues that it will be conservative to neglect the hydroelastic effects on the structural response if hydroelasticity is prominent during the impact. This is because the hydroelastic interaction between the structure and fluid will lead to a decreasing pressure on the structure, and hence, a smaller structural response. The appropriate solution method for the structural response depends on the presence of hydroelasticity. If hydroelasticity is negligible, the hydrodynamic loading is assumed to be the same as if the structure was completely rigid. By reapplying the hydrodynamic load history from the rigid structure to a deformable structure, the resulting deformations and stresses can be found.

Faltinsen (1999) investigated the relative importance of hydroelasticity for an elastic hull with wedge-shaped cross section impacting a calm water surface. A stiffened panel between two transverse frames was studied. The hydrodynamic problem was solved by a generalisation of Wagner's theory by including elastic vibrations. The water entry velocity of the wedge was assumed to be constant during the impact. The results showed that the importance of hydroelasticity for the local slamming induced stresses in the panels increased for increasing impact velocity and decreasing impact angle β. The non-dimensional hydroelasticity parameter ξ was introduced in equation 2.6.

$$\xi = \sqrt{\frac{EI}{\rho L^3}} \frac{tan\beta}{|V|} \tag{2.6}$$

where L is the length of the longitudinal stiffener between the transverse frames and EI is the bending stiffness per width of stiffener between the transverse frames. Faltinsen's calculations showed that hydroelastic effects were present when $\xi <\approx 1.5$, and that they had a considerable influence on the fluid-structure interaction when $\xi < 0.25$. The latter limit is applied in the recommended practices in RP C205 (DNVGL, 2014). The non-dimensional ξ-parameter is proportional to the ratio between the wetting time of the wedge and the highest natural period of the wedge. This proportionality indicates that the local hydroelastic effects become important for impacts of small duration where the structural component have a high dominant natural period.

In Bereznitski (2001), theoretical and FE-models were made for a 2D hydroelastic and rigid wedge cross section that penetrates the water surface with a constant velocity. The results also identified the ratio between the impact duration and the eigen period as the most important parameter when deciding when to include hydroelasticity. The largest structural response occurred when both hydroelasticity and entrapment of air were neglected. The lowest predicted response occurred when both hydroelasticity and air were included. The difference in the predicted responses increased for decreasing impact angle and increasing natural period of vibration. The entrapped air led to a reduction of the slamming loads, and thus a lower structural deformation. The results in Bereznitski (2001) also showed that the effect of hydroelasticity gives a large reduction of the deformation when the ratio between the duration of the impulse and the first dry natural period of the structure is small. When the ratio is larger than 2.0, hydroelastic effects are assumed negligible.

2.2.2 Analytical Hydroelastic Calculations

In Faltinsen (2005), the free vibration phase of a hydroelastic slamming impact is analysed. The structure in the analytical model is based on two-dimensional elastic Euler beam theory. Thus, 3D effects are ignored and the load levels will not cause plastic deformations. The effect of shear deformation is assumed to be negligible. The equation for the beam motion is expressed as:

$$M_B \frac{\partial^2 w}{\partial t^2} + EI \frac{\partial^4 w}{\partial x^4} = p(x, w, t) \tag{2.7}$$

The hydrodynamic pressure p is expressed in terms of the beam deflection w and the longitudinal length coordinate x. The beam with length $\pm \frac{L}{2}$ is assumed to have a constant thickness and finite width. M_B is the structural mass per length square, and EI is the bending stiffness per length width. Because only the free vibration phase of impact is considered, the slamming pressure is zero. The hydrodynamic pressure p acting on the plate arises from the oscillations of the beam.

In the experiments for hydroelastic plate impact in Aarsnes (1994) and Kvålsvold et al. (1995), it was found that the lowest mode shape corresponding to the highest natural period dominated the response shape. The first elastic mode shape Ψ_1 of the response is assumed to follow a simple cosine pattern.

$$\Psi_1 = cos(p_1 x) \tag{2.8}$$

where $p_1 = \pi / L$. The beam deflection is expressed by the time scaled shape function.

$$w(x, t) = a_1(t)\Psi_1(x) \tag{2.9}$$

Here, $a_1(t)$ is the unit amplitude oscillation. The pressure $p(x, t)$ due to the vibrations of the flexible plate may be approximated using the solution for the forced heave problem of the beam. By averaging the mode shape function in equation 2.8 over the beam length, a relationship between the amplitude of the mode shape and the amplitude of the rigid plate is found in equation 2.10.

$$\frac{\partial \varphi}{\partial z} = \frac{1}{L}\int_{-\frac{L}{2}}^{\frac{L}{2}} cos(p_1 x)dx = \frac{2}{\pi} \tag{2.10}$$

The pressure due to the flexible motion of the beam is then expressed as:

$$p(x,t) = \rho \ddot{a}_1(t)\frac{2}{\pi}\sqrt{\left(\text{‘}\frac{L}{2}\right)^2 - x^2} \tag{2.11}$$

Damping of the beam during the free vibration phase is not considered in the analysis. Thus, the relevant terms in the dynamic equation of motion for the first flexible mode are the generalised structural mass M_{11}, added mass A_{11} and the stiffness C_{11}.

$$(M_{11} + A_{11})\frac{\partial^2 a_1}{\partial t^2} + C_{11}a_1 = 0 \tag{2.12}$$

The generalised added mass A_{11} [kg/m] due to a unit amplitude oscillation in the first flexible mode is given by equation 2.13

$$A_{11} = \rho\frac{2}{\pi}\int_{-\frac{L}{2}}^{\frac{L}{2}} \sqrt{\left(\frac{L}{2}\right)^2 - x^2 cos(p_1 x)dx} \tag{2.13}$$

2.3 Scaling of Model Tests

2.3.1 Scaling Factors

The goal of an experimental model is to represent the behaviour of a full-scale system as realistic as possible at a much smaller scale. In order to obtain similar behaviour in both scales, it is necessary to determine the optimum scaling laws and which properties the scaling should apply to. The selection of the model scale is limited by several factors, such as size of testing facility, scaling effects, costs and instrumentation requirements. According to Steen (2014), large scales may be costly, difficult to handle and more challenging to install in the experimental facility. For small scales, problems with accuracy and scale effects may be challenging. In RP C205 (DNVGL, 2014), scaling effects can be understood as additional corrections that have to be applied to the scaling laws.

According to RP C205 (DNVGL, 2014), the most common method is Froude scaling, which ensures that gravity forces are properly scaled. Slamming pressures are scaled according to Froude, but according to the RP, Froude scaling is not applicable to entrapped air. If entrapped air is present during the slamming event, scaling effects may give inaccurate predictions. By assuming that the problem is geometrically similar in model and full scale, the structural dimensions in the in model scale should be scaled by a factor λ. Some Froude scale parameters are given in table 2.1.

Table 2.1: Scaled parameters according to Froude's scaling law

Parameter	Scaling Factor	Unit
Length	λ	mm
Velocity	$\lambda^{1/2}$	m/s
Linear Acceleration	λ^0	m/s^2
Angle	λ^0	degrees

2.3.2 Non-Dimensional Scaling

When experimental results are scaled to other dimensions or materials, non-dimensional variables are often applied. Introducing non-dimensional variables can be a useful tool as long as the variables are able to capture the real physics of the problem. In Faltinsen (2005), non-dimensional variables have been introduced in order to define scaling relations for the elastic response due to slamming. Two important nondimensional parameters related the slamming impact are the hydroelastic parameter ξ in equation 2.6, and the nondimensional maximum strain in equation 2.14.

$$\frac{\varepsilon_m EI tan\beta}{z_a V^2 \rho L^2} \tag{2.14}$$

where EI is the bending stiffness per length width, L is the length of the beam, ε_m is the maximum strain, z_a is the distance to the neutral axis, ρ is the mass density of water, β is the deadrise angle, and V is the impact velocity. By imposing geometric similarity between the model and full-scale, scaling criteria for bending stiffness and yield stress may be derived from the non-dimensional parameters. Full scale variables are denoted with a bar.

$$\frac{tan\beta}{V\sqrt{\rho L^3/EI}} = \frac{tan\bar{\beta}}{\bar{V}\sqrt{\bar{\rho}\bar{L}^3/\bar{E}\bar{I}}} \tag{2.15}$$

$$\frac{\bar{E}\bar{I}}{EI} = \left(\frac{tan^2(\beta)}{tan^2(\bar{\beta})}\right)\left(\frac{\bar{V}^2}{V^2}\right)\left(\frac{\bar{\rho}}{\rho}\right)\left(\frac{\bar{L}^3}{L^3}\right) \tag{2.16}$$

By introducing the scaling factor λ to equation 2.16 according to the Froude scaling laws in table 2.1, the scaling criteria for bending stiffness may be expressed as in equation 2.17.

$$\bar{E}\bar{I} = EI\lambda^4 r \tag{2.17}$$

where r is the relationship between the water density in full-scale relative to the model scale. By assuming that the nondimensional maximum strain is equal in model and full scale and that $\sigma_y = E\varepsilon_m$, the criterion for scaling of yield stress can be expressed by equation 2.18.

$$\frac{\bar{\sigma}_y}{\sigma_y} = \left(\frac{\bar{z}_a}{z_a}\right)\left(\frac{\bar{V}^2}{V^2}\right)\left(\frac{\bar{\rho}}{\rho}\right)\left(\frac{\bar{L}^2}{L^2}\right)\left(\frac{tan^2(\beta)}{tan^2(\bar{\beta})}\right)\left(\frac{I}{\bar{I}}\right) \tag{2.18}$$

which can be rewritten to equation 2.19.

$$\bar{\sigma}_y = \lambda\sigma_y \tag{2.19}$$

2.4 Structural Response Analysis

2.4.1 Categorisation of Loading Domains

According to RP C204 (DNVGL, 2016a), the structural dynamic response may be divided into three loading regimes depending on the duration of the load pulse, t_d, relative to the fundamental period of vibration of the component T_n. These regimes are the quasi-static, dynamic and impulsive domain, and are divided by the following limits:

Impulsive

$$\frac{t_d}{T_n} < 0.3 \tag{2.20}$$

Dynamic

$$0.3 < \frac{t_d}{T_n} < 3 \tag{2.21}$$

Quasi-static

$$3 < \frac{t_d}{T_n} \tag{2.22}$$

In the impulsive domain, the duration of the pressure pulse is very short compared to the natural period. In Larsen (2014), the structural response has been divided into two phases. During the first phase, the pressure pulse acts directly on the system and forces it to vibrate, while in the second phase, the loading is removed and the system vibrates freely. In the impulsive domain, the maximum strains occur during the second phase. According to Faltinsen (2005), the structural response will be governed by the magnitude of the impulse. The expression for the impulse is given in equation 2.23.

$$I = \int_0^{t_d} P(t)dt \tag{2.23}$$

Due to the simple dependency between the magnitude of the impulse and response, a rough estimate of the maximum deformation for short impulses can according to Larsen (2014) be estimated from equation 2.24.

$$w_{max} = \frac{I}{\sqrt{km}} \tag{2.24}$$

In the quasi-static domain, the duration of the pressure impulse is longer than the response time of the structure. The quasi-static response is close to static, which means that inertia effects may be neglected. According to RP C204 (DNVGL, 2016a), the response depends upon the peak pressure and the rise time of the pressure impulse, but not the pressure-time history.

In the dynamic domain, the relationship between the load and response is more complex. Contrary to the impulsive and quasi-static domain, the structural response is significantly influenced by the pressure-time history of the impulse (Langseth et al., 2016), which implies that the dynamic response must be solved by numerical integration of the dynamic equilibrium equations.

2.4.2 Yield Line Mechanism

For a plastic limit analysis of a structural member subjected to bending, the transition from elastic to plastic behaviour occurs when the bending moments in the component have reached the plastic bending moment resistance, M_p. When M_p is reached, a plastic hinge will be formed at this location. Figure 2.2 shows the formation of a plastic hinge for a simply supported beam. The beam behaves like two rigid beams connected with a plastic hinge in the middle, which allows them to rotate relative to each other.

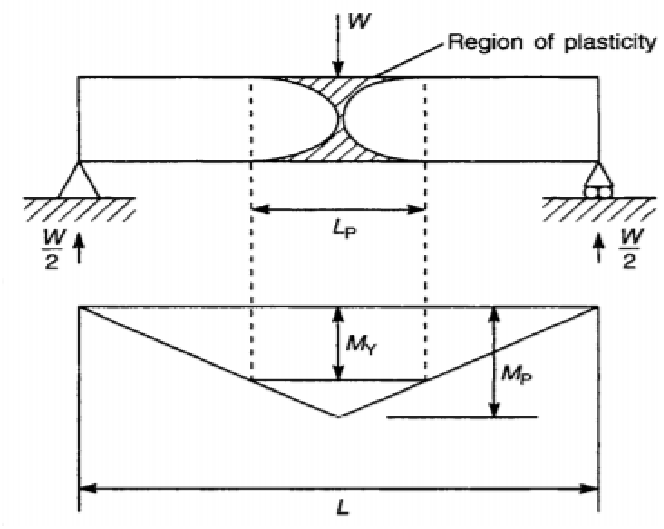

Figure 2.2: The formation of a plastic hinge for a simply supported beam from Megson (2005)

Several plastic hinges may be formed if the load pattern, boundary conditions or structural shape are more complicated. When a sufficient number of plastic hinges have been formed in the structure, the structure will collapse. The unrestricted plastic flow in a plate leads to the formation of yield lines. The local collapse mechanism of the plate will follow the formation of these yield lines.

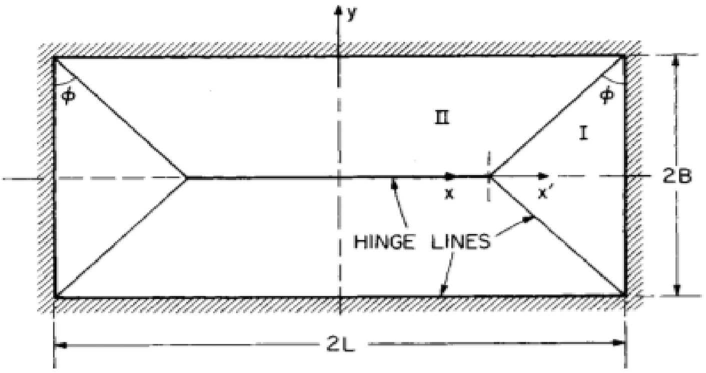

Figure 2.3: Plastic hinge line pattern in a fully clamped rectangular plate subjected to a uniformly distributed lateral pressure from Norman (1971)

2.4.3 Resistance Model for Stiffened Plate Subjected to Lateral Loads

The resistance curves for stiffened plates exposed to lateral loads provide the relationship between plastic resistance and lateral deformation. These response curves may be established analytically from methods in Norsok Standard (2013) N004 and RP C204 (DNVGL, 2016a) for plates and beams with different dimensions, flexibility and boundary conditions.

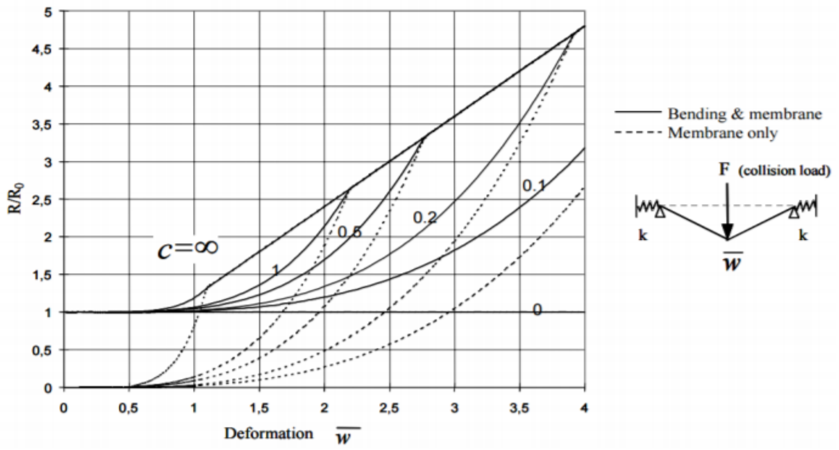

Figure 2.4: Plastic resistance curve from Norsok Standard (2013) for different non-dimensional spring stiffness c

Amdahl et al. (2017) present a simplified method for the assessment of the resistance curves of stiffened panels subjected to lateral loading. The objective of the proposed formulation is to provide a quick method for realistic estimates of the deformation resistance of panels subjected to abnormal or accidental lateral loads such as dropped objects, slamming impacts or collisions.

It is assumed that the stiffened plate behaves like beams with an effective flange. The formulation provides an expression for the lateral deformation resistance R as a function of the development of bending moments and membrane forces across the beam cross section for increasing lateral displacement. The material formulation assumes a rigid perfectly-plastic material, and the effect of shear deformation is assumed to be negligible.

Figure 2.5, shows the beam collapse mechanism for a general loading condition. The beam is subjected to a uniform patch load on the distance B. If B=0, then α=0.5 and $L_{eff} = L$, which means that the load is approximated as a point load in the middle. If the pressure p is uniformly distributed over the entire beam length, the resistance may be estimated with an effective concentrated force P = 0.5pL

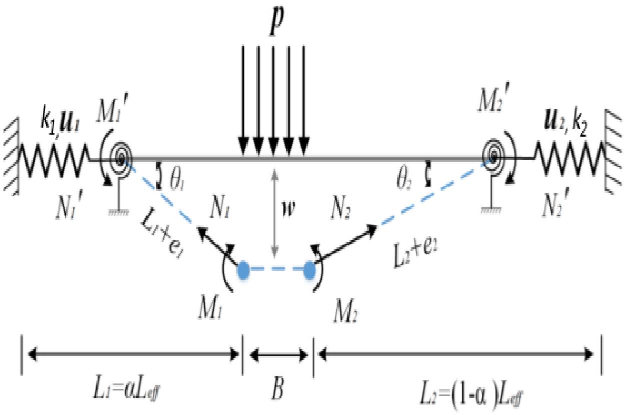

Figure 2.5: Beam collapse mechanism in the simplified model for a general loading condition

The translational flexibility of the beam is accounted for in the translational axial stiffness towards inwards motion, k. According to RP C204 (DNVGL, 2016a), the axial stiffness may be introduced as:

$$\frac{1}{k} = \frac{1}{k_{node}} + \frac{L}{2EA_e} \tag{2.25}$$

The first term in equation 2.25 represents the influence of the adjacent structure to the axial stiffness in the member. The second term in 2.25 is the axial stiffness of the beam section, where A_e is the effective cross-section area of the stiffener and effective plate flange.

In the simplified method by Amdahl et al. (2017), a non-dimensional translational stiffness factor c for a general loading case is introduced as:

$$c = \frac{2kh_w^2}{\alpha(1-\alpha)L_{eff}N_p} \tag{2.26}$$

The non-dimensional stiffness factor normally ranges between values from 0 to 1. If c = 0, the beam ends have no axial fixity, and if c = 1, the beam has close to fixed boundaries. When c=inf, the solution converges to the solution for completely fixed ends. When the lateral deformation becomes sufficiently large, the resistance will converge towards the solution for a beam in pure tension with fixed ends for all values of c.

The stress distribution over the cross section during the first part of the deformation is governed by pure bending. With increasing lateral deformation, the load carrying mechanism will change from bending to membrane. As the load carrying mechanism changes from bending to membrane, the membrane force N will "occupy" an increasing part of the cross section. According to Langseth et al. (2016), the bending resistance is negligible when the membrane force N equals the membrane capacity N_p. The nondimensional interaction functions for membrane forces N/N_p and bending moments M/M_p are calculated for increasing lateral deflection w and tension force N in the stiffener cross section. Based on the non-dimensional interaction functions, the non-dimensional resistance can be expressed as in equation 2.27 for a general loading case.

$$\frac{R}{R_o} = \frac{M}{M_p} + \frac{Nw}{\beta M_p}; \qquad \beta = \begin{cases} 1 & free \ \ rotation \\ 2 & fixed \, rotation \end{cases} \tag{2.27}$$

where M_p is the plastic bending moment resistance, N_p is the plastic axial resistance, R_o is the plastic collapse resistance in pure bending, and R is the lateral deformation resistance.

The plastic collapse resistance in pure bending R_o is given in equation 2.28.

$$R_0 = \beta M_p \left(\frac{1}{\alpha L_{eff}} + \frac{1}{(1-\alpha) L_{eff}} \right) \tag{2.28}$$

The stiffness in the elastic domain k_1 can be found from equation 2.29. The maximum elastic displacement is denoted w_{el}.

$$k_1 = \frac{R_0}{w_{el}} \tag{2.29}$$

2.4.4 Single Degree of Freedom Analogy

A simplified calculation model for response prediction of stiffened panels subjected to explosion loads has been described in RP C204 (DNVGL, 2016a). Slamming loads and explosions share a lot of the same characteristics, e.g. high peak pressures of short duration. Therefore, it can be argued that the simple response formulation is also applicable to slamming loads. In the RP, the dynamic impact problem is simplified to a single mass-spring system subjected to an equivalent triangular load pulse of duration t_d. According to the RP, it is convenient to assume that the dynamic deformation pattern will be approximately the same shape as the static deformation pattern. The precision of the assumed displacement pattern depends on how accurate this approximation is. The deformation is split into a spacial shape function $\varphi(x)$ and a temporal coordinate y(t), where $\varphi(x)$ is the shape function for the assumed displacement pattern, and y(t) is equal to the displacement magnitude.

$$w(x,t) = \varphi(x)y(t) \tag{2.30}$$

By applying the assumed deformation shape, the dynamic equilibrium equations may instead be solved in the generalised form shown in equation 2.31. The parameters $\bar{m}$, $\bar{k}$ and $\bar{f}$ are the generalised mass, stiffness and load, respectively.

$$\bar{m}\ddot{y} + \bar{k}y = \bar{f}(t) \tag{2.31}$$

When $\bar{m}$, $\bar{k}$ and $\bar{f}$ are known, equation 2.31 may be solved by numerical integration or by an analytical method. If the pressure history from the explosion impulse can be approximated as a triangular load pulse with amplitude F_{max} and duration t_d, then the maximum dynamic response can be calculated from *Biggs design charts* for the SDOF system. Each curve in the chart is plotted for a given relation between the plastic collapse resistance in pure bending R_{el} (also denoted R_o) and the triangular load amplitude F_{max}. For a given R_{el}/F_{max}, the duration of the impulse t_d relative to the eigen period of the system T_n is applied to find the corresponding relation between the max displacement w_{max} and the maximum elastic displacement w_{el}. If the response is in the impulsive domain, then the maximum response is independent of the shape of the triangular load curve.

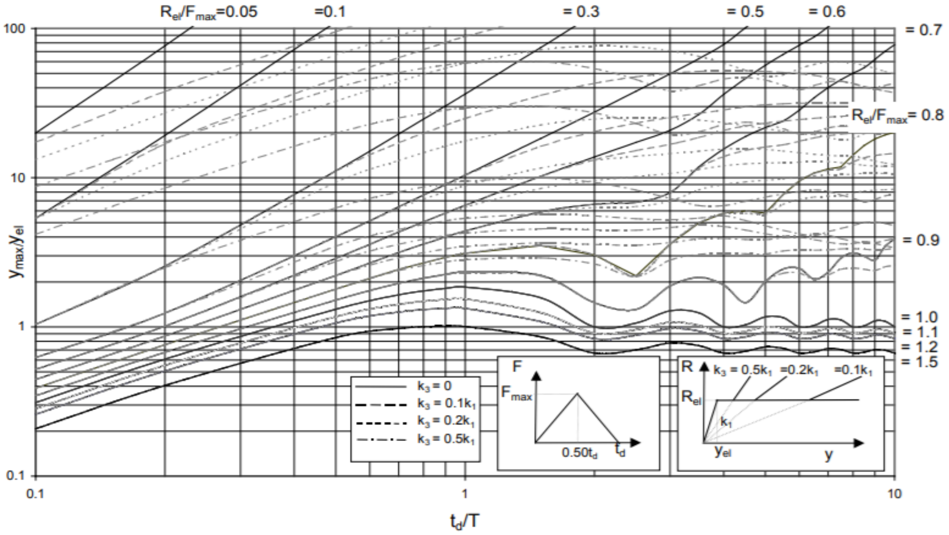

Figure 2.6: Biggs chart for a SDOF system subjected to a triangular load pulse with rise time $0.5t_d$ from DNVGL (2016a)

The solid lines in the Biggs chart in figure 2.6 represent the response for a linear perfectly-plastic system where membrane effects are not considered. The dashed and dotted lines take different membrane effects into account with different degrees of stiffness in the membrane stage. In order to apply the simplified approach with SDOF analogy and Biggs charts, both the load history and the resistance curve from the actual nonlinear impact must be approximated. The resistance curve for the real non-linear system is often simplified into three linear stages with stiffness k_1, k_2 and k_3. The tri-linearisation of the resistance curve is shown in figure 2.7.

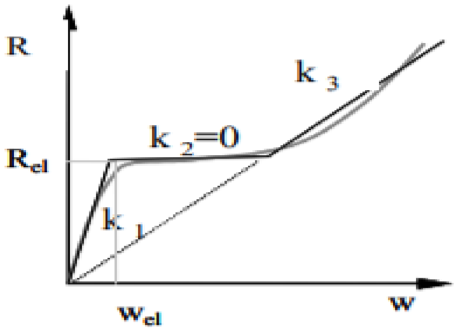

Figure 2.7: Non-linear resistance curve approximated by an equivalent tri-linear system DNVGL (2016a)

R_{el} is the plastic collapse force in pure bending and w_{el} is the deflection at the end of the initial, linear resistance domain. The elastic stiffness coefficient in the initial, linear resistance domain k_1 is calculated from equation 2.29. The stiffness k_2 is zero. If $k_3 \neq 0$, then the response of the system is elasto-plastic with membrane effects and strain hardening. Membrane effects are typically prominent when the boundaries of a stiffened plate are restricted against axial in-plane displacement. For increasing lateral deflection, membrane forces will develop, which will lead to an increase in the load carrying capacity of the structural component.

2.4.5 Added Mass for Rectangular Plates

When a structure oscillates in a fluid, the motion of the body will induce changes in the surrounding pressure field. The change in pressure on the structure contributes as an additional force acting in phase with the acceleration of the submerged body. This additional force is identified as the added mass term. In dynamic analyses, inertia effects are not negligible, and the effect of added mass must therefore be included.

There are several methods for estimation of the added mass for rectangular plates. The analytical approach for finding the added mass for flexible beams described in section 2.2.2 may be extended from 2D beam theory to 3D plates. If the edges in the length direction of the plate can move freely, the mode shape of the plate will follow a cosine pattern in the length direction. The added mass per unit width for the plate would thus be identical to the added mass of the beam section in equation 2.13. To find the total added mass, the expression for A_{11} must be multiplied by the width of the plate.

If the edges of the plate in length direction are not free to move, the mode shape is more likely to follow a cosine pattern in both transversal and longitudinal direction. The first mode shape should then be rewritten to:

$$\Psi_1 = cos(p_1 x) cos(p_1 y) \tag{2.32}$$

A factor accounting for 3D-effects and the mode shape of a flexible plate compared to that of a rigid plate is given in equation 2.33.

$$\frac{\partial \varphi}{\partial z} = \frac{1}{L^2} \int_{-\frac{L}{2}}^{\frac{L}{2}} cos(p_1 x) \int_{-\frac{L}{2}}^{\frac{L}{2}} cos(p_1 y) dy dx = \frac{4}{\pi^2} \tag{2.33}$$

The added mass A_{11} [kg] for the first flexible mode shape of the stiffened plate is given by:

$$A_{11} = \rho \frac{4}{\pi^2} \int_{-\frac{L}{2}}^{\frac{L}{2}} \int_{-\frac{L}{2}}^{\frac{L}{2}} \sqrt{\left(\frac{L}{2}\right)^2 - x^2 cos(p_1 x) cos(p_1 y) dy dx} \tag{2.34}$$

The added mass may also be established from RP C205 (DNVGL, 2014), where added mass coefficients are given for different 2D and 3D geometries. Figure 2.8 shows the added mass parameters for a 3D rectangular plate in infinite fluid subjected to a forced heave motion. From the tabulated parameters, the added mass M_a [kg] can be calculated from equation 2.35.

$$M_a = \rho C_a V_r \tag{2.35}$$

C_a is the added mass coefficient, V_r is the reference volume, and ρ is the fluid density. The tabulated values from the RP assumes a rigid plate with uniform oscillations in finite water. If the plate is deformable, the added mass from equation 2.35 must be adjusted to account for the effect of non-uniform vibrations. This factor corresponds to the factor of $2/\pi$ in equation 2.10.

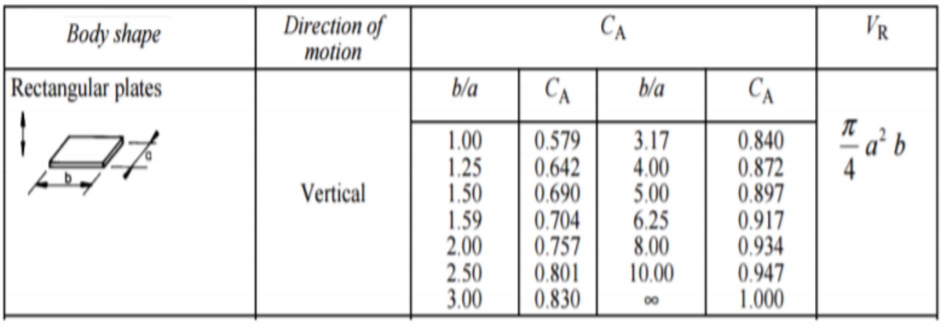

Body shape	*Direction of motion*	C_A				V_R
Rectangular plates		*b/a*	C_A	*b/a*	C_A	
	Vertical	1.00 1.25 1.50 1.59 2.00 2.50 3.00	0.579 0.642 0.690 0.704 0.757 0.801 0.830	3.17 4.00 5.00 6.25 8.00 10.00 ∞	0.840 0.872 0.897 0.917 0.934 0.947 1.000	$\frac{\pi}{4} a^2 b$

Figure 2.8: Added mass parameters for 3D rectangular plates in infinite fluid

2.5 Material Behaviour

2.5.1 Calibration of Stress-Strain Curves from Tensile Tests

The output from a quasi-static tensile test is commonly the force F, the position of the grip and time. Based on measurements of force, elongation and the initial geometry of the test specimen, the engineering stress and strain can be computed.

$$\sigma_e = \frac{F}{A_0} \tag{2.36}$$

$$\varepsilon_e = \frac{\Delta L}{L_0} \tag{2.37}$$

The true stress and logarithmic true strain in equations 2.38 and 2.39 are derived from the engineering stress and strain.

$$\sigma_t = \sigma_e(1+\varepsilon_e) \tag{2.38}$$

$$\varepsilon_t = ln(1+\varepsilon_e) \tag{2.39}$$

The effective plastic strain is derived in equation 2.40.

$$\varepsilon_{pt} = \varepsilon_t - \sigma_t / E \tag{2.40}$$

2.5.2 Nonlinear Material Parameters from RP C208

Nonlinear material parameters for the elasto-plastic response of different steel types have been defined in RP C208 (DNVGL, 2013). The true stress-true strain curves are defined by a combination of step-wise linear and power law definition after a yield plateau, as shown in figure 2.9. The power law equation for the elasto-plastic materials is defined in equation 2.41.

$$\sigma = K\left(\varepsilon_p + \left(\frac{\sigma_{yield2}}{K}\right)^{\frac{1}{n}} - \varepsilon_{p\_y2}\right)^n \qquad \varepsilon_p > \epsilon_{p\_y2} \tag{2.41}$$

where K and n are power law parameters, σ and ε are the true stress and strain, and σ_{yield2} and ε_{p_y2} are the true stress and strain at the end of the yield plateau.

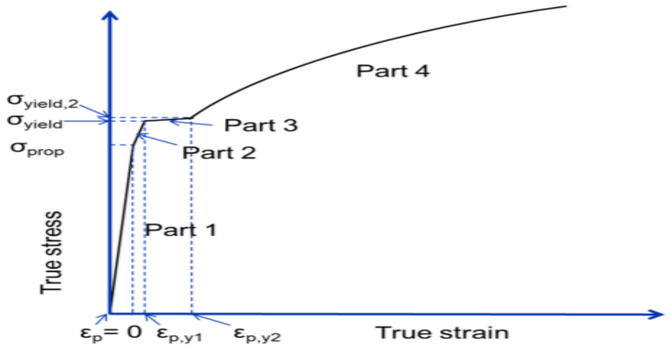

Figure 2.9: Definition of true stress-true strain curve according to RP C208 (DNVGL, 2013)

2.5.3 Strain Rate Hardening

A rapid impact may introduce strain-rate sensitivity to the material. When a material is rate dependent, strain rates during plastic deformation will increase the plastic flow stress of the material and thus increase the resistance to further deformation. If the effect of strain rate hardening is not taken into account for a rate dependent material, the response prediction will be overestimated. The method developed by Cowper and Symonds (1957) accounts for the effect of strain rate dependence in the plastic flow by scaling the static stress by a dynamic hardening factor in order to find the dynamic strain.

$$\sigma_{dynamic} = \sigma_{static}\left[1 + \left(\frac{\dot{\varepsilon}}{C}\right)^{\frac{1}{p}}\right] \tag{2.42}$$

C and p are the strain rate hardening parameters and $\dot{\varepsilon}$ is the strain rate. According to RP C208 (DNVGL, 2013), C = 4000 s^{-1} and p=5 are recommended for steel materials in offshore steel structures.

2.5.4 Johnson-Cook Constitutive Relation

The elasto-plastic behaviour of metals is characterised by an yield condition and a hardening rule. The yield condition describes the stress state when the plastic deformation occurs, while the hardening rule describes how the yield conditions and flow stress modify due to strain hardening during the plastic deformation. If the plastic material behaviour also is dependent on strain rates and temperature, this must be included in the equation for the flow stress.

The Johnson-Cook constitutive relation in equation 2.43 describes the plastic behaviour of metals as a function of strain, strain-rate and temperature. The first term describes the effect of plastic hardening, the second term accounts for strain rate hardening effects, and the third term includes thermal softening.

$$\sigma_{flow} = \left(A + B\varepsilon_{pt}^{n}\right)\left(1 + Cln\left(\frac{\dot{\varepsilon}_{pt}}{\varepsilon_0}\right)\right)\left(1 - T^{*m}\right) \tag{2.43}$$

where σ_{flow}, ε_{pt}, $\dot{\varepsilon}_{pt}$ and ε_0 are the flow stress, the effective plastic strain, the effective plastic strain-rate and a reference strain rate, respectively. The temperature term T^* is given as $T^* = (T - T_{room})/(T_{melt} - T_{room})$. The five material parameters A, B, C, n and m may be calibrated by a least square fit of equation 2.43 to a true stress-effective plastic strain curve from a tensile test. According to Hopperstand and Børvik (2017), the strain rate sensitivity constant C will normally be small for most metals. At room temperature, C will typically range between 0.001 and 0.01.

2.6 Limit State Conditions

Limit state designs refer to different limit states beyond which the structure no longer fulfils the relevant design criteria. *Ultimate limit state design*, ULS, refers to a design check for environmental loads with an annual probability of exceedance of 10^{-2}, i.e. a 100 year return period. The ULS design approach considers the upper elastic limit of the structure. This means that the structural response considered in the ULS load category will be predominantly in the elastic domain. For *accidental limit state design*, ALS, survival conditions for a structure subjected to abnormal environmental conditions or accidental loads are considered. The ALS design approach ensures that the structural response due to the accidental actions does not result in complete loss of performance or structural integrity. ALS design refers to a capacity check of the structure to be able to withstand accidental or abnormal loads with an annual probability of exceedance of 10^{-4}. Contrary to the ULS design condition, the response considered in ALS design will be predominantly elasto-plastic.

2.7 Background Theory for LS-Dyna

LS-Dyna is a nonlinear finite element solver developed by LSTC. The program is suitable for non-linear, transient problems such as automotive crash and explosions. LS-Dyna is also capable of simulating complex fluid-structure interaction problems.

2.7.1 Arbitrary Lagrangian–Eulerian Formulation

Numerical simulations of highly non-linear problems must often be able to deal with strong distortions of the finite elements, and at the same time maintain an accurate resolution of the material boundaries. The kinematic description of the continuum determines the relationship between the deforming continuum and the computational mesh. The choice of these conditions governs the ability of the numerical model to handle severe distortions and provide a clear delineation between different material surfaces.

Two of the main descriptions of motion are the *Lagrangian* and *Eulerian* formulations. In the Lagrangian description, the computational grid follows the material. Because the mesh deforms with the material, large element distortions easily occur. One of the major benefits of the Lagrangian description is that it allows easy tracking of free surfaces between materials. This is a great benefit in solid mechanics. In the Eulerian formulation, the material is not connected to the mesh, but allowed to move between the computational grid. Since the material is allowed to flow through the mesh, element distortions are handled more easily, but often at the expense of interface precision.

One of the most common descriptions of fluid-structure interactions in continuum mechanics is by the *Arbitrary Lagrangian-Eulerian* formulation, denoted ALE. The goal of the ALE method is to overcome the shortcomings of purely Lagrangian and Eulerian methods by combining their best features. When the ALE formulation is applied, the computational mesh is allowed to move arbitrarily to avoid element distortion, while the mesh at the material interfaces can move along with the material to ensure precise tracking of the boundaries.

2.7.2 ALE in LS-Dyna

In LS-Dyna, both Lagrangian, Eulerian and ALE formulations may be combined in the same numerical model. This is especially an advantage for fluid-structure interaction problems, since the Lagrangian formulation is suitable for solid problems, while Eulerian and ALE formulations are suitable for modelling fluids. When water and air are modelled by the ALE approach in LS-Dyna, there are two main approaches. The simplest approach is to use ALE with a single material and void, where the air is modelled as a void space. When air is modelled as a void, it must be given the same constitutive properties as water. It is assumed that the error of approximating air as a void will be small due to the relatively low density of air. The second approach is to model water and air with an ALE multi-material formulation, where the air is treated as a separate ALE material. For both approaches, the mesh for air and water must have merged nodes at their shared boundaries.

2.7.3 Penalty Algorithm

When Lagrangian structures interact with ALE fluids, the fluid-structure interaction must be handled by a coupling algorithm that computes the coupling forces at the fluid-structure interface. The different meshes usually interact via a penalty-based coupling. In a FSI problem, the impacting surfaces must either be assigned the role of masters or slaves. According to Aquelet et al. (2006), the role of slaves is commonly given to the part in motion, while the role of master is assigned to the stationary part. The surface of the Lagrangian elements has a predefined number of coupling points in which the penetration between the Lagrange and ALE part are measured. When penetration of the coupling points is detected, the penalty algorithm generates a resisting force to the slave node, proportional to its penetration through the master surface. This penalty force will be applied to both the slave and master nodes in the opposite direction in order to satisfy equilibrium. The contact force in the penalty algorithm is represented by linear springs with a spring coefficient k between the master and slave nodes.

$$\begin{aligned} F_s &= -k \cdot d \\ F_m^i &= N_i \cdot k \cdot d \end{aligned} \tag{2.44}$$

where d is the penetration vector and N_i is the shape functions at node i.

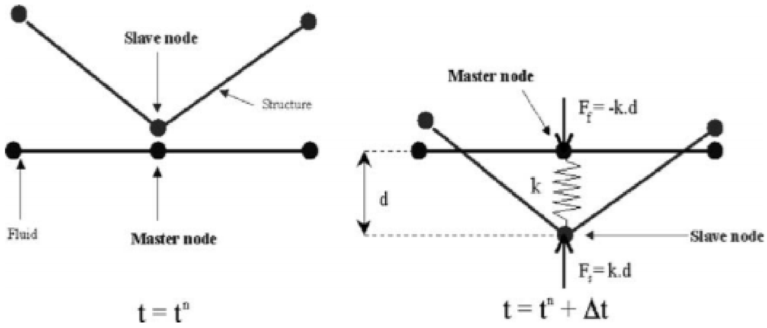

Figure 2.10: Illustration of the penalty coupling algorithm from Aquelet et al. (2006)

2.7.4 Equation of State

An equation of state, denoted EOS, describes how changes in fluid pressure relate to the volumetric changes of the fluid. The equation of states are mostly used in conjunction with simulations where the materials behave similarly to fluids. The EOS formulations are only applicable to solid elements and a few types of shell elements with large thickness. The choice of EOS depends on the characteristics of the material and the simulation. When large deformations are present, the *Gruneisen* EOS is mostly applied. If the deformations are smaller, the EOS may instead be defined in terms of a linear polynomial model.

The pressure for compressed materials defined according to the Gruineisen EOS is expressed in equation 2.45:

$$p = \frac{p_o C^2 \mu [1 + (1 - \frac{\gamma_0}{2})\mu - \frac{a}{2}\mu^2]}{[1 - (S_1 - 1)\mu - S_2(\frac{\mu^2}{\mu+1}) - S_3(\frac{\mu^3}{(\mu+1)^2}]^2} + (\gamma_0 + a\mu)E \tag{2.45}$$

In the formulation of the Gruneisen EOS in LS-Dyna, the shock velocity is defined as a function of the particle velocity $v_s(v_p)$. S_1, S_2 and S_3 are unitless coefficients of the slope of the $v_s(v_p)$ curve. According to LSTC (2001), C is taken as the bulk sound speed, γ_0 [-] is the initial value of the Gruneisen gamma, a [-] is a volume correction for γ_0 and E is the internal energy. The excess compression μ is defined in terms of the current density ρ and the initial density ρ_0 by

$$\mu = \frac{\rho}{\rho_0} - 1 \tag{2.46}$$

The parameters for different materials in EOS varies in literature. It is therefore important to find the best suitable parameters both for the material and the specific characteristics of the simulations. The EOS Gruneisen parameters for water and air are given in table 2.2.

Table 2.2: EOS Gruneisen for aluminium, steel, water and air

	C	S1	S2	S3	γ_0	A	E_0	V_0	Source
Water	1480	2.56	-1.986	0.227	0.5	0	0	0	(Brett, 1998)
Air	343.7	0	0	0	1.4	0	0	0	(LSTC, 2001)

2.7.5 Explicit Time Integration Scheme

Explicit finite element methods are suitable non-linear impact problems. An explicit integration scheme finds the configuration at time t_{n+1} as a function of previous configuration. This integration method is only conditionally stable, which means that a sufficiently small time step must be chosen to ensure a stable solution. According to Hopperstand and Børvik (2017), the critical time step for the explicit formulation is given in equation 2.47.

$$\Delta t_{critical} = \alpha \left(\frac{l_e}{c_e} \right) \tag{2.47}$$

where l_e is the characteristic size if an element e, c_e is the current wave speed in the material and α is a safety factor for the critical time step. The limit for the time step in equation 2.47 means that no information should be able to propagate across more than one element per time step. The wave speed $c_e = \sqrt{\frac{E}{\rho}}$, where E and ρ is the Young's modulus and density of the material. Since small mesh sizes are necessary for highly nonlinear impact problems, the critical step size can become very small. According to Dynamore (2018), the minimum step size is automatically applied by LS-Dyna in the explicit integration. A safety factor of α=0.67 is recommended for high explosives.

2.7.6 Added Mass in LS-Dyna

When simulating a fluid-structure interaction problem in LS-Dyna, the added madd is automatically included and does not have to be specified as input by the user. The added mass can be seen in the results as pressure components proportional to the acceleration.

Chapter 3

Simplified Method for Deformation Resistance to Lateral Loads

In this chapter, the simplified approach by Amdahl et al. (2017) has been applied to estimate the resistance curves for a stiffened plate subjected to uniformly distributed lateral loads. The results have been compared with the corresponding static resistance-deformation curves in LS-Dyna.

3.1 Finite Element Model of Stiffened Panel

The stiffened panel consists of a quadratic plate with five equally spaced bulb flat stiffeners. The 3x3 m^2 plate area has been chosen in correspondence with the technical guidelines in OTG 14 (DNVGL, 2016c), where the response of a 3x3 m^2 stiffened plate is evaluated for horizontal wave loads. The dimensions of the stiffened plate are identical to those described in Skjeggedal (2017). The plate thickness and stiffener profile have been chosen in accordance with recommendations from the offshore standard for the design of steel structures in RP C101 (DNVGL, 2015). A plate thickness of 8 mm fulfils the minimum thickness requirement for plates subjected to lateral loads. Based on the RP C101 safety requirement that the section modulus of the stiffener profile should not be taken as less than 15 cm^3, the HP180x10 stiffener profile was chosen as a suitable bulb flat stiffener. In order to simplify the finite element model, the bulbs have been replaced by rectangular flanges that provide the same moment of inertia to the stiffeners as the originally selected bulb flats. The final dimensions of the stiffened panel are summarised in table 3.1.

Table 3.1: Structural dimensions of the stiffened panel

Plate thickness [mm]	Plate area [m^2]	Stiffener spacing [mm]	H_{web} [mm]	t_{web} [mm]	W_{flange} [mm]	t_{flange} [mm]
8	3x3	500	165	10	27.4	30

The stiffened panel is modelled as four-noded shell elements with S/R Hughes Liu shell formulation with five integration points through the thickness. The plate is discretised in quadratic elements, while the stiffener and flange are discretised in rectangular elements with length equal to the quadratic plate elements. To find the optimum mesh, an increasing lateral pressure load was slowly applied to the plate for various finite element discretisations. Figure A.1 in appendix A shows the lateral deflection of the middle node at the stiffener bottom for increasing lateral pressure. The variation in midpoint deflection is small for the static pressure deformation curves. Due to the small overall difference between the static deformation curves, the model is discretised with the coarsest mesh shown in figure 3.1.

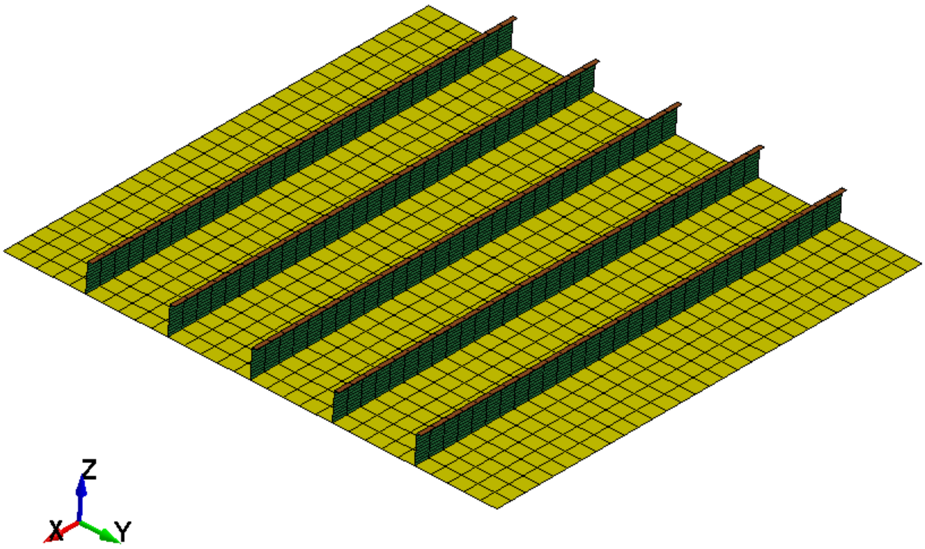

Figure 3.1: Finite element model of stiffened plate used for the quasi-static pressure analyses in LS-Dyna

3.2 Material Selection

The plate, webs and flanges are made of the same steel S355 material. The linear material properties of steel S355 are listed in table 3.2. With a steel density of 7850 kg/m^3, the total mass of the stiffened plate is 856 kg. Four materials with different plastic material behaviour have been applied for the quasi-static pressure-deformation curves from LS-Dyna. Their nonlinear material properties are described in table 3.3 and 3.4. Material 1 and 2 have the same plastic properties as the materials studied in Amdahl et al. (2017). Strain rate effects have been included in material 3. The strain rate effect parameters are based on the Cowper-Symonds model, and the strain rate parameters are chosen based on typical values for offshore steel structures. The nonlinear material properties of material 4 are found in RP C208 (DNVGL, 2013) for steel S355. In LS-Dyna, the materials have been modelled with the *Piece-wise Linear Plasticity* material formulation. In this material model, the true stress-true strain curves can be defined directly as input. If strain rate hardening is included, the strain rate sensitivity parameters are also defined in the material description. The true stress-true strain curves without strain rate effects are shown in figure 3.2.

Table 3.2: Linear material properties of S355 steel

Material type	$\rho [kg/m^3]$	E [GPa]	ν [-]	σ_0 [MPa]
Steel S355	7850	210	0.3	355

Table 3.3: Plastic material properties of steel S355

Material	Hardening	K [MPa]	n	E_t [MPa]	σ_{yield_2}[Mpa]	ϵ_{p_y2}	C[s^{-1}]	P
1	Linear	-	-	400	-	-	0	0
2	Power law	780	0.22	-	357	0.026	0	0
3	Power law	780	0.22	-	357	0.026	4000	5

Table 3.4: Nonlinear material properties of steel S355 from (DNVGL, 2013)

Material	σ_{prop}[Mpa]	σ_{yield}[Mpa]	σ_{yield_2}[Mpa]	ϵ_{p_y1}[-]	ϵ_{p_y2}[-]	K [Mpa]	n [-]
4	320	357	366.1	0.004	0.015	740	0.166

Material 4 neglects strain rate hardening effects, i.e. C and p = 0.

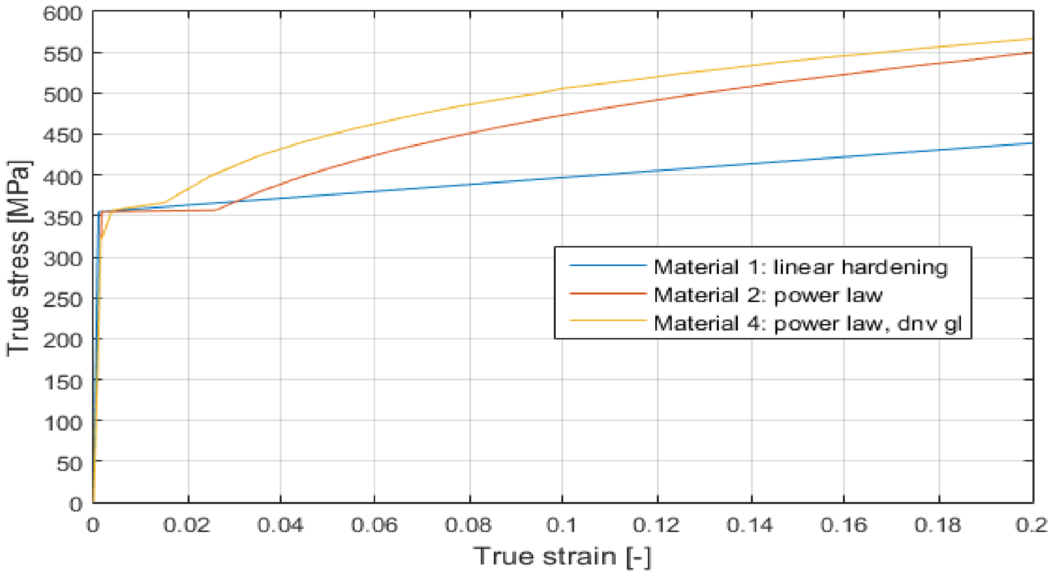

Figure 3.2: True stress-true strain curve for steel S355 with different nonlinear material properties

The stiffened plate is fully clamped in the transverse direction along the edge of the stiffeners. By fixing the panel ends against inward displacements, the plate will elongate as the lateral displacement increases. For large lateral deflections, the elongation of the plate gives rise to membrane forces in the longitudinal direction. The membrane forces will increase the load-bearing capacity of the plate for increasing lateral load. Membrane effects are expected to be important when the maximum, lateral deflection of the plate is in the same order as the plate thickness. Static analyses in LS-Dyna have been performed for materials 1-4 with no rotational or translational restrictions along the longitudinal boundaries. For material 2, static analyses have also been performed for longitudinal boundaries that are either clamped or simply supported, and not allowed to move in the in-plane direction.

3.3 Parameters for Analytical Resistance Curve

The resistance curves for the stiffened plate have been established based on the simplified method for large inelastic deformation resistance of stiffened plates subjected to lateral loads in Amdahl et al. (2017). When the stiffened plate is subjected to lateral loads, the plate will act as a bottom flange for the stiffener, and thus the stiffener and plate section will behave like a beam. In order to analyse the stiffened panel as a beam, the effective width of the plate flange between the stiffeners must be used as the width of the bottom flange. The effective flange can be found graphically in figure 3.3. The graph for more than N_p=5 point loads is used because the pressure is assumed to be evenly distributed. The ratio of the plate length and stiffener spacing is $L/s = 6$, which gives an effective flange approximately equal to the stiffener spacing.

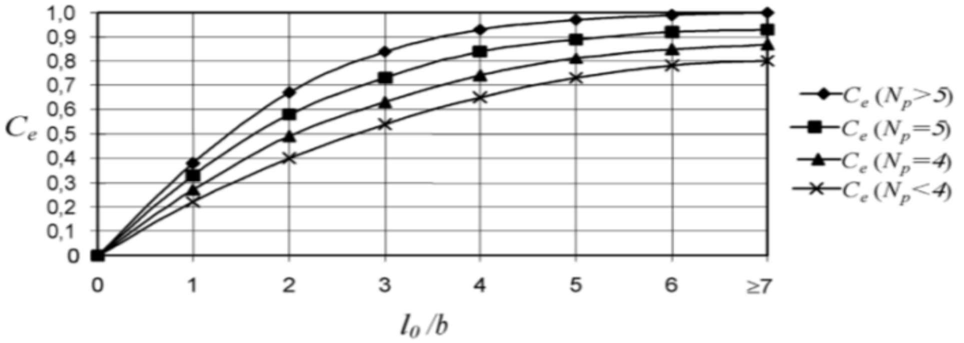

Figure 3.3: Coefficient for estimation of the effective flange $s_e = C_e s$ from RP C101 (DNVGL, 2015)

In the simplified approach, the only input for the material behaviour are the yield stress, Young's modulus and the steel density. The plastic mechanism of the stiffened plate is captured by the equations that describe the development of membrane forces and bending moments across the beam cross section.

The rotational boundaries of the beam are fixed, so β=2. For clamped beam ends, the simplified formulation assumes that the beam will collapse via a three hinge bending mechanism. The flexibility of the adjacent structure is neglected, i.e. only the second term in equation 2.25 for the translational axial stiffness k is included. The stiffness k_1 in the linear, elastic domain for the clamped beam is found in the tables from RP C204 (DNVGL, 2016a) in figure B.2. The non-dimensional translational spring stiffness factor is c=14.3. Because c $\gg$ 1, the resistance curve will coincide with the curve for c=inf for completely fixed boundaries. When the transverse boundary of the plate is completely fixed against inward translations the membrane effects will be large. The main resistance parameters from the simplified formulation are given in table 3.5.

Table 3.5: Structural parameters for the deformation resistance of the stiffened plate response for clamped beam

I [mm^4]	Ro [MN]	k_1 [MN/m]	w_{el} [mm]	M_p [MNm]	N_p [MN]	k [MN/m]	c	β
3.065E07	0.514	91.5	5.6	0.0964	2.3	906	14.3	2

3.4 Results from Static Analyses in LS-Dyna

3.4.1 Effect of Boundary Conditions and Plastic Material Properties

The quasi-static analyses of the stiffened panels were performed by gradually applying uniformly distributed pressure perpendicularly to the plates. The rate of the applied load was chosen so that the kinetic energy contributed to a small amount of the total energy to ensure that no dynamic effects were included. Figure 3.4 compares the static pressure-deformation curves for materials 1-4 from LS-Dyna with the resistance curves from the analytical formulation. The transverse boundaries are fixed against rotations and inwards displacement. No rotational or translational restrictions have been imposed along the longitudinal boundaries.

The deformation is measured as the vertical deflection of the node in the middle of the plate at the bottom of the middle stiffener. The simplified method is based on a rigid perfectly plastic material formulation. The elastic displacement w_{el} in table 3.5 is added to the plastic value to include the initial linear resistance domain in figure 3.4.

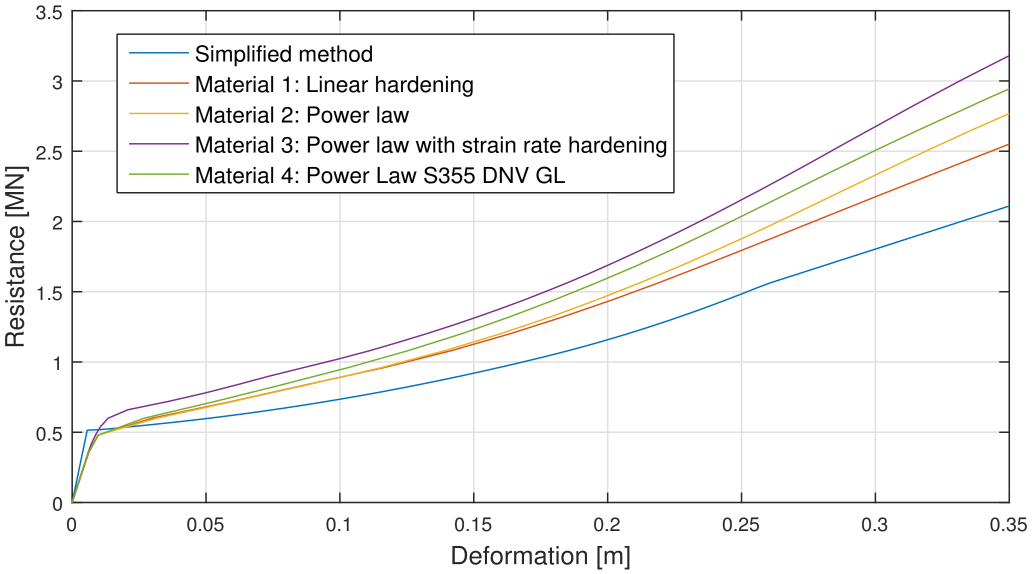

Figure 3.4: Static resistance-deformation curves from LS-Dyna for different plastic properties of steel compared with the resistance curve from the simplified formulation

Figure 3.4 clearly shows that the numerical static resistance curves do not coincide well with the predicted response from the simplified formulations. The simplified formulation produces a resistance curve that thoroughly underestimates the deformational resistance of the stiffened plate. The discrepancy between the analytical response and the response from LS-

Dyna increases with the amount of strain hardening in the material.

As the membrane action increases, the simplified model fails to predict the response. The linear hardening model of material 1 experience the least amount of strain hardening, and therefore has the best fit to the simplified method. Material 3, which is described by power law hardening with strain rate hardening effects, differs the most from the simplified resistance curve. Although the plastic collapse force in pure bending R_o is larger when strain rate effects are included, the slope of the resistance curve is not significantly affected by the strain rate hardening effects.

Figure 3.5 compares the static pressure-deformation curves from LS-Dyna and simplified method for different longitudinal boundary conditions. The transverse boundary is fixed against rotations and translations and material 2 is applied for all simulations.

When the longitudinal boundary is not allowed to move in the in-plane direction, the theoretical resistance curve underestimates the response twice as much as when the longitudinal boundary was free. This shows that the static pressure-deformation curves in the formulation are not very affected by the rotational constraint in the longitudinal direction, but depend heavily on the translational restriction of motion.

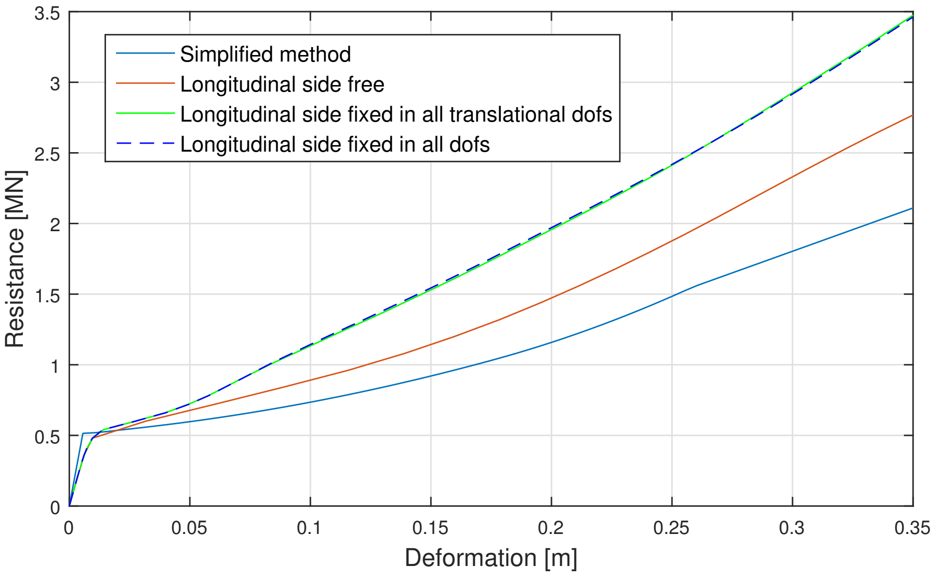

Figure 3.5: Static resistance-deformation curves for different longitudinal boundary conditions

With exception of material 3, which predicts a higher value for the plastic collapse force in pure bending R_0, the resistance curves from LS-Dyna have a similar response in the linear elastic stiffness domain. By differentiation of the pressure-deformation curves, the elastic stiffness k_1 in the elastic domain is obtained. The elastic displacement w_{el} is calculated from equation 2.29. The linear response parameters are given in table 3.6. The different plastic collapse forces for the FE analyses are approximately equal to the plastic collapse force predicted by the simplified method at 0.514 MN. However, the analytical linear stiffness for clamped beams at k_1=91.5 MN/m is 51.2 % larger than the linear stiffness obtained from the static analysis in LS-Dyna at approximately 60 MN/m. Thus, w_{el} from LS-Dyna is approximately 3.6 mm larger than estimated by the simplified method.

Table 3.6: Elastic response parameters from FEA static analysis

Material	Longitudinal boundary	R_o [MN]	k_1 [MN/m]	w_{el} [mm]
1,2,4	Free	0.54	60	9.00
3	Free	0.615	60.5	10.16
2	Fixed translational dofs	0.54	61	8.85
2	Fixed in all dofs	0.54	61	8.85

3.5 Discussion of Simplified Method

The simplified approach provides a conservative estimation of the deformation resistance of the stiffened panel subjected to lateral loads. The proposed model captures the initial bending capacity of the plate quite well, but as the lateral deflection increases and the membrane effects in the material become prominent, the capacity of the plate is underestimated. The discrepancy between the resistance curves from the analytical method and the analysis in LS-Dyna increases as the response approaches the pure tension stage.

The simplified formulation assumes a rigid perfectly-plastic material formulation. In the pure tension stage, where the plastic hardening may be significant, the simplified formulations still apply the yield stress σ_y instead of the flow stress σ_{flow}. When the plastic flow stress increases during plastic deformation, the strength of the material will increase. By neglecting the effect of strain hardening behaviour, the capacity of the plate will be underestimated by the theoretical approach. As expected, the deformation resistance of the panel with material 1, which has the least amount of hardening among the tested materials, is closest to the analytical resistance curve. The resistance curves for material 3 and 4 do not coincide well with the analytical method due to the large plastic hardening and strain rate hardening effects in the materials. The underestimation of the load-bearing capacity of the plate will be especially prominent in pure tension stage, where plastic hardening is significant.

In the elastic domain, the numerical and analytical resistance curves coincide well. The plastic collapse resistance R_0 is approximately the same for the numerical and analytical curves for most of the conditions in figure 3.4 and 3.5. The bending stiffness k_1 for the pressure-deformation curves in LS-Dyna is 35 % lower than k_1 from the simplified method. In the simplified approach, the linear stiffness is found for a clamped beam in RP C204 (DNVGL, 2016a) in table B.2. The lower linear stiffness in the FE-model indicates that that the boundaries of the FE-model does not act as completely fixed.

Material 1 and 2 are used as material models in LS-Dyna in Amdahl et al. (2017). In the numerical simulations, a stiffener with an effective flange is struck by a flat indentor with constant velocity. Several tests are performed for different widths and impact positions of the indentor. The numerical results show good agreement with the simplified method. As expected, material 1 has a slightly better fit to the analytical resistance curves due to the low degree of hardening.

In Amdahl et al. (2017), uniform loads were applied to the beam section with transverse boundaries fixed against rotation and horizontal displacements, and longitudinal boundaries completely free. When the uniform load was applied to the stiffened panel, the resistance was also underestimated by the simplified model. As expected, the difference between the analytical and numerical resistance curves was similar to the discrepancy between the curves in figure 3.4. In the simplified formulation, the deformation resistance to uniformly distributed loads may be approximated with an effective concentrated force $P = 0.5\rho L$. The approximation of the uniform load is derived based on similarity in the plastic bending collapse mechanism, but will not be completely satisfied in the membrane stage. Thus, the simplified formulation is better suited for patch- or point loads than for uniform loads. For a rigid perfectly-plastic analysis, all plastic deformations may be assumed to occur in plastic hinge locations. According to Amdahl (2005), a clamped beam subjected to uniform lateral pressure will collapse in a three-hinge bending mechanism with hinges located at the supports and in the middle of the beam. The theoretical three-point collapse mechanism differs from the observed deformation pattern of the plate, which follows a cosine shape.

The transverse boundaries of the panel have been restrained against in-plane motion for all of the structural analyses in LS-Dyna in this chapter. If the longitudinal boundaries also are restrained against inwards motion, a bi-axial membrane stress state for the plating will occur. The present version of the simplified model is not applicable for stiffened plates with bi-axial membrane action because the method assumes that the longitudinal edges are not fixed against inward displacements. The simplified model may be further developed to account for transverse membrane contributions. One possible approach for including bi-axial membrane effects could be by increasing the term that is governed by the tension force in equation 2.27.

Some of the main contributions to the discrepancy between the theoretical and numerical resistance curves have been identified. The simplified method is better suited for point loads than uniform loads. This becomes especially evident in the membrane stage. Hardening and strain rate hardening effects are not accounted for in the analytical formulation, which results in a severe underestimation of the capacity of the plate. The current version of the analytical approach is also not able to capture the effect of transverse membrane effects.

Chapter 4

Drop Tests for 3D Stiffened Panels

In this chapter, drop test simulations with a 3D stiffened panel have been performed in LS-Dyna. The FE-model consists of a stiffened plate with the same dimensions as the model in chapter 3. In the drop tests, the stiffened plate falls through the air with an initial velocity towards a calm water surface. Because the FSI analyses are very computationally demanding, the drop tests simulations have been conducted on the cluster of NTNU's supercomputer "Vilje".

4.1 ALE Formulation in LS-Dyna

In LS-Dyna, the impact of the stiffened plate on the fluid surface is simulated using an ALE-formulation and an FSI-algorithm. The water and air are modelled with an Eulerian formulation, while the stiffened plate is modelled with a Lagrangian formulation. In the coupling algorithm for the fluid-structure impact, the fluids are assigned the role of master elements, while the elements in the steel plate are given the role of slave elements.

The water and air are modelled with an *ALE single material and void* formulation. In this approach, the water is modelled as an Eulerian material, while the air initially surrounding the Lagrangian stiffened plate is modelled as a vacuum. It is assumed that modelling the air as a vacuum is a valid approximation due to the low density of water and because the air has less influence on the deformation of the plate during the impact. By modelling the water as a void, the problem of air entrapment beneath the plate is not considered.

Water is modelled as a solid Eulerian null material with properties shown in table 4.1. Null materials are commonly used in LS-Dyna to model fluids. The pressure-volume relation in the fluid is described by the EOS Gruneisen equation for water from table 2.2.

Table 4.1: Material properties for water in LS-Dyna

	Material type	Density $\rho[kg/m^3]$	Dynamic viscosity μ at 4°C [-]
Sea water	Null	1025	0.00167

4.2 Finite Element Model in Drop Test

The stiffened panel in the numerical drop tests has the same structural dimensions as the stiffened panel in chapter 3. In order to minimise rigid body accelerations and to ensure that the reduction of the velocity is small during the impact, a rigid plate has been added on top of the panel. The rigid plate has the same surface area as the deformable plate and is connected to the steel plate via elastic shell elements at the plate boundaries. The 3x3 m^2 deformable steel plate is assumed to be a part of a larger floating structure. Thus, the additional mass from the rigid panel above the deformable plate provides a realistic representation of a stiffened surface on a large structure subjected to horizontal wave impacts.

The results from the drop tests will be used to verify the simplified methods for response prediction in the following chapter. The boundary conditions for the stiffened plate are equal to the boundary conditions used in the static analysis in chapter 3. This means that the longitudinal boundaries are free, and the transverse boundaries are fixed against rotations and in-plane displacements. The elastic shell boundaries provide some extra stiffness for the translational deformation of the plate. The additional stiffness contribution is assumed to have a negligible effect on the maximum lateral deflection.

When the stiffened plate is subjected to lateral loading, it will experience both membrane stresses and bending moments. Four-noded shell elements are therefore a good choice for the finite elements in the panel. The fluid elements are modelled with solid 8-noded elements. The fluid domains are modelled as two rectangular boxes. The nodes at the intersecting surfaces of the water and air domains are merged. Before the simulation begins, the stiffened panel is located close to the water surface inside the void domain.

The convergence of the FSI problem depends on parameters such as the mesh size of the Lagrangian and Eulerian elements, the size of the fluid domain, and the coupling algorithms between the master and slave parts. In chapter 7, comprehensive convergence tests for the variables above were carried out for an unstiffened plate. These results showed that the ideal finite element discretisation was obtained when the fluid and plate elements had the same mesh size. The fluid domains should be large enough to capture the effects of the fluid-structure impact without demanding a very high computational time. The convergent fluid domain for the unstiffened plate was scaled and applied for the stiffened plate. The results from a convergence test for the fluid and structural mesh refinement is shown in figure 4.1.

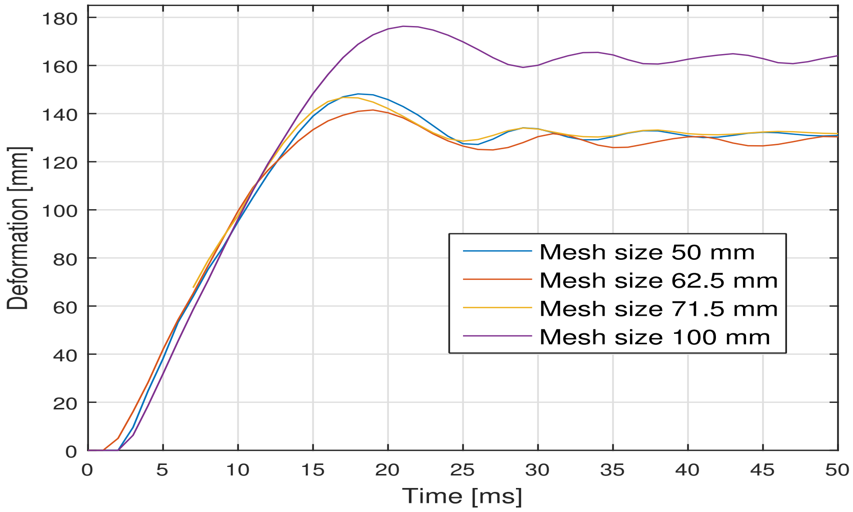

Figure 4.1: Convergence test for FSI drop test problem. Same elements size for master and slave elements

The drop test simulation in LS-Dyna has converged for a mesh size of 50 mm for both the quadratic plate shell elements and the solid fluid elements. The mesh sizes for the stiffened plate are summarised in table 4.2. The parameters n_W and n_L are the number of finite elements in the width and length direction of the structural part. The length, width and height of the water and air domains are 7x7x2.5 and 7x7x1 m^3, respectively.

Table 4.2: Finite element discretisation of the stiffened drop test panel

Part	B [m]	L [m]	t [mm]	n_W	n_L	Material
Plate	3	3	8	60	60	1
Web	0.165	3	10	22	60	1
Flange	0.0274	3	30	2	60	1
Boundary plate	0.2	3	8	1	60	5
Rigid plate	3	3	8	60	60	6

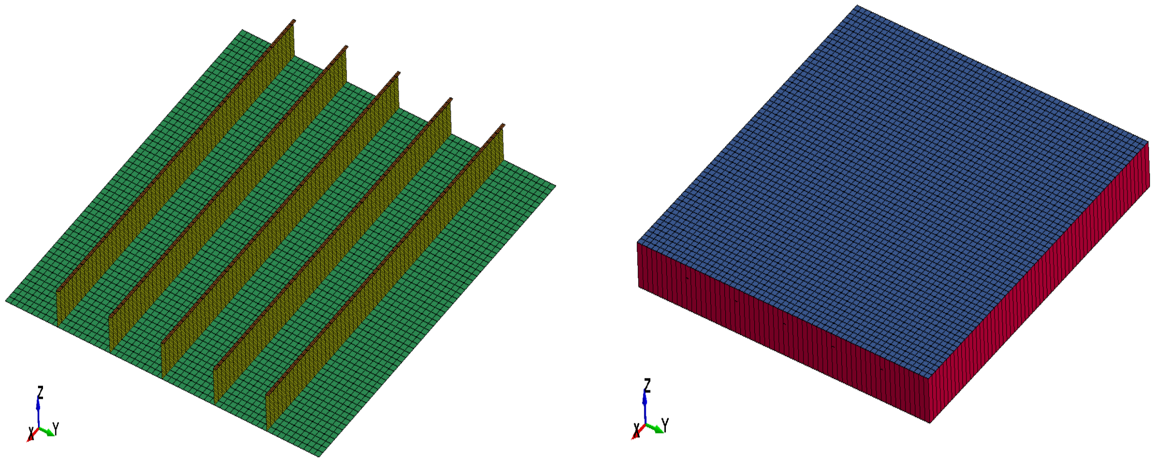

(a) Stiffened plate **(b)** Panel with rigid top and elastic boundary

Figure 4.2: Discretised model of stiffened plate used in the drop tests in LS-Dyna

The material used for the stiffened plate in the drop tests is steel S355 as defined in RP C208 (DNVGL, 2013), which is identical to material 4 in table 3.4. In table 4.3, the linear material properties of the stiffened plate, rigid top plate and elastic boundary are given. The mass of the rigid panel has been chosen so that the reduction of the velocity during the impact is negligible.

Table 4.3: Linear material properties for the dropped panel

Material	Material type	$\rho [kg/m^3]$	E [GPa]	ν [-]	σ_0 [MPa]
4	Elasto-plastic	7850	210	0.3	355
5	Elastic	7850	210	0.3	355
6	Rigid	1.38E+06	210	0.3	355

4.3 Conduction of Drop Tests

The stiffened plate was dropped 10 mm above the free surface. Drop tests with both flat and inclined plates has been investigated. The chosen impact angles were 0 ° and 3 ° with the longitudinal edge closest to the surface. According to Faltinsen (1990), hydroelastic effects are not as important for impact angles larger than 5°. The inclined impact angle was chosen so that hydroelastic effects should be included. Additionally, the impact angle should be sufficiently bigger than the flat plate, so that it would be easy to observe differences between the two impact cases. Within these limitations, the 3° impact angle have been chosen arbitrarily.

A velocity of 11.19 m/s was identified as the particle velocity corresponding to the most critical sea state in terms of negative air gap in Skjeggedal (2017), and was therefore chosen as the vertical impact velocity for the drop tests.

The pressure history across the plate was extracted from FSI-sensors attached to the segments on the Lagrangian plate surface. The output-file contained the recorded pressure in each sensor segment. Due to the large pressure variation across the impact area, the pressure distribution was taken as the average pressure across the entire plate surface.

4.4 Results from Numerical Simulations

The average pressure variation for the stiffened panel with 0 ° and 3 ° angle is shown in figure 4.3. The peak pressure for the elasto-plastic plate with zero impact angle is 2.4 MPa. For the plate with 3 ° impact angle, the maximum pressure is 0.65 MPa, but is not located at a sharp peak as for the plate with zero impact angle.

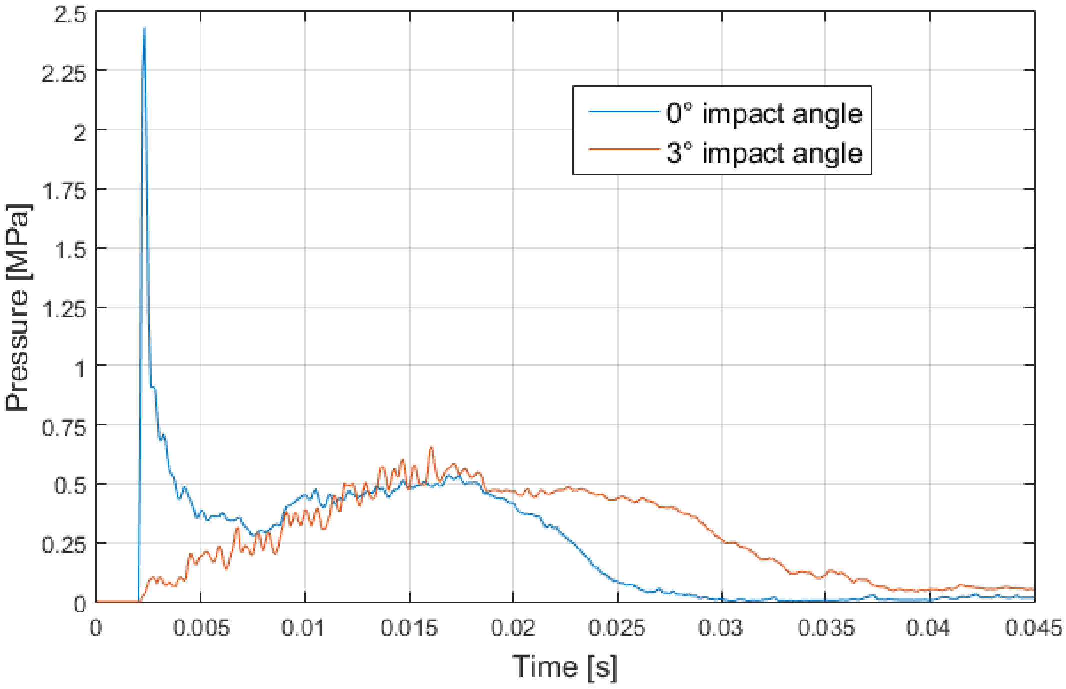

Figure 4.3: Pressure-time variation with 0° and 3° impact angle and velocity 11.19 m/s

The duration of the pressure impulse increases with increasing impact angle. For 0 ° angle, the duration is $t_d \approx 23$ ms, while for the plate with 3 ° angle, the duration is $t_d \approx 33$ ms. The wet eigen period of the plates was estimated from oscillations of the upper strain in the x-direction. The elasto-plastic natural period for the flat plate was approximately 10 ms, while the eigen period of the inclined plate was slightly longer at 11 ms. It was difficult to observe a distinct difference in the eigen period for the two plates. The relationship between the duration of the impulse and the wet eigen period is t_d/T_n= 2.3 for the flat plate, and t_d/T_n= 3.0 for the inclined plate. According to the loading domain categories from RP C204 (DNVGL, 2016a), the response for the plate with 0 ° impact angle is in the dynamic domain, while the plate with 3 ° impact angle is at the upper limit of the dynamic domain, close to the quasi-static region. The pressure impulses for the 0 ° plate is 10 $kPas$, and 11.5 $kPas$ for the 3 ° plate.

In figure 4.4, the lateral deformation of the plates in z-direction have been visualised. For the drop test with zero impact angle, the maximum lateral deformation occurs in the middle of the plate, while for the inclined plates, the maximum deformation is shifted from the middle. In figure 4.4(e) and (f), the deformation patterns at maximum deflection are shown. The figures show that the deformation pattern changes during the impact event. Assuming a constant mode shape can therefore yield inaccurate results.

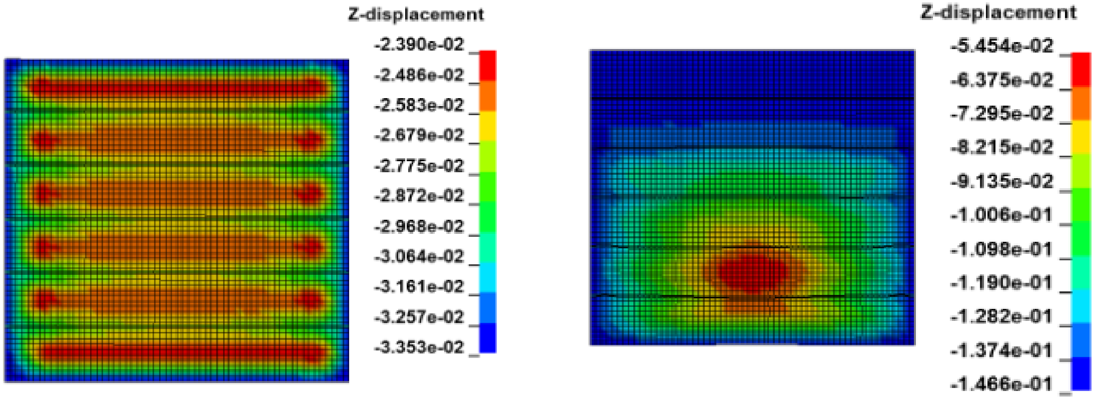

(a) t=3 ms, $\beta = 0°$

(b) t= 13 ms, $\beta = 3°$

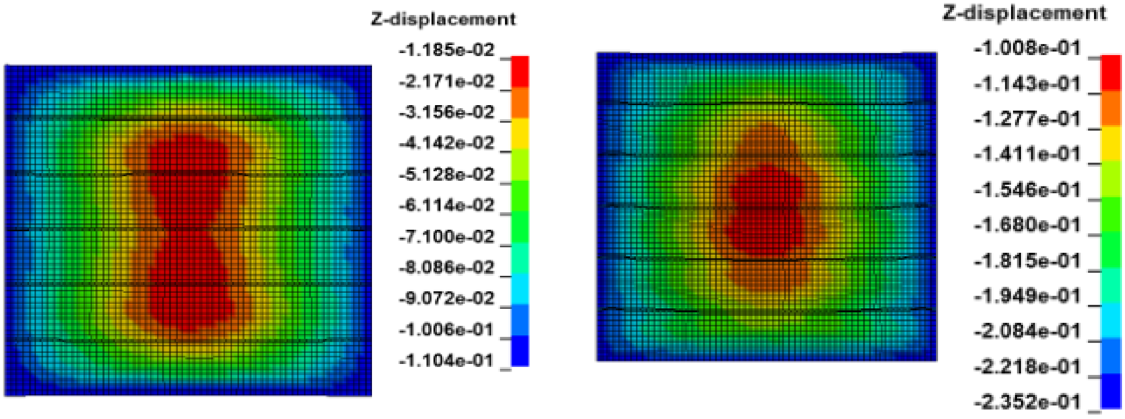

(c) t=10 ms, $\beta = 0°$

(d) t= 21 ms, $\beta = 3°$

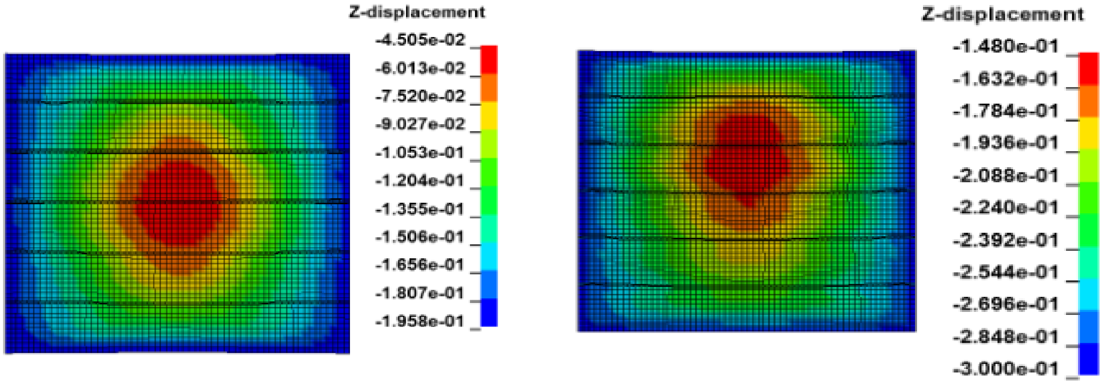

(e) t=18 ms, $\beta = 0°$

(f) t=27 ms, $\beta = 3°$

Figure 4.4: Lateral deformation pattern for elasto-plastic plate with 0° impact angle (left column) and 3° impact angle(right column)

The maximum deformation for the plates with 0 ° angle is 148 mm, while the max deformation for 3 ° angle is 136 mm. The deformation in the middle of the inclined plate is 131 mm. The graphs of the maximum deformation are shown in figure 4.5.

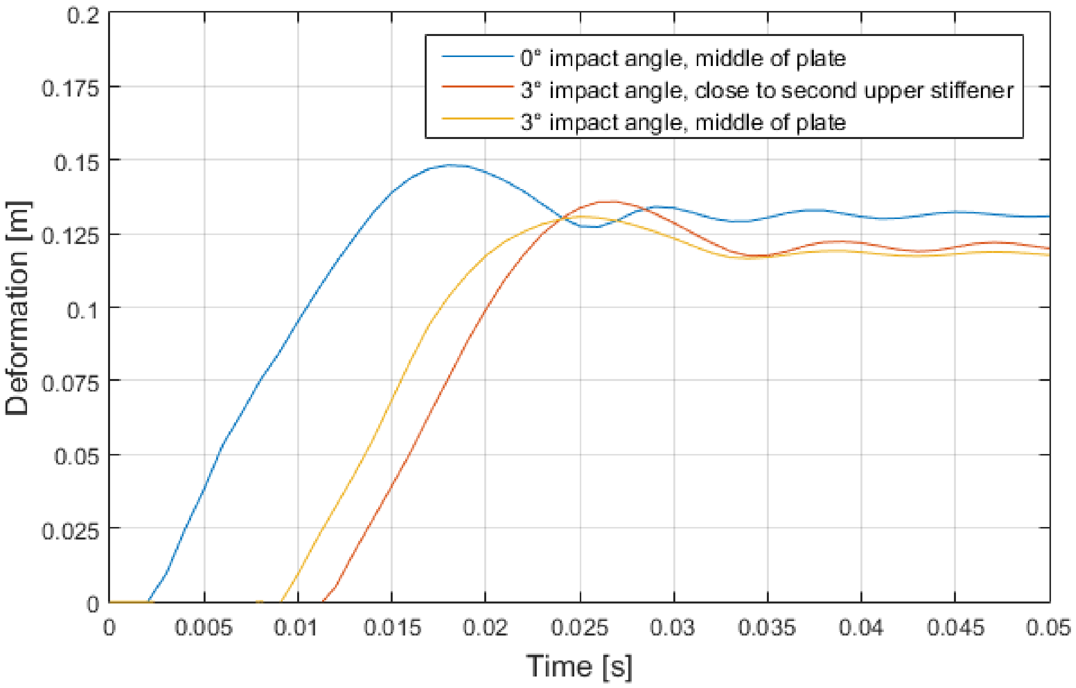

Figure 4.5: Maximum lateral plate deformation with 0° and 3° impact angle and velocity 11.19 m/s

In figure 4.6, the pressure history and the deflection at the location of the maximum deformation are plotted for the same time scale. For both impacts, the maximum deformation is reached close to the end of the pressure impulse. The overlap between the load and deformation variation shows that the drop tests should be categorised as dynamic impacts.

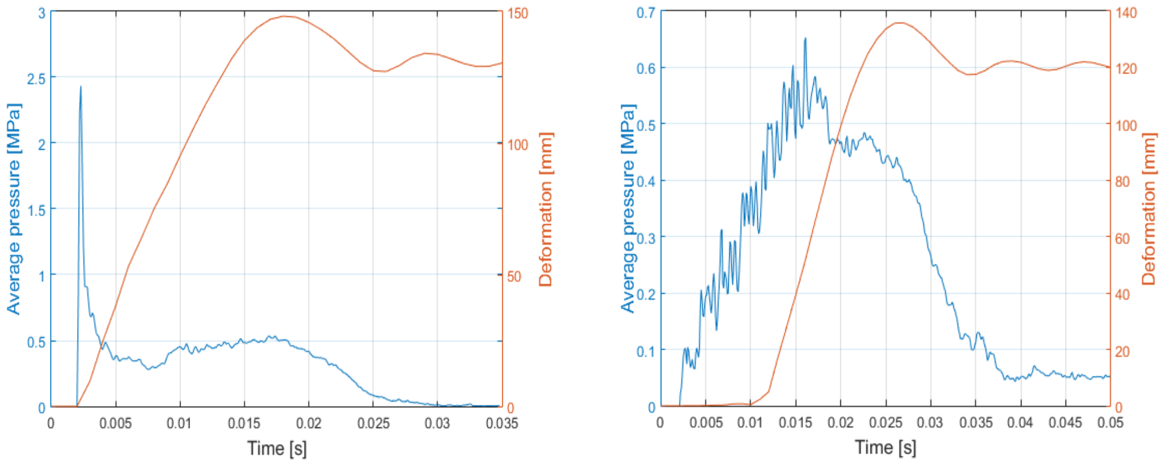

(a) 0° impact angle **(b)** 3° impact angle

Figure 4.6: Pressure and response history for drop test with stiffened plate

Figure 4.7 show the variation of von Mises stress in the plate at the stage of maximum deformation for the plate with 0° impact angle. The effective stress in the middle of the plate is either above or close to the yield stress $\sigma_y = 355$ MPa. Except for a few localised stress concentrations near the near the bottom of the clamped stiffener edges, the stress level in the plate is below the ultimate tensile strength $\sigma_{ts} = 465$ MPa.

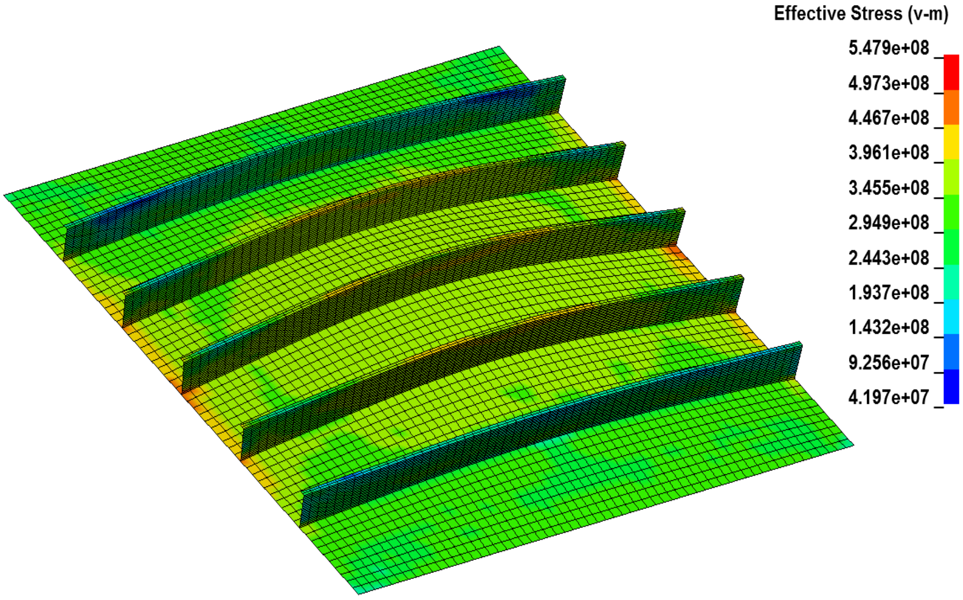
Effective Stress (v-m)
5.479e+08
4.973e+08
4.467e+08
3.961e+08
3.455e+08
2.949e+08
2.443e+08
1.937e+08
1.432e+08
9.256e+07
4.197e+07

Figure 4.7: Von mises stress at 18 ms for stiffened plate with zero impact angle

Chapter 5

Single Degree of Freedom Analogy for Drop Test Response

In this chapter, the SDOF analogy for response prediction of explosion loads in RP C204 (DNVGL, 2016a) is applied for estimation of the maximum lateral deformation of a stiffened plate subjected to slamming loads. The resistance curves from chapter 3 are applied in the simplified method. The prediction of the maximum deformation will be compared with the numerical drop test results in chapter 4 for the drop tests with 0° and 3° impact angle.

5.1 Beam Analogy for Stiffened Plate

When a lateral pressure acts on a stiffened plate, it is assumed that the stiffener with the effective flange can be approximated as a beam. According to RP C204 (DNVGL, 2016a), stiffened plates may be treated as beams as long as the stiffeners remain stable against local or torsional buckling or tripping. The SDOF analogy in RP C204 assumes that the dynamic interaction between the effective plate flange and stiffener profile can be neglected.

The dynamic equations of motion for the beam can be transformed into the equivalent SDOF system described by equation 5.1.

$$K_{lm}(M+M_a)\ddot{y}+k_e=F(t) \tag{5.1}$$

where M and M_a are the structural and added mass, K_{lm} is the load-mass factor from table B.2, and k_e is the equivalent stiffness from table B.2.

5.2 Calculation of Added Mass for Rectangular Plate

The analytical approach for calculation of added mass for flexible beams by Faltinsen (1999) is applied to the stiffened plate. The boundary conditions are the same as for the plate in chapter 4, i.e. the plate is clamped along the stiffener ends, and the longitudinal edges can move freely. As mentioned in section 2.4.5, the primary mode shape of the plate will follow a cosine pattern along the length of the beam if the longitudinal edges are free to move. The added mass may in this case be calculated according to equation 2.13. If the longitudinal sides are fixed, there will be a cosine mode shape in both transverse and longitudinal direction. Although no rotational or translational restrictions have been imposed directly on the longitudinal boundaries of the stiffened plate, the elastic shell boundary and the initial velocity will reduce the ability of the longitudinal egds to move freely. The plots of the lateral deflection in figure 4.4 show that the final deformation pattern of the panel with zero impact angle follows a cosine pattern in both x- and y-direction. Thus, the estimated added mass is based on a cosine mode shape in both directions and is calculated according to equation 2.34. The added mass for the stiffened plate is 1974 kg. For comparison, the uni-directional cosine pattern gave an added mass of 4871 kg. The structural mass of the stiffened plate, without the elastic boundary and rigid top, is 856 kg.

In order to verify the calculated added mass, a comparable plate is loaded with the elasto-plastic pressure history. It is assumed that the stiffeners will have a negligible effect on the added mass because most of the added mass effect arises from the motion of the plate in heave direction. The added mass is included in the comparable plate by increasing the mass density of the plate to ρ_a. The maximum deformation of the comparable plate was less than 10 mm lower than the drop test deflection. Some differences in maximum deformation was expected because the average pressure history is applied. Due to the small deviation between the predicted deformation, the approximated value of the added mass at 1974 kg is assumed to be a sufficiently correct estimate.

In section 3.3, the effective flange of the beam was estimated to be equal to the stiffener spacing s=0.5 m. Because the total width of the stiffened plate is 3 meters, the added mass for a stiffener section is the total mass divided by six. This yields an added mass of 329 kg for the beam section. The structural mass for the effective stiffener and plate flange is 152.5 kg. Thus, the total mass of the beam section in the SDOF analysis is 481.5 kg.

5.3 SDOF Parameters from Analytical Resistance Model

The analytical resistance parameters for a clamped beam estimated from the simplified approach have been summarised in table 3.5 in chapter 3. The nondimensional spring stiffness c= 14.3$\approx \infty$, which means that the ends are completely fixed. The response parameters in the elastic resistance domain are summarised in table 5.1.

Table 5.1: Analytical resistance parameters in the elastic domain for the stiffened plate

R_0 [MN]	w_{el} [mm]	k_1 [MN/m]
0.514	5.6	91.5

The equivalent linear stiffness k_e and the elastic load-mass factor K_{lm} are found in table B.2 in appendix B for a clamped beam subjected to uniform pressure. The structural and added mass for the section multiplied by K_{lm} are given in table 5.2.

Table 5.2: Generalised mass and stiffness in elastic domain for the clamped beam in SDOF analysis

	K_{lm}	$\overline{M}$[kg]	$\overline{M_a}$ [kg]	k_e [MN/m]
Elastic	0.77	117.4	253.3	71.3

The parameters in table 5.2 are inserted in equation 5.1 for estimation of the wet elastic eigen period. The analytical eigen period is T_n = 14.3 ms, which is larger than the eigen period from LS-Dyna at T_n = 10 ms.

5.4 SDOF Parameters from FEA Resistance Model

The response parameters in the initial linear resistance domain from the FEA analysis are summarised in table 5.3.

Table 5.3: FEA resistance parameters in the elastic domain for the stiffened plate

R_0 [MN]	w_{el} [mm]	k_1 [MN/m]
0.54	9	60

The load-mass factors for a clamped beam with uniform pressure can be found in table 5.4. The stiffness coefficients k_1, k_2 and k_3 for the tri-linearisation of the resistance curves, shown in figure 2.7, are found by differentiation of the resistance curves with respect to the deformation.

Table 5.4: Mass and stiffness for the clamped beam in SDOF analysis

	K_{lm}	$\overline{M}$	$\overline{M_a}$	k [MN/m]
Elastic	0.77	117.4	253.3	60
Elasto-plastic	0.72	109.8	236.9	4.5
Plastic	0.66	100.6	217.1	6.8

The variables in table 5.3 are inserted in equation 5.1 for estimation of the wet elastic eigen period. The elastic wet eigen period is calculated as T_n = 0.0156 s, which is also larger than the elastic natural period observed from the drop tests.

5.5 Response Calculation in Biggs Charts with SDOF analogy

According to RP C204 (DNVGL, 2016a), the maximum displacement of a SDOF system subjected to a triangular pressure load can be calculated from Biggs response charts. A triangular load pulse with duration t_d is therefore fitted to the force-time history from the numerical drop tests. The force variation on the stiffener section is obtained by multiplying the pressure variation from LS-Dyna with the section plate area A=1.5 m^2. Because the maximum response is dependent on the impulse and not the peak pressure (Faltinsen, 2005), the total impulse for the triangular and numerical load curve should be equal. In figure 5.1 and 5.2, the FEA and analytical resistance curves have been plotted along with tri-linear resistance curves with different stiffness k_3. The values of k_1 in the tri-linearisation are found in table 5.1 and 5.3. In figure 5.1, the FEA resistance curve from LS-Dyna is in the middle of the curves $k_3 = 0.1k_1$ and $k_3 = 0.2k_1$. In figure 5.2, the best tri-linear idealisation of the resistance curve from the analytical method is with $k_3 = 0.1k_1$, although the deviation between the two curves is quite large.

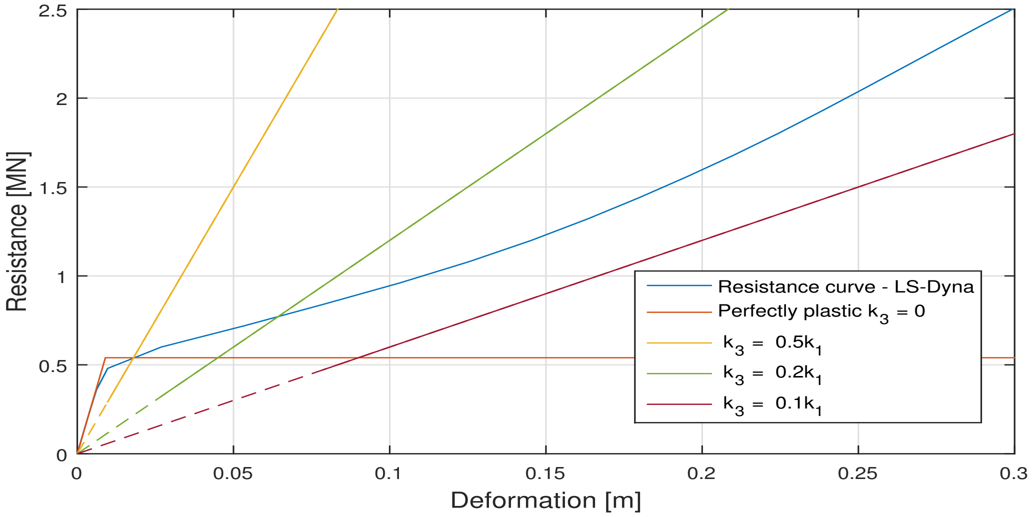

Figure 5.1: Resistance curve for the stiffened steel plate obtained from static analysis in LS-Dyna compared with a standard tri-linearisation of the resistance curves with k_1 = 60 MN/m

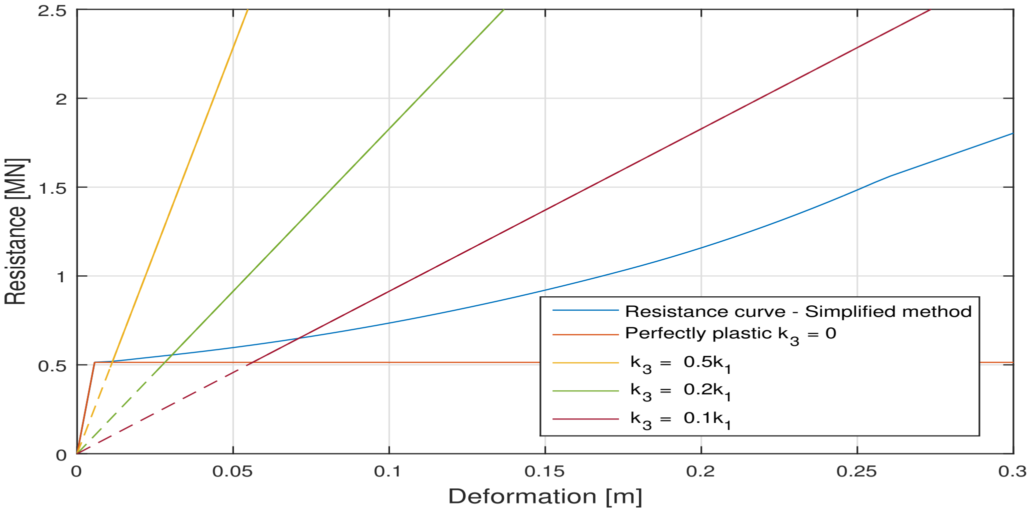

Figure 5.2: Resistance curve for the stiffened steel plate obtained from the simplified approach compared with a standard tri-linearisation of the resistance curves with k_1 = 91.5 MN/m

The Biggs charts in RP C204 (DNVGL, 2016a) have only included a standard selection of R_{el}/F_{max} curves. If the calculated R_{el}/F_{max} relation cannot be directly found in the Biggs chart, interpolation is required. The interpolation introduces uncertainty to the results. Instead of finding the maximum result graphically from the standardised Biggs charts, a Fortran program made by Jørgen Amdahl is applied to plot the Biggs response curves. The input in the Fortran program is a non-dimensional, normalised force-time curve and resistance-deformation curve. The force-time curve has a maximum force amplitude F_{max} = 1. The plastic collapse resistance in bending R_{el} will then be equal to the relationship R_{el}/F_{max}. The

Fortran program was successfully verified against Biggs charts in RP C204 (DNVGL, 2016a) and Norsok Standard (2013) N004.

5.6 Response for Drop Test with 0° Impact Angle

In figure 5.3, a triangular load curve with rise time $0t_d$ approximates the force variation from the drop test with zero impact angle in section 4. The impulses are equal in magnitude when the equivalent force amplitude F_{max} = 1.31 MN. The duration of the flat impact in LS-Dyna was t_d=23 ms, and the maximum deflection was 148 mm. The Biggs response parameters from the FEA and analytical resistance models are presented in table 5.5 and 5.6, respectively.

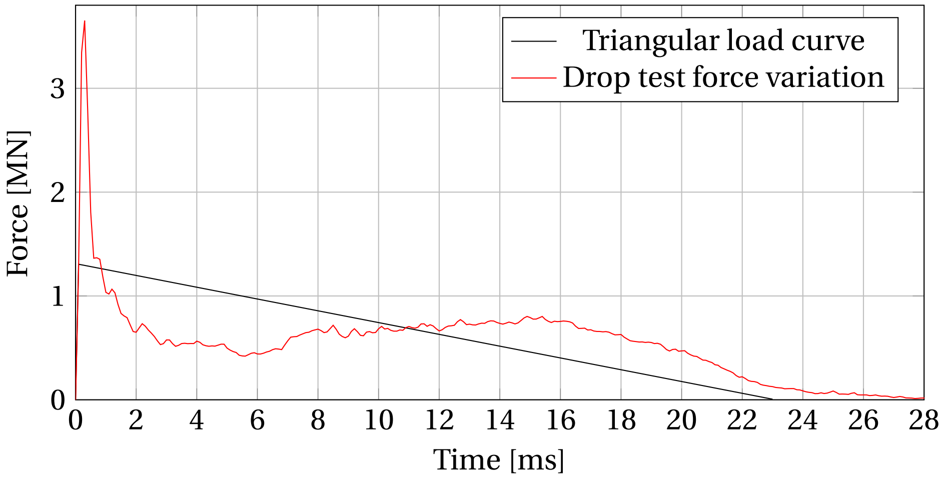

Figure 5.3: Triangular load pulse with $0t_d$ rise time fitted to drop test pressure-time history for the stiffened plate with 0° impact angle

Table 5.5: Summary of the SDOF response from Biggs chart for the plate with FEA resistance model and $0t_d$ rise time

F_{max} [MN]	R_{el} [MN]	$\frac{R_{el}}{F_{max}}$	$\frac{t_d}{T_n}$	k_3	$\frac{w_{max}}{w_{el}}$	w_{max} [mm]	Relative difference from drop test w_{max} [%]
1.31	0.54	0.41	1.47	$0.1k_1$	23.2	209	41.1
				$0.2k_1$	14.8	133	-9.9

Table 5.6: Summary of the SDOF response from Biggs chart for the plate with analytical resistance model and $0t_d$ rise time

F_{max} [MN]	R_{el} [MN]	$\frac{R_{el}}{F_{max}}$	$\frac{t_d}{T_n}$	k_3	$\frac{w_{max}}{w_{el}}$	w_{max} [mm]	Relative difference from drop test w_{max} [%]
1.31	0.514	0.394	1.61	$0.1k_1$	26.5	149	0.6

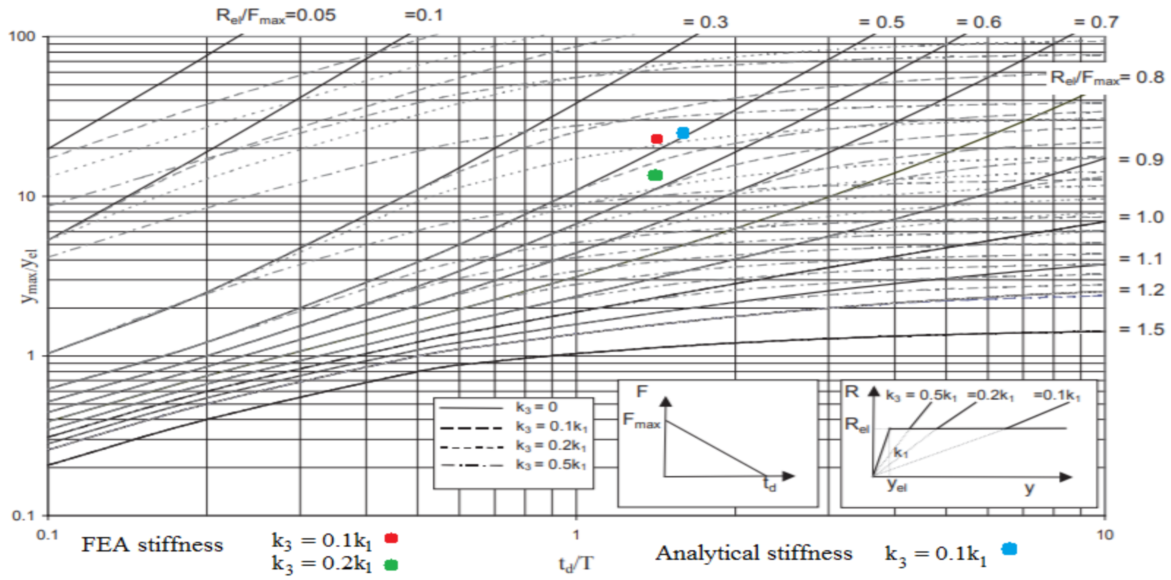

Figure 5.4: Biggs chart in RP C204 for dynamic response of a SDOF system subjected to a triangular load with 0t_d rise time

5.7 Response for Drop Test with 3° Impact Angle

In figure 5.5, the force-time variation from the drop test with 3° impact angle in chapter 4 is approximated with a triangular load pulse with rise time 0.5t_d. The maximum load F_{max} occurs after half the duration of the pressure impulse. The force impulses are equal when F_{max}=1.05 MN. The duration of the impact was t_d=33 ms, and the maximum plate deflection from LS-Dyna was 136 mm. The Biggs response parameters from the FEA and analytical resistance models are presented in table 5.7 and 5.8, respectively

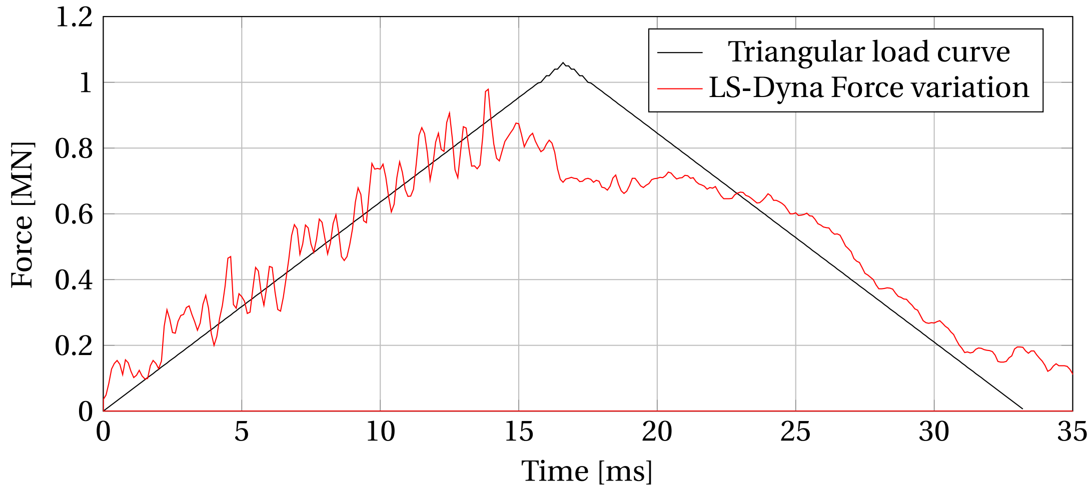

Figure 5.5: Triangular load pulse with 0.5t_d rise time fitted to drop test pressure-time history for the stiffened plate with 3° impact angle

Table 5.7: Summary of the SDOF response from Biggs chart for the plate with FEA resistance model and $0.5t_d$ rise time

F_{max} [MN]	R_{el} [MN]	$\frac{R_{el}}{F_{max}}$	$\frac{T_d}{T_e}$	k_3	$\frac{w_{max}}{w_{el}}$	w_{max} [mm]	Relative difference from drop test w_{max} [%]
1.05	0.54	0.51	2.11	$0.1k_1$	20.3	183	34.4
				$0.2k_1$	12.9	116	-14.3

Table 5.8: Summary of the SDOF response from Biggs chart for the plate with analytical resistance model and $0.5t_d$ rise time

F_{max} [MN]	R_{el} [MN]	$\frac{R_{el}}{F_{max}}$	$\frac{T_d}{T_e}$	k_3	$\frac{w_{max}}{w_{el}}$	w_{max} [mm]	Relative difference from drop test w_{max} [%]
1.05	0.514	0.49	2.3	$0.1k_1$	23	129	-5

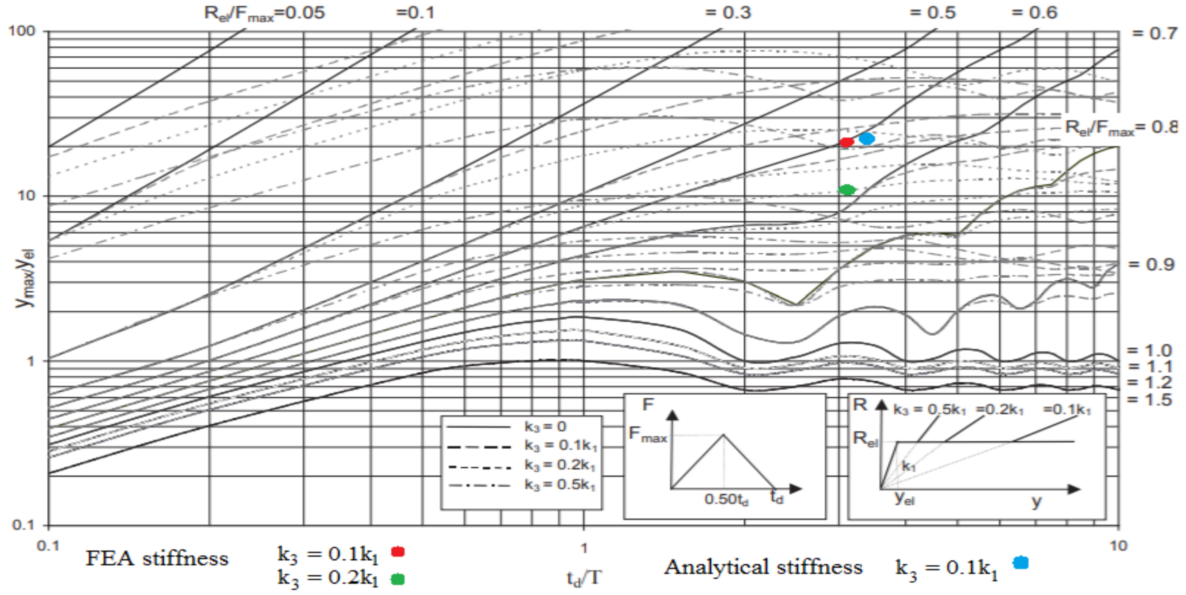

Figure 5.6: Biggs chart in RP C204 for dynamic response of a SDOF system subjected to a triangular load with $0.5t_d$ rise time

5.8 Modified Biggs Response Charts

The standard tri-linearisation of the resistance curves in figure 5.1 and 5.2 shows that the response will be either overestimated or underestimated depending on the choice of k_3. The triangular load approximation in figure 5.5 is a good fit for the force variation from the drop test with 3° impact angle, but the triangular shape with $0t_d$ in figure 5.3 does not resemble the force variation from the 0° drop test. It is of interest to investigate how the prediction of the maximum response is affected if more precise approximations of the real load and resistance curve are applied.

Figure 5.7 shows the improved tri-linear approximation to the resistance curves from the simplified method and the FE analysis in LS-Dyna. The approximation in the elastic domain follows the resistance curves exactly. In the elastic-plastic domain, k_2=0 for the tri-linear approach. In this region, the approximation differs from the actual resistance curves, especially for the resistance curve from FEA. The starting point of the plastic stage and the corresponding stiffness accounting for membrane effects, k_3, are chosen so that the approximation coincides as well as possible with the real resistance curves.

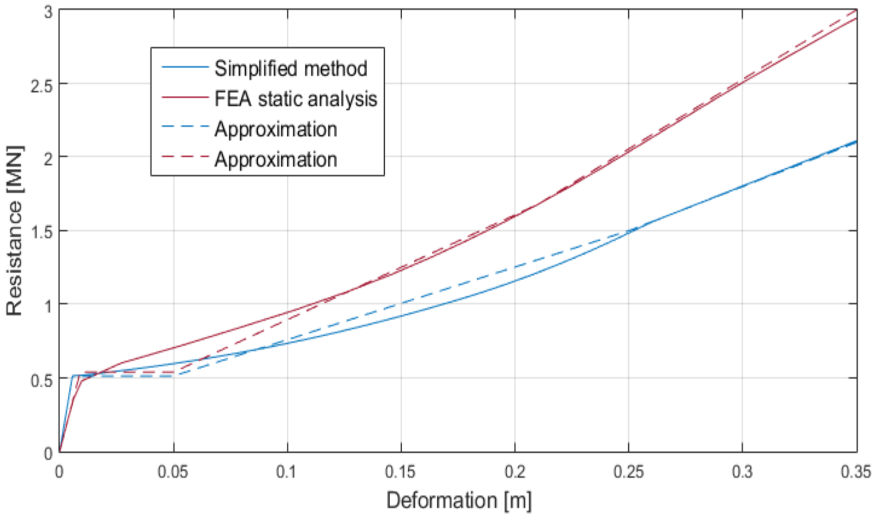

Figure 5.7: Modified tri-linear approximation to the theoretical and FEA resistance curve for the stiffened plate

Figure 5.8 shows the modified approximation of the triangular pressure pulse to the real pressure histories from the drop tests. The approximated curves follow the shape of the pressure variation and are not necessarily triangular, but the total impulse should be equal to the drop test impulse. For the 3° deadrise angle, the fitted load curve is almost triangular.

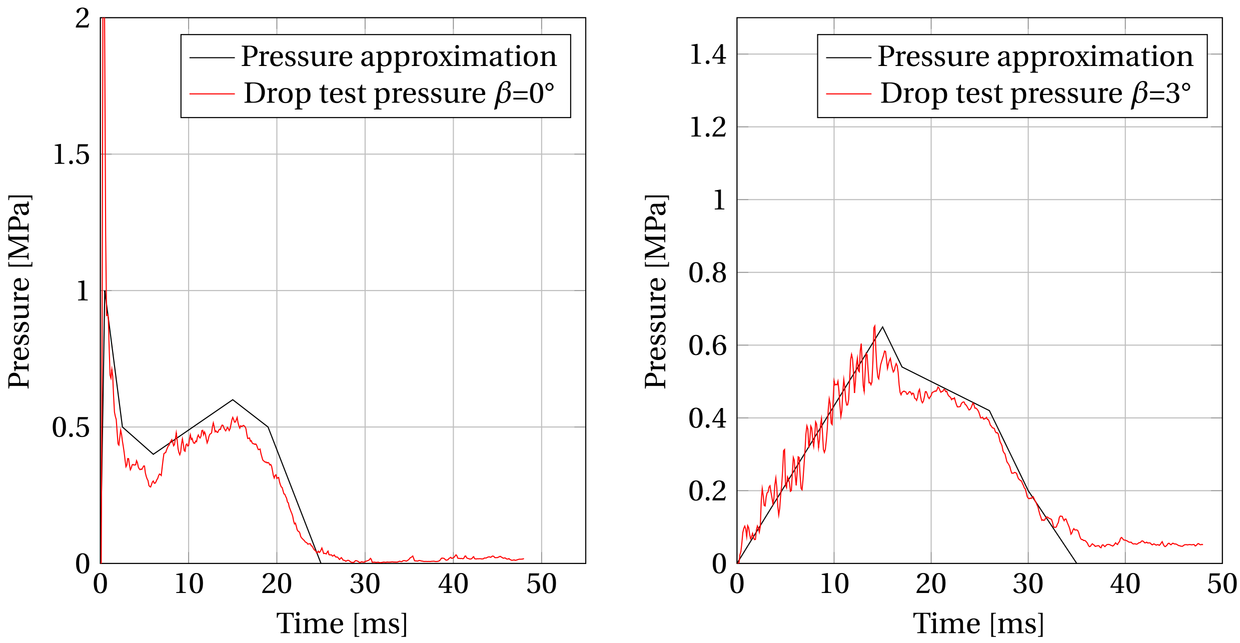

Figure 5.8: Modified "triangular" load history for the pressure history from the drop tests in LS-Dyna

In table 5.9, the different test combinations for the input in the Biggs curves in Fortran are listed. *Standard* refers to the tri-linear resistance curves in figure 5.1 and 5.2, and the triangular load curves in figure 5.3 and 5.5. *Modified* refers to the approximated resistance curves in figure 5.7, and the pressure approximations in figure 5.8.

Table 5.9: Explanation of graphs in numerical Biggs charts in figure 5.9, 5.10 and 5.11

—	Standard triangular load and resistance curve according to Biggs charts in RP C204
—	Modified load curve, standard resistance curve
—	Modified resistance curve, standard load curve
—	Modified load and resistance curve
—	Intersection of actual w_{max} from drop test in LS-Dyna

Figure 5.9 shows the Biggs chart for a SDOF system corresponding to the drop test of the stiffened panel with 0 ° impact angle. The resistance curve applied in the Biggs chart in figure 5.9 is found from the FE analysis in LS-Dyna and R_{el}/F_{max}=0.41. When the standard resistance and load curves are applied, the curve for $k_3 = 0.1k_1$ overestimates the maximum deformation, while the curve for $k_3 = 0.2k_1$ is close to the maximum drop test deformation. Based on the standard tri-linearisation of the FEA resistance curve in figure 5.1, the maximum response was expected to be underestimated by $k_3 = 0.2k_1$.

When the resistance curve is modified according to figure 5.7, the value of the maximum predicted response from the Biggs charts is the middle the curves for $k_3 = 0.2k_1$ and $k_3 = 0.2k_1$. The maximum response is underestimated when the modified load curve is applied. When both the modified resistance curve and the modified load curve are applied, the predicted maximum response is only 5 mm lower than the maximum deformation from LS-Dyna.

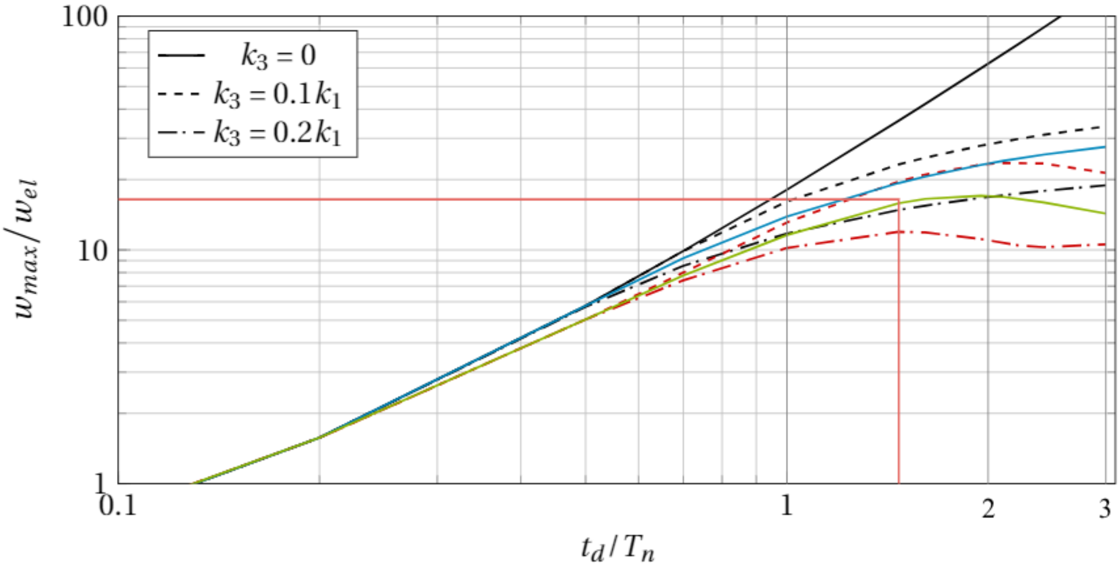

Figure 5.9: Biggs curves from Fortran for the dynamic response of a SDOF system equivalent to the drop test of a stiffened plate with 0 ° impact angle. FEA resistance curve is applied

Figure 5.10 shows the Biggs chart for a SDOF system corresponding to the drop test of the stiffened panel with 3 ° deadrise angle. The resistance curve applied in the Biggs chart in figure 5.10 is found from the FE analysis in LS-Dyna and R_{el}/F_{max}=0.51. The standard resistance curves give similar deviations from the actual deformation as for the drop test with zero impact angle. The response is overestimated with $k_3 = 0.1k_1$, but only slightly underestimated by $k_3 = 0.2k_1$. When the modified resistance curve is applied, the Biggs response curve is in the middle between the two former standard curves. However, for the plate with 3° impact angle, the difference between the modified and standard load curve is small. The Biggs curve with the modified load history predicts a small increase in the maximum deformation. At $t_d/T = 2.11$ for the system, the difference between the modified load curve and the triangular load curve is negligible. The response curve with both modified load history and modified response curve predicts a maximum response of 164 mm, which is 28.2 mm larger than the actual deformation measured in the drop test.

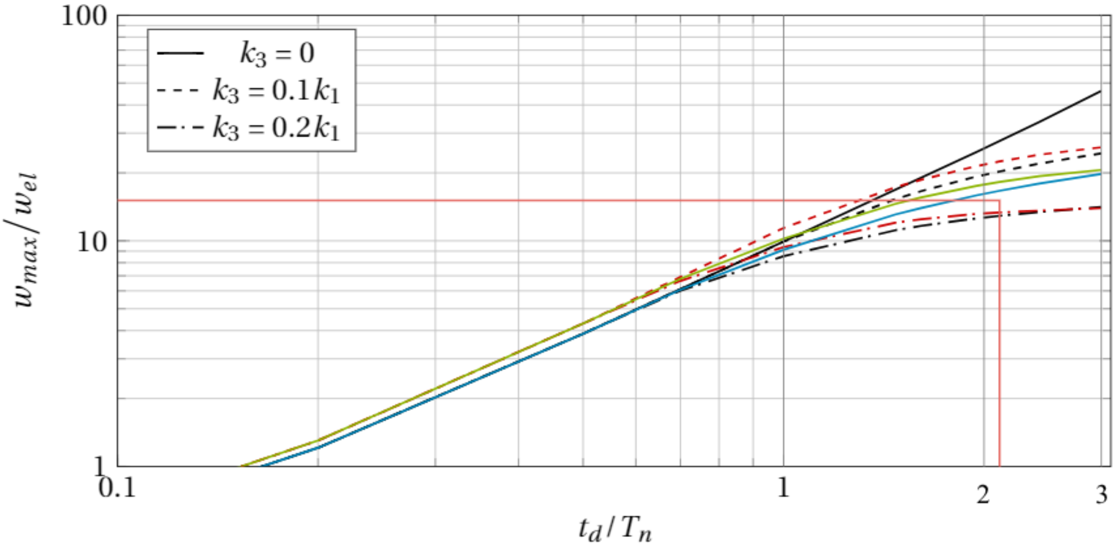

Figure 5.10: Biggs curves from Fortran for the dynamic response of a SDOF system equivalent to the drop test of a stiffened plate with 3 ° impact angle. FEA resistance curve is applied

Figure 5.11 shows the Biggs chart for a SDOF system representing the drop test of the stiffened panel with 0 ° deadrise angle. The resistance curve applied in the Biggs chart in figure 5.11 is found from the analytical approach in Amdahl et al. (2017) and R_{el}/F_{max}=0.394. The Biggs curve with the modified resistance curve overestimates the maximum response, while the Biggs curve with the modified load curve underestimates the maximum response. When both the resistance curve and the load curve are modified, the predicted maximum response only deviates from the actual maximum response with 6.8 mm.

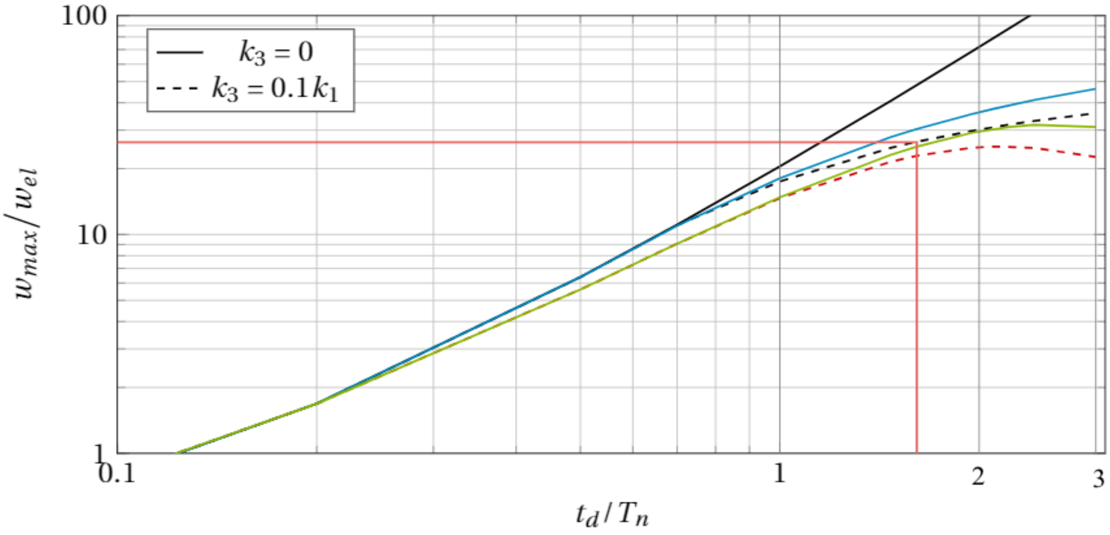

Figure 5.11: Biggs curves from Fortran for the dynamic response of a SDOF system equivalent to the drop test of a stiffened plate with 0 ° impact angle. Analytical resistance curve is applied

The maximum response estimated from the Biggs curves with modified pressure history and modified resistance curves are summarised in table 5.10.

Table 5.10: Summary of predicted maximum responses for the SDOF system with modified load curve and resistance curve in Biggs charts

	Predicted maximum reponse w_{max} [mm]	Drop test maximum response w_{max} [mm]	Difference [mm]
0° impact angle with resistance curve from LS-Dyna	142.5	148	5.5
3° impact angle with resistance curve from LS-Dyna	164.2	136	28.3
0° impact angle with analytical resistance curve	141.2	148	6.8

5.9 Discussion of Results

The maximum responses obtained from the Biggs design charts provided good approximations of the response from the drop tests in LS-Dyna. For design purposes, it is important that the simplified methods do not underestimate the maximum deformations. None of the results underestimated the deflection, although, for the flat impact, the deviation between predicted and actual deformation was minimal. The estimated maximum lateral deflection for the drop test with 0° deadrise angle only differed from the numerical results by 4.15% on average. For the drop test with 3° deadrise angle, the lateral deflection was overestimated by 17.4 %.

When the standard FEA resistance curves were applied, it was expected from figure 5.1 that $k_3 = 0.1k_1$ would overestimate, and that $k_3 = 0.2k_1$ would underestimate the lateral deflection. However, the curve with $k_3 = 0.2k_1$ did not underestimate the response in the Biggs charts.

Although the analytical resistance curve underestimated the capacity compared to the FEA resistance curve in figure 5.7, the maximum response from the design charts is only overestimated by 1.3 mm. The predicted response based on the analytical resistance curve was expected to be larger, since the analytical resistance curve underestimated the capacity of the plate in section 4.

It is challenging to quantify the effect the modifications of the pressure load will have on the response. For the flat impact, the adjusted load pulse underestimates the deformation. For the inclined impact, the modified load pulse is almost identical to the triangular approximation and hence the difference between the modified and standard Biggs curve is small. But despite the good fit between the load pulses, the inclined plate has the biggest deviation between the drop test deformation and the estimated response from the Biggs charts.

The maximum response from the Biggs charts depends on several inputs which all have some uncertain aspects. In addition to the approximated resistance curves and load histories, the duration of impact t_d, the eigen period T_n and equivalent load amplitude F_{max} will also affect the results. The value of t_d is chosen approximately so that $\mathrm{I}(t_d) \approx I(t_d + \Delta t)$. The wet elastic eigen period T_n includes the estimated value of the added mass, which is also an approximated value. Despite these uncertainties, the combination of the modified resistance curve and the modified load curve provides a maximum lateral displacement that is close to the maximum displacement in LS-Dyna. The standard curves in RP C204 (DNVGL, 2016a) yield inaccurate results for systems with resistance curves that do not fit the standard tri-linearisation or with pressure histories that do not fit a triangular shape. In conclusion, the Biggs design curves provide good results if they are plotted numerically with modified input.

Chapter 6

Studies of the Effect of Hydroelasticity and Limit State Conditions

In this chapter, further studies on fluid-structure impacts with a stiffened plate are conducted in LS-Dyna. The details of the numerical simulation are identical to the drop tests in chapter 3 and 4, with the exception of the boundary conditions and material behaviour. The effect of hydroelasticity is studied for drop test impacts with different deadrise angles and impact velocities. State of the art theoretical and experimental research on slamming impacts have focused on the *elastic* structural response for ULS conditions. Because the hydro-elastic structure interaction is well considered for ULS, it is of interest to investigate how well the elastic pressure history can predict the elasto-plastic deformations for ALS conditions.

6.1 Finite Element Model

The structural dimensions and element discretisation are identical to the stiffened plate described in chapter 4, but the boundary conditions have been reevaluated. If large lateral loads cause the stiffeners to buckle symmetrically with respect to the frame, clamped boundary conditions could be justified according to Amdahl (2005). By assuming that the wave loads hit the surrounding structure as well, a zero deformation angle to the girders and stiffeners may be reasonable. Thus, the stiffened plate is fixed against inwards rotation in the longitudinal direction, and fixed against rotations around both x and y-axis in the transverse direction. Although the plate boundaries are not restricted against in-plane displacements, some translational stiffness is added to the structure due to the elastic boundary and the translational restriction in z-direction caused by the imposed impact velocity. In a real structure, the adjacent structures will cause translational restrictions that will induce membrane effects which will increase the load-carrying capacity of the plate.

The material of the stiffened plate is steel S355. The response behaviour of the plate is varied between elastic, rigid and elasto-plastic with and without strain rate hardening. The linear material parameters for steel are given in table 6.1. The elasto-plastic material has the same nonlinear material properties as material 4 in table 3.4 from chapter 3. The strain rate parameters are taken as $C = 4000$ and $p = 5$ according to section 2.5.3.

Table 6.1: Linear material properties for the dropped panel

Material type	Material model in LS-Dyna	$\rho [kg/m^3]$	E [GPa]	ν [-]	σ_0 [MPa]
Elastic	Elastic	7850	210	0.3	355
Elasto-plastic	Piecewise linear plasticity	7850	210	0.3	355
Rigid	Rigid	7850	210	0.3	355

The impact velocity is 11.19 m/s, and the impact angle is 0 °. When the effect of hydroelasticity and limit states are considered, the velocity and angle will be varied.

6.2 Pressure Development

Figure 6.1 shows the pressure variation on the stiffened plate from the drop test with zero deadrise angle and 11.19 m/s impact velocity. The rigid peak pressure is 4 MPa. The elastic and elasto-plastic materials have the same distinct peak pressure at 2.4 MPa, which is almost half the value of the rigid peak value. The pressure impulse for the rigid plate is 9.8 kPas, for the elastic plate, the impulse is 12.7 kPas, and for the elasto-plastic materials, the impulse is approximately 10.5 kPas. The duration of the rigid load pulse is 5.5 ms, which is less than a third of the duration of the elasto-plastic impulses at t_d=22 ms. The duration of the elastic load pulse is 18 ms.

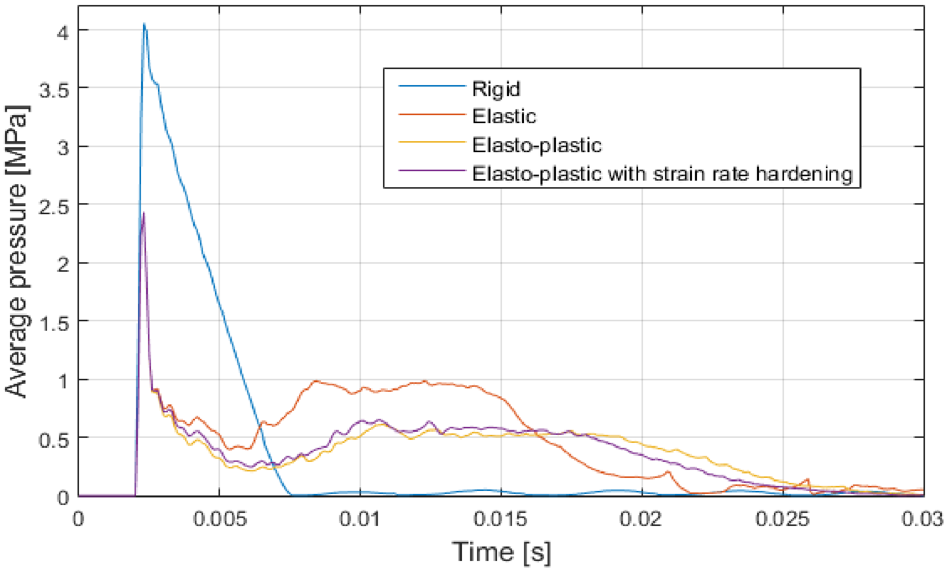

Figure 6.1: Pressure variation on the stiffened steel plate with $\beta = 0°$ and V = 11.19 m/s for different material response behaviour

The values of the wet eigen periods were obtained from plots of the upper strain in x-directions. The elastic eigen period is 16 ms, and the elasto-plastic is 11 ms. For the elasto-plastic plate, the strains did not oscillate as evidently as for the elastic plate. The relationship between the duration of impact and the wet eigen period for the elasto-plastic plate is $t_d/T_n = 2$, which categorises the elasto-plastic impact in the dynamic domain. For the elastic plate t_d/T_n=1.13, which also categorises the elastic impact in the dynamic domain, although the impact is slightly more impulsive.

6.3 Drop Test Responses

6.3.1 Response with Hydroelastic Behaviour

The maximum lateral deflections have been plotted in figure 6.2. For the elastic plate, the maximum response is 93 mm, for the elasto-plastic plate, the response is 170.5 mm, and for the elasto-plastic plate with strain rate hardening, the maximum response is 152.4 mm. The plots show that the elasto-plastic plates have large permanent deformations, while the response for the elastic plate is not permanent and oscillates around zero. When strain rates effects are included, the response decreases. This agrees well with the observed increase in deformation resistance in LS-Dyna as a consequence of the increased plastic flow stress in the material.

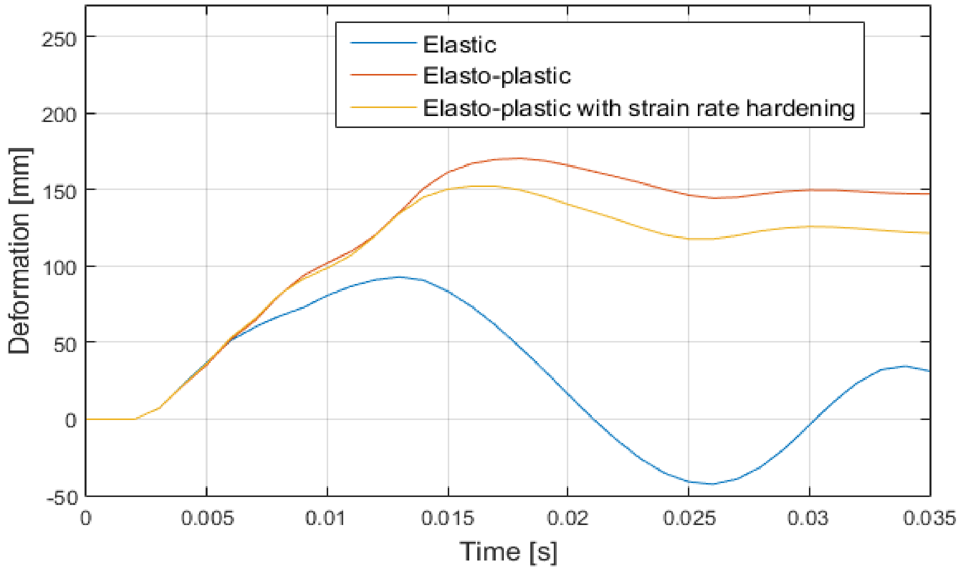

Figure 6.2: Maximum deflection for drop test of for stiffened plates with $\beta = 0°$ and V = 11.19 m/s

Contrary to the drop test in chapter 4, the transverse boundaries are not restricted towards in-plane motion, and the longitudinal boundaries are fixed against inwards rotations. The changes in the boundary conditions increased the maximum response with 22.5 mm. Because the stiffened plate in this chapter has a smaller stiffness, thus allowing a larger deformation, it would be expected that the eigen period would increase. However, no significant increase in the eigen period was observed from the results.

6.3.2 Response from Rigid Pressure Impulse

In order to study the effect of hydroelasticity, the pressure impulse from the rigid drop test is applied to an identical stiffened plate. The rigid pressure variation will not be affected by the deformation of the plate. By applying the rigid pressure variation to the elasto-plastic plate, the deformation without hydroelastic effect can be found. The added mass effects are accounted for by increasing the density of the comparable plate to ρ_a. The maximum deflection of the stiffened plate subjected to the rigid load pulse is shown in figure 6.3. The maximum elastic deformation is 183 mm in the direction of the motion of the plate. During the elastic drop test, the maximum elastic response occurred in the opposite direction of motion during the first response period. For the elasto-plastic plate subjected to the rigid load pulse, the maximum deformation has also increased compared to the drop test results in figure 6.2. The maximum deformation in the elasto-plastic plate is 281.1 mm, and when strain rate effects are included, the response is 247.6 mm. When the rigid load pulse is applied to the plates, the structural responses occur approximately 3 ms earlier than in the drop tests.

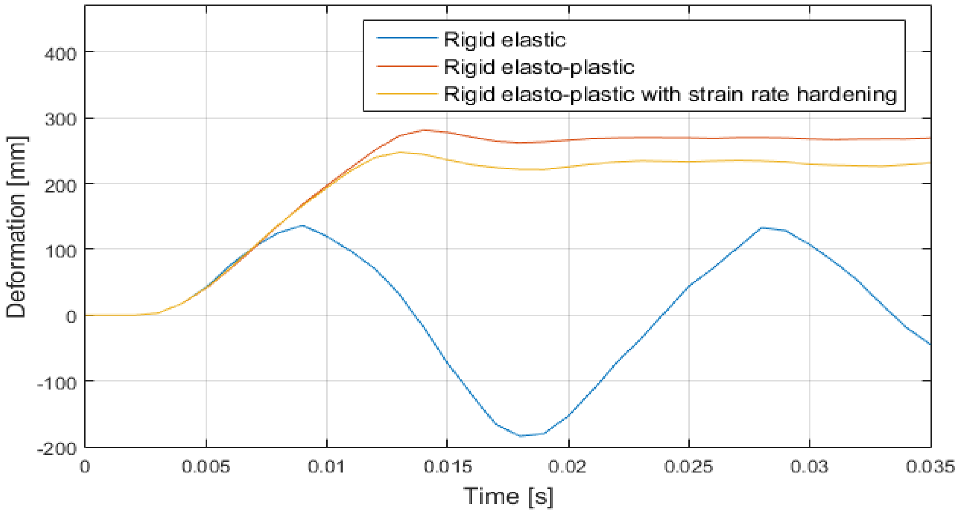

Figure 6.3: Structural response of stiffened panel with material density ρ_a subjected to a rigid load pulse

6.3.3 Elasto-plastic Response from Elastic Pressure Impulse

The elastic pressure variation from the drop test was applied to an equivalent elasto-plastic stiffened plate with an increased material density ρ_a accounting for added mass effects. The previous elasto-plastic response from the drop test was 170.5 mm. When the elasto-plastic plate was subjected to the elastic pressure pulse, the maximum response increased to 255.5 mm.

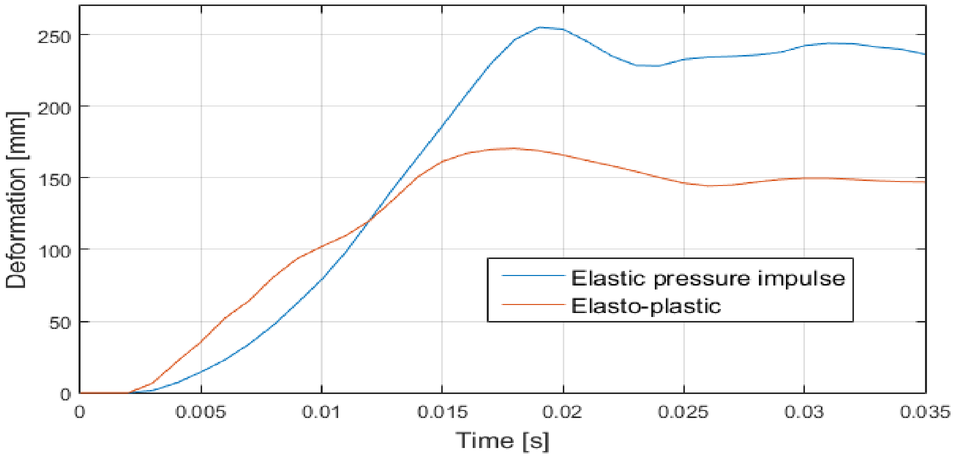

Figure 6.4: Elasto-plastic response of stiffened panel with ρ_a subjected to an elastic load pulse

6.4 Parameter Study on the Effect of Hydroelasticity

Faltinsen (1999) studied the effect of hydroelasticity on the elastic response for impacts with various deadrise angles and impact velocities. The role of hydroelasticity was also studied by Bereznitski (2001) for different deadrise angles and structural stiffness. Figure 6.3 shows that by applying the rigid pressure pulse, i.e. by neglecting hydroelasticity, the structural response is overestimated. A parameter study with different impact angles and velocities was performed to investigate how the severity of the slamming impact will affect the hydroelasticity. Nine test combinations with β=0, 3 and 7 degrees and V=7.5, 11.19 and 15 m/s were used for rigid drop tests in LS-Dyna. The rigid load histories were reapplied to a comparable elasto-plastic plate in order to obtain the elasto-plastic response without hydroelastic effects. Strain rate effects for the elasto-plastic material was neglected. The drop test responses in the middle of the elasto-plastic plate for the different tests conditions are plotted as a surface plot in figure 6.5. The maximum deformation increases for decreasing impact angle and increasing impact velocity.

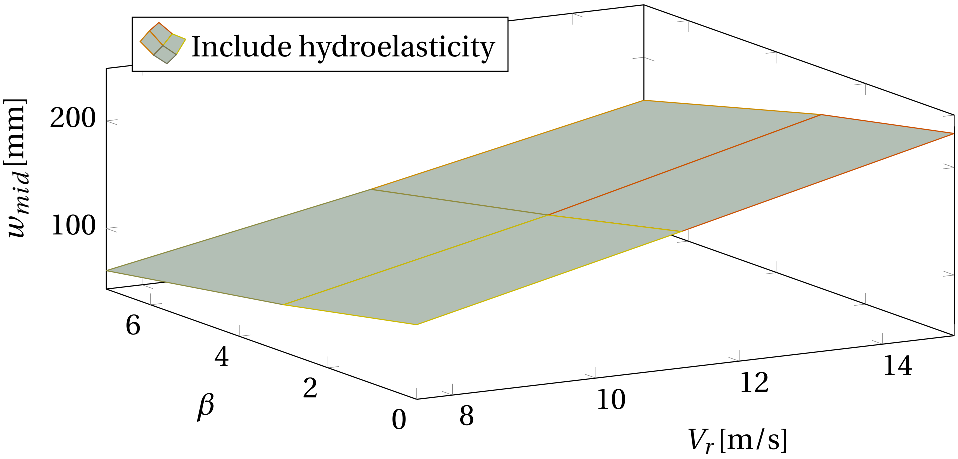

Figure 6.5: Mid-plate deformations from drop test with the elasto-plastic stiffened plate with various impact conditions

Figure 6.6 shows two surface plots of the mid-plate elasto-plastic response with and without the effect of hydroelasticity. The relative differences between the plastic deformations with or without hydroelastic effects have been calculated in table 6.2.

Table 6.2: Relative difference [%] between the responses with and without hydroelastic effects

	0 °	3 °	7 °
7.5 m/s	52.2	110	38.8
11.19 m/s	64.8	152.9	81.9
15 m/s	62.2	97.6	116.8

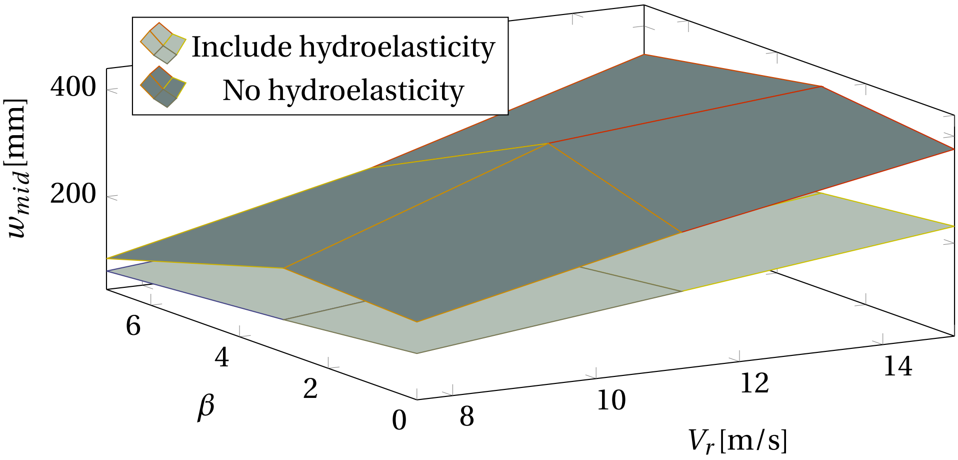

Figure 6.6: Surface plots of the mid-plate elasto-plastic deformation with and without hydroelastic effects for different deadrise angles and impact velocities

When hydroelastic effects have been neglected, the estimation of the structural response is overestimated. According to table 6.2, the largest relative difference in response occurs for the impact with 3° impact angle and 11.19 m/s impact velocity. The deviations between the hydroelastic and non-hydroelastic responses do not show a consistent increase for increasing severity of the slamming impact. The inconsistency differs from the results in Faltinsen (1999) and Bereznitski (2001) whose research showed that the effect of hydroelastic effects increased with decreasing impact angle and increasing impact velocity.

6.5 Parameter Study for ULS Prediction of ALS response

The same nine impact conditions were applied for elastic drop test simulations in LS-Dyna. The elastic pressure histories were reapplied to the elasto-plastic plates with ρ_a.

Figure 6.7 shows the surface plots of the mid-plate deformation from the elasto-plastic drop test, and for the elasto-plastic plate subjected to an elastic load pulse. The relative difference between the plastic response due to the elastic or elasto-plastic pressure variation has been calculated in table 6.3.

Table 6.3: Relative difference [%] between elasto-plastic responses due to a elastic or elasto-plastic pressure pulse

	0 °	3 °	7 °
7.5 m/s	41.6	44.9	58.4
11.19 m/s	31.9	69.1	82.1
15 m/s	30.1	82.1	97.5

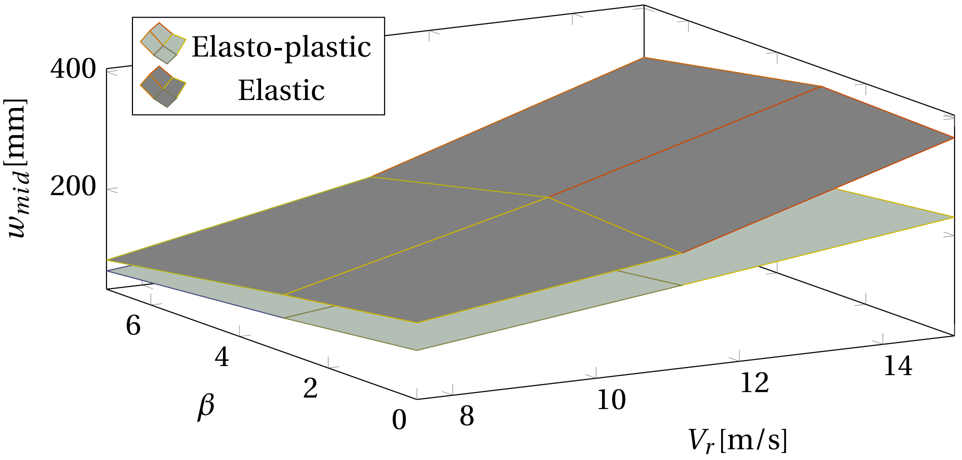

Figure 6.7: The effect of impact angle and velocity for the prediction of ALS elasto-plastic response with ULS elastic load history

When the elastic pressure variation is applied to the elasto-plastic plate, the prediction of the plastic deformations are conservative, although less conservative than the plastic deformations estimated by the rigid load variation. In general, the ALS response induced by the ULS pressure approaches the elasto-plastic response from the drop tests for decreasing impact velocities and increasing impact angles.

6.6 Discussion of Results

The parameter study has shown that if hydroelastic effects are not accounted for during the fluid-structure impact, the response will be overestimated. However, a clear correlation between the importance of hydroelastic effects as a function of impact angle and velocity was not obtained. It is challenging to draw any definite conclusions based on a small test sample which also contained some unexpected responses. To properly study the effect of hydroelasticity in relation to impact angle and velocity, a more comprehensive parametric study must be conducted.

When the elastic pressure variation was applied to the elasto-plastic plate, the structural response was underestimated. However, the predicted responses from the elastic impulse are less conservative and have a smaller scatter than the deformations causes by the rigid pressure impulse.

The variations in the results could be explained by how the pressure impulses have been applied to the plate. For the flat plate, the rigid and elastic pressure impulses were averaged across the plate surface and then reapplied to the same surface of the elasto-plastic plate. For the inclined plates, the spatial and temporal variations of the pressure were larger, and thus, the pressure was averaged across six sections. Ideally, the pressure variation on each element should have been exactly reapplied to the comparable model, but this was considered to be too time-consuming since all the pressure curves had to be re-applied manually in LS-Dyna. The pressure-time curves have not been applied quasi-statically, but at the same time scale as the drop tests. The approximation of the added mass also introduces uncertainty to the results.

Chapter 7

Experimental Drop Tests of Unstiffened Plates

Experimental drop tests of unstiffened plates have been carried out in cooperation with Sintef Ocean in the Ocean Basin Laboratory at NTNU. The drop tests are a part of the SLADE (2018)-project for slamming loads in structural design initiated by Sintef Ocean. The aim of the drop tests is to study the nonlinear plastic structural deformations induced by the slamming impact. The model tests represent a full-scale 3x3 m^2 steel panel subjected to slamming loads with a 100 years return period. The slamming impact from the breaking waves have been simplified to a drop test where the structure with the stiffened plate falls through the air and penetrates a calm surface. At model scale, the stiffened steel plate has been idealised to an unstiffened aluminium plate embedded in a rigid structure.

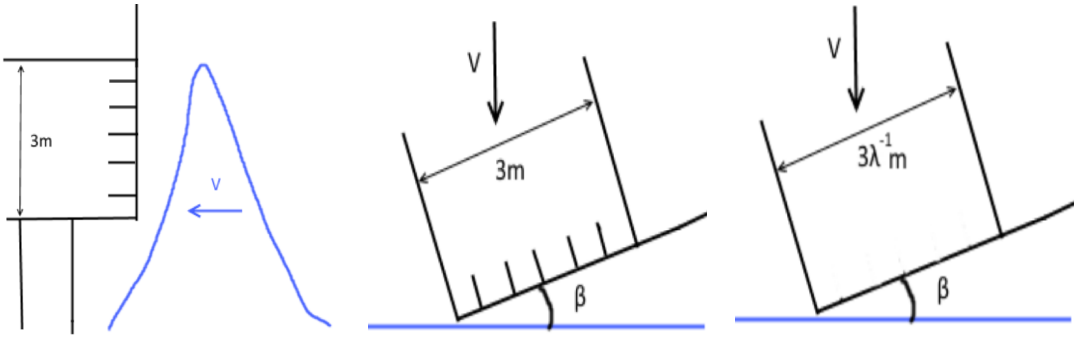

(a) Breaking wave impact on stiffened plate structure on platform deck

(b) Drop test representing breaking wave impact

(c) Model scale drop test

Figure 7.1: Idealisation of a slamming load impact against the column of a semi-submersible to a drop test where the structure falls and impacts the calm water surface

7.1 Background

The slamming phenomenon is a highly nonlinear problem with a complex coupling between fluid flow and structural response. A structural component that is exposed to violent slamming waves may undergo severe local plastic deformations. When using theoretical, numerical and experimental methods to study slamming loads, it is required to introduce simplifications and idealisations of the impact event.

Experiments and model tests are among the most valuable tools for understanding the physical effects of the slamming phenomena. Experimental data is crucial for validation of numerical tools and theoretical methods. However, model tests for slamming load impacts are still in need of improvement. There is very little experimental research on slamming tests with elasto-plastic deformations. The main focus in previous experimental studies has primarily been directed towards identification of pressures, global forces and strains for elastic or rigid panels. There are also little data on the structural dynamic response *during* the slamming impact. To fully understand the deformation mechanism, the instantaneous response during the impact should be captured.

7.2 Objective

The purpose of the experimental study is to perform drop tests causing large plastic deformations in the aluminium plate. The experimental data from the drop tests will be used to validate an explicit, coupled FSI simulation of the drop impact scenario in LS-Dyna. The instantaneous deformation of the plate is calibrated with high-speed DIC cameras normally used in solid impact mechanics. In this thesis, emphasis has been put on numerical simulations of the impacts and comparisons with the structural response of the plate. The pressure histories and stress variations in the plates have not been included. Only elasto-plastic material behaviour is studied in this thesis, but the SLADE-project will also include drop test experiments with rigid and elastic plates in future work.

7.3 Scaling of the Experimental Model

Stiffened steel plates in offshore structures typically have a plate area of 3x3 m^2. Figure 7.2 illustrates two realistic examples of stiffened steel plates covering the hull and topside of an offshore structure.

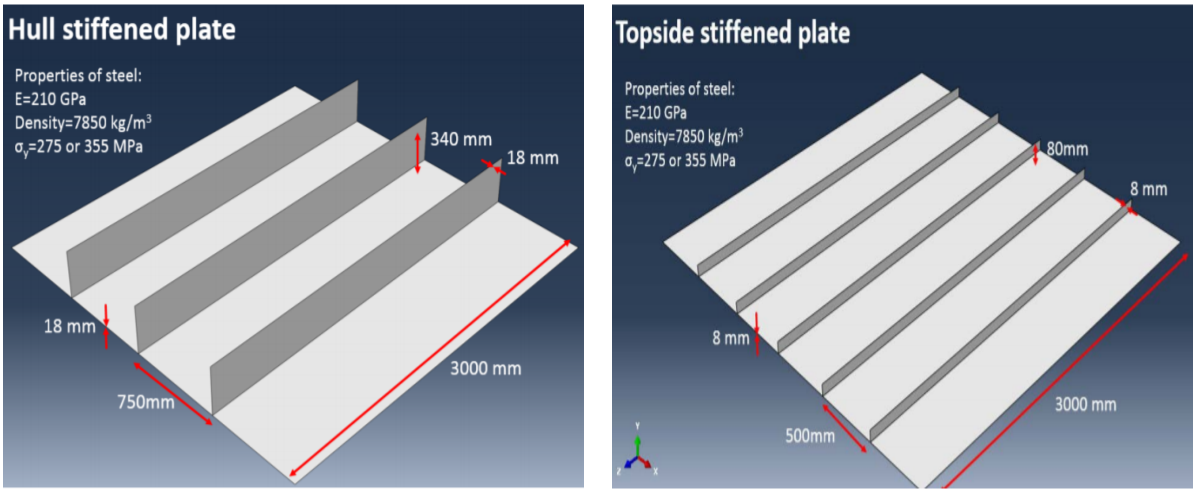
Hull stiffened plate
Properties of steel:
E=210 GPa
Density=7850 kg/m³
σy=275 or 355 MPa
340 mm
18 mm
18 mm
3000 mm
750mm
Topside stiffened plate
Properties of steel:
E=210 GPa
Density=7850 kg/m³
σy=275 or 355 MPa
80mm
8 mm
8 mm
500mm
3000 mm

(a) Stiffened steel panel with dimensions relevant for a panel in a column of a semi-submersible

(b) Stiffened steel panel with dimensions relevant for a vertical wall above deck

Figure 7.2: Examples of stiffened plates covering the hull and topside of offshore structures from SLADE (2018)

In the SLADE-project, the dimensions of a hull stiffened panel have been chosen for the full-scale model. The steel type for the full-scale model is assumed to be steel S355, which is a commom material for offshore structures. The full-scale plate thickness is 18 mm. Thus, the stress-strain curve defined in RP C208 (DNVGL, 2013) for S355 with thickness 16 mm < t < 40 mm will describe the material behaviour. The true stress- true strain curve is shown in figure C.2. The drop test impact should experience slamming forces comparable to the wave loads that may be encountered in a 100 years storm. A reasonable critical velocity of the wave crests in a 100 year storm is approximately 15 m/s according to SLADE (2018).

The drop tests will be performed with existing equipment and set-up from a previous drop test experiment by Lian et al. (2015) in OMAE. The scaling of the model test is therefore limited by the availiable equipment and basin. Based on the existing equipment, a suitable scaling could be approximately 1:15. At this scale, properties for both the elastic and plastic deformation of the plate cannot be correctly scaled in the same model. In order to apply Froude scaling to the response, the model of the plate should be as realistic as possible. However, producing a model that is geometrically similar to the full-scale model at small model scales, is often challenging. In order to reduce the number of parameters that must be scaled correctly, the stiffeners have been neglected. The stiffened plate field is instead approximated as an equivalent unstiffened plate. The simplification reduces the parameters that need to be scaled to the material and plate thickness. Relevant Froude-scaled parameters for the slamming impact are summarised in table 7.1. The parameter r is the relationship between density of sea water and fresh water.

Table 7.1: Scaling parameters for panel drop test

Description	Symbol	Scale	Unit
Length	L	λ	mm
Drop height	H	λ	mm
Impact velocity	V	$\lambda^{1/2}$	m/s
Bending stiffness	EI	rλ	GPa m^3
Yield stress	σ_y	rλ	MPa
Membrane capacity	N	rλ^2	N/mm

In order to obtain an accurate representation of the elastic and plastic deformation history in model scale, the bending stiffness EI, plastic moment capacity M_p and membrane capacity N_p should be scaled correctly. The SLADE drop tests focus on the hydro-plastic response of the panels where large permanent deformations are expected. The edges of the unstiffened plate in the drop tests are fixed against rotations and in-plane translations. When the clamped plate undergoes large out-of-plane deformations, the load will mainly be supported through membrane forces. Thus, the model should be scaled so that the plastic response is well captured. The correct scaling of the plastic response is achieved by choosing a plate thickness and material that have the correctly scaled membrane capacity.

Equation 7.1 gives the relationship between membrane force in the model and full scale. N is the membrane force per unit width of the plate. The bar denotes full-scaled variables.

$$\frac{\overline{N}}{N} = \frac{\bar{\sigma}\bar{t}}{\sigma t} = r\lambda^2 \tag{7.1}$$

By solving equation 7.1 with respect to the scale factor λ, equation 7.2 is obtained.

$$\lambda = \sqrt{\frac{1}{r}\frac{\bar{\sigma}_{ts}\bar{t}}{\sigma_{ts}}} \tag{7.2}$$

If the same material is applied in the model and the full-scale, equation 7.1 shows that the plate thickness in the model will be very thin. Too thin plate thickness can be problematic during the assembly of the structure. Thicker plates can be used if a softer material for the model test is applied. The chosen material for the model test is aluminium A1050 H111. Unstiffened plates of Aluminium A1050 H111 with a plate thickness of t=0.6 mm was found available for production. A1050 H11 has an ultimate tensile strength σ_{ts}=72 MPa and E=72 GPa. The material for the full-scale plate is steel S355 with ultimate tensile strength of σ_{ts}=465 MPa and a plate thickness t = 18 mm.

In a uni-directional tensile test, the largest axial force will occur when the true stress is equal to the ultimate tensile strength. By inserting the plate thickness and ultimate tensile strength from the model and full-scale in equation 7.2, the scale factor λ = 13.92 is obtained. Zhang et al. (2014) tested the ability of the membrane scaling in equation 7.1 to represent the plastic response. For large strains, the membrane force from a uniaxial tensile test with A1050 O agreed well with the scaled membrane force from full-scale S355 steel. Because large strains are expected in the SLADE drop test, the scaling of the membrane capacity is considered to be a good method for modelling the plastic response. In table 7.2, some of the main properties of the drop test experiments have been scaled with λ = 13.92. The drop height is found from the scaled impact velocity based on energy equilibrium of the pendulum motion, $h = 0.5v^2/g$.

Table 7.2: Model and full scale parameters scaled according to correct membrane capacity N_p

Scaling factor λ=13.92	Model scale	Full scale
Plate thickness [mm]	0.6	18
Plate dimensions [m]	0.215	3
Impact velocity [m/s]	4.02	15
Drop height [m]	0.82	11.5
Material	Aluminium A1050 H111	Steel S355
E-modulus [GPa]	72	210
Ultimate tensile strength [MPa]	72	465

7.4 Experimental Set-up

The drop tests were performed in the "Trim-dokka"-basin in the Ocean Basin Laboratory at SINTEF Ocean. The basin is approximately 2.03 m wide, 10 m long and 1.15 m deep. The aluminium plate has an effective plate area of 22x22 cm^2. The aluminium plate is embedded in the rigid steel S355 box shown in figure 7.3a. The quadratic steel box with the fixed aluminium plate has a side length of 33 cm and a height of 5 cm. The rigid box is bolted to the bottom of the rigid impactor. The impactor is open on top and has a quadratic opening in the bottom, which allows visual monitoring of the structural response of the aluminium plate. The bottom of the impactor, i.e. the area that impacts the free surface, is 48.9 cm wide and 34.4 cm long. The total height of the impactor is 80 cm. At the top of the impactor, the width is 103.9 cm, and the length is 73.2 cm.

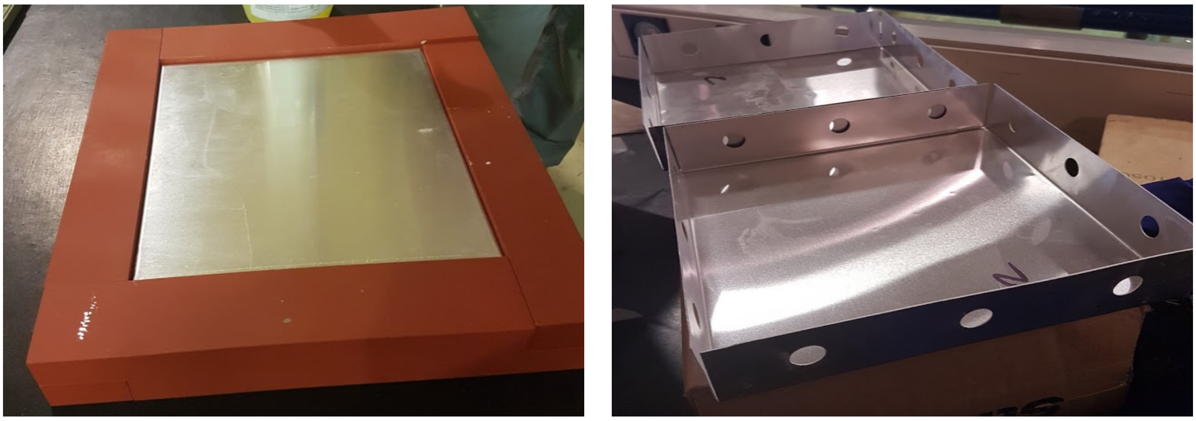

(a) Aluminium plate embedded in a rigid steel box. The visible surface will impact the fluid surface

(b) Samples of aluminium plates with bent edges. The bent edges are bolted to the inside of the rigid steel box

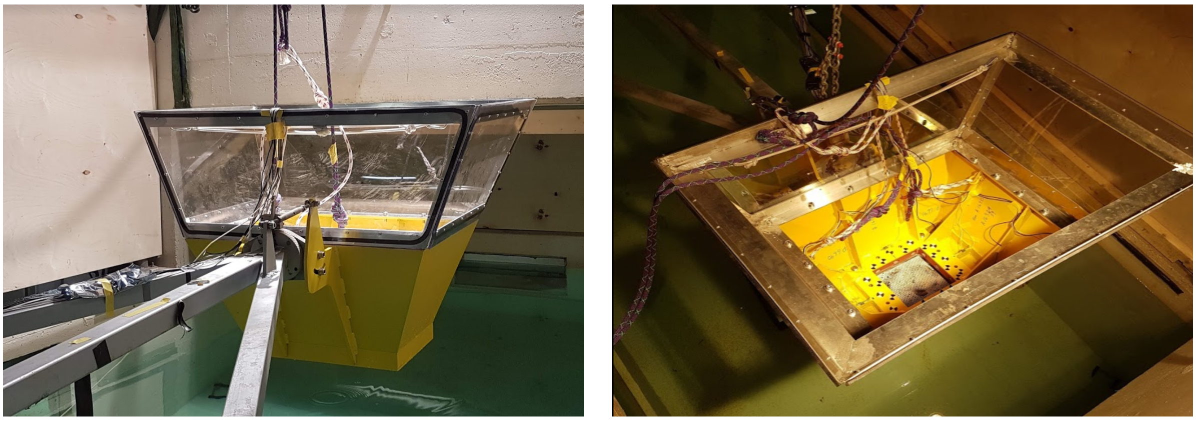

(c) Impactor connected to the arm

(d) Top view of impactor. The aluminium plate is visible in the quadratic square in the bottom

Figure 7.3: Pictures of impactor, rigid steel box and aluminium plate from the drop test

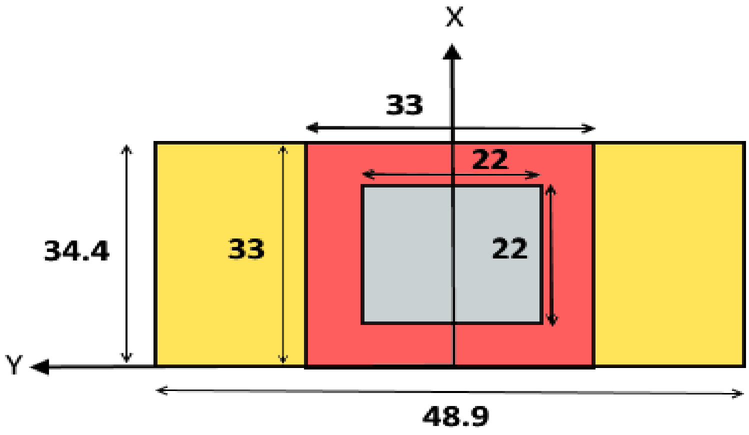

Figure 7.4: Dimensions [cm] of the rigid impactor, rigid steel box, and flexible aluminium plate

The impactor is connected to a 2.31 m long drop arm. The hinge that connects the impactor to the arm is 12.5 mm. Modifications of the impact angle between the impactor and the surface are adjusted at the hinge. The other ends of the drop arm are connected to hinges that allow rotation of the rig. The drop height is adjusted with a crane and a chain connected to the impactor. The total weight of the drop test rig is 139.42 kg. The deformable aluminium plate is embedded in a larger rigid structure in order to represent the surrounding walls of a semi-submersible. The mass of the rig should be large enough so that the rigid body accelerations during the penetration of the free surface are minimised.

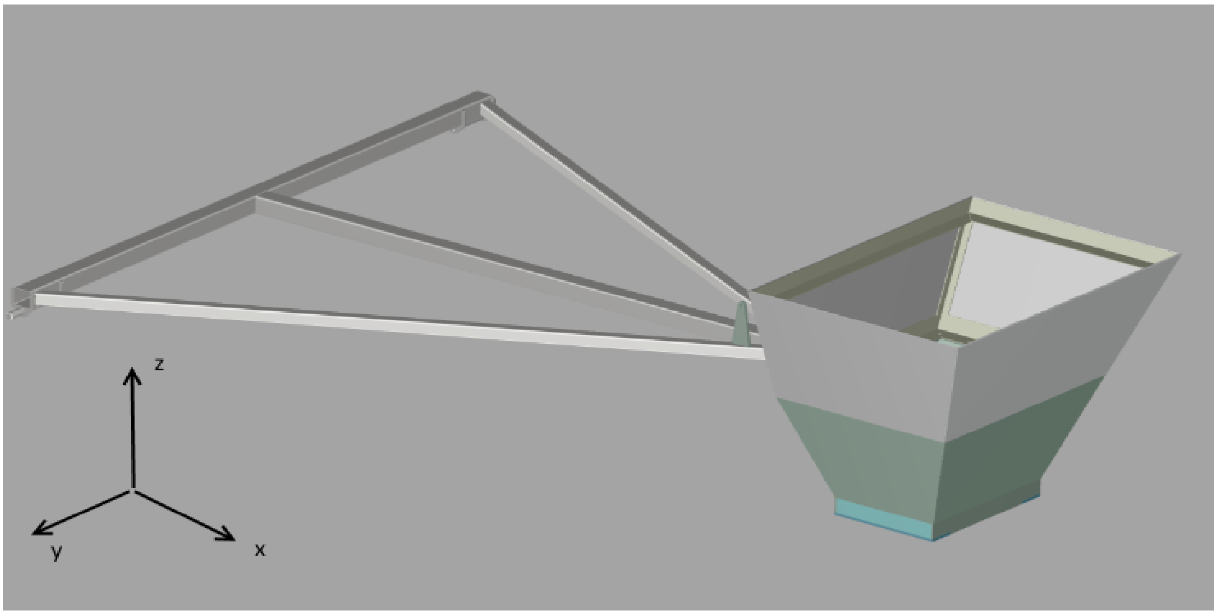

Figure 7.5: CAD-drawing of the drop test rig from SLADE (2018)

Before the drop test, the impactor is only supported by a chain with a pin connected the hinge between the impactor and the arm. In order to initiate the free fall of the impactor towards the fluid surface, the pin is released from the hinge by pulling a rope connected to the pin. The impactor falls towards the fluid surface with an impact angle β. The impactor follows the rotational motion of the arm, and will therefore have both a horizontal and vertical velocity component through the water. Ropes that hang loosely at the initial position of the impactor are used to decelerate the impactor before it hits the bottom of the basin.

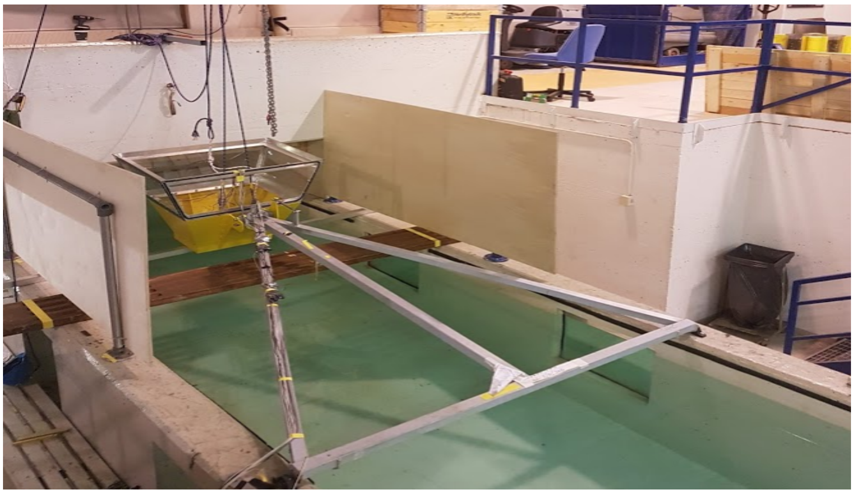

Figure 7.6: Installed drop test rig at the "Trim-dokka" basin

A 45 degrees inclined mirror is located at the bottom of the basin. A high-speed camera with 3000 frames per second photographs the impact through a window at the end of the basin. The camera captures the image of the bottom of the aluminium plate through the mirror. This is illustrated in figure 7.7 and 7.8a.

Digital Image Correlation, DIC, with high-speed cameras are applied to measure the deformation of the plate during the impact. The DIC cameras are mounted above the rig, looking down at the aluminium plate during the drop test impact. When two DIC cameras are applied for stereo vision, both in-plane and out-of-plane displacements of the plate can be measured. A speckle pattern has been sprayed on the surface of the aluminium plate facing the cameras. During the impact, the pattern changes due to the deformation of the plate. The change in the pattern is captured with the DIC cameras with 37000 frames per second. Based on the observed changes in the speckle pattern, the deformations of the plate can be estimated.

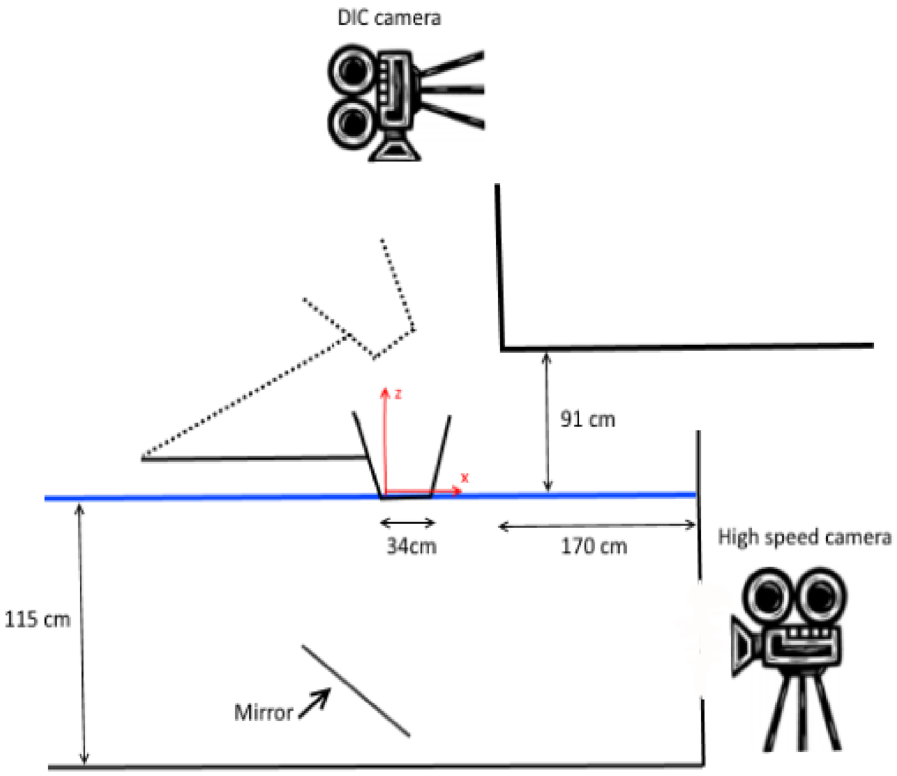
DIC camera
z
x
91 cm
34cm
170 cm
High speed camera
115 cm
Mirror

Figure 7.7: Illustration of the experimental set-up

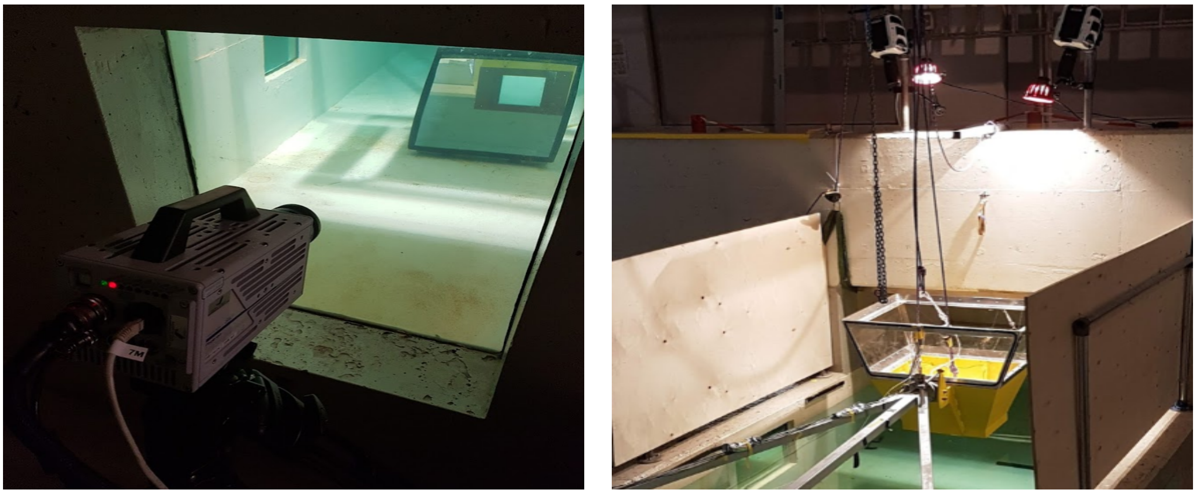

(a) High speed camera with 3000 Hz photographing the impact through the window of the basin

(b) Two DIC cameras with 37000 Hz mounted above the rig to monitor the lateral plate deformation

Figure 7.8: Installation of high-speed cameras for the drop test experiment

7.5 Test Conditions

The experiment was performed for 12 drop tests impacts. Most of the drop test impacts were performed with zero impact angle, but a 4° impact angle was also tested. The A1050 H111 plates were fabricated in two batches, denoted 1 and 2. The drop tests were only performed with material 2, but the difference between material 1 and 2 is expected to be negligible. The test details for the experimental impacts are given in table 7.3.

Table 7.3: Test specifications for the different drop impacts

Test number	Drop height [cm]	Angle [deg]	Material	DIC	Underwater HS camera
1	77.8	0	2	No	No
2	77.8	0	2	No	No
3	77.8	0	2	Yes	Yes
4	44.3	0	2	Yes	Yes
5	44.3	0	2	Yes	Yes
6	22.2	0	2	Yes	Failed
7	11.8	0	2	Yes	Yes
8	44.4	4	2	Yes	Yes
9	44.4	4	2	Yes	Yes
10	84.5	4	2	Yes	Yes
11	84.5	4	2	Yes	Yes
12	44.4	0	2	Yes	Yes

The first two drop tests were performed before the high-speed measuring equipment had been installed. For the rest of the drop tests, both cameras were applied. Reference pictures of the plate before and after the impact were taken with the DIC camera. When these pictures were taken, the bottom of the impactor was lowered to the water line.

For the flat impacts, the drop height was measured from the edge of the impactor that was closest to the surface at the start position, i.e. the edge closest to the hinge. When the plate falls with a 4° impact angle, the drop height was measured from the initial position of the edge that first hits the water. The impact angle is -4 ° according to the global coordinate system in figure 7.9(b).

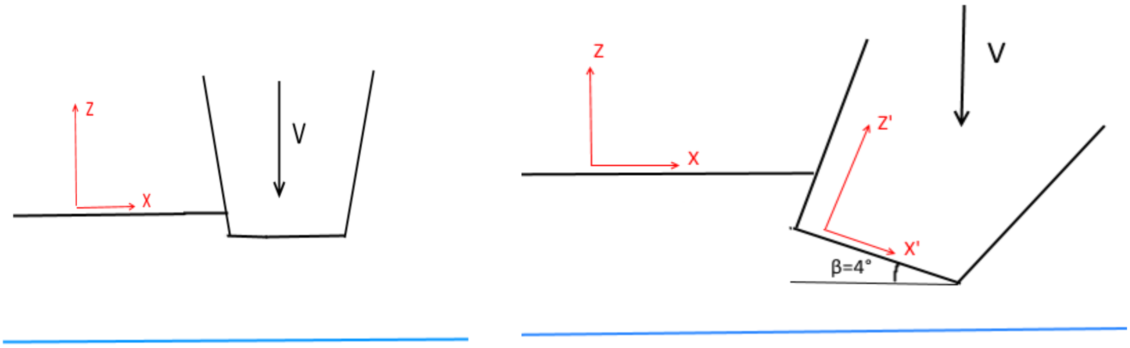

(a) Drop test impact with 0° deadrise angle **(b)** Drop test impact with -4° deadrise angle

Figure 7.9: Illustration of flat and inclined drop test impacts

After the drop test impact, the rigid steel box with the aluminium plates was demounted carefully from the impactor. The permanent plastic deformations were measured with the Mitutoyo measuring equipment and by a dial gauge instrument. The Mitutoyo machine is an automatic measuring instrument that measures the deformation of an object with a predefined pattern and frequency. The aluminium plate was mapped with a 15x15 measuring point pattern. Due to a strict schedule, the Mitutoyo machine was not applied for test 1, 5 or 11. A dial gauge was also applied to measure the maximum and mid-plate deformations manually. The purpose of the dial gauge was to verify the permanent deformations measured by Mitutoyo.

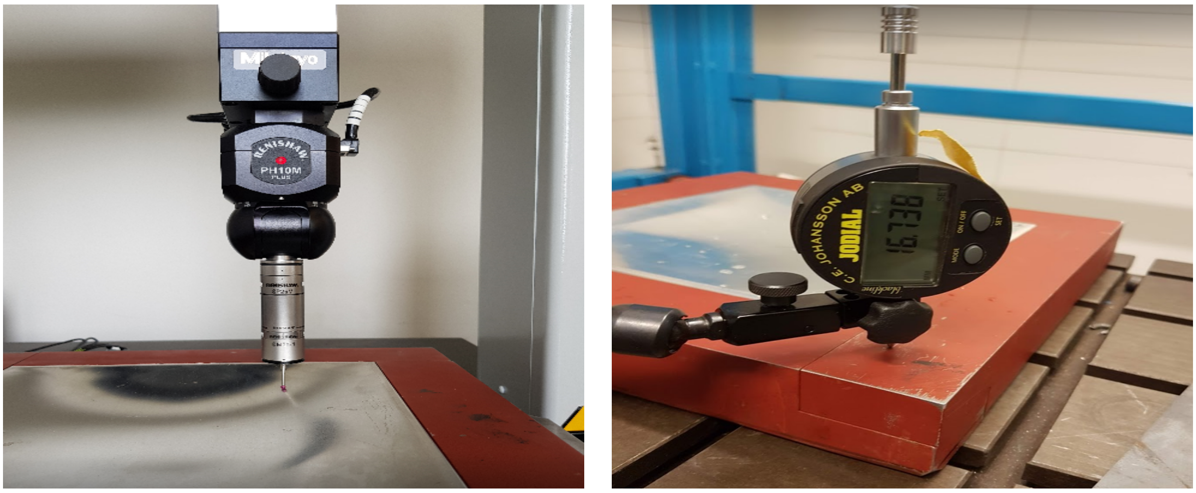

(a) Automatic: Mitutoyo measuring equipment **(b)** Manual: Dial gauge measuring equipment

Figure 7.10: Equipment applied to measure the permanent lateral plate deformations

7.6 Results from Drop Test Experiments

7.6.1 Deformations with 0° Impact Angle

Drop test impacts with 0° impact angle were performed from four different drop heights. From the Mitutoyo scans and visual interpretation, it was discovered that the maximum deformation occurred in the middle of the plate for all impacts. This is shown in the surface plot of the permanent deformation measured by Mitutoyo in figure 7.11(a). As expected, the maximum deformation increases for increasing drop height. The maximum deformations measured by the dial gauge and Mitutoyo are summarised in table 7.4. The dial gauge error is the displacement shown on the dial gauge when the measuring pin is moved from the rigid steel box to the maximum deformation and back to the opposite side of the steel box.

Table 7.4: Maximum permanent out-of-plane deformations measured with dial gauge and Mitutoyo measuring equipment for plate impacts with zero deadrise angle

Test	Drop height [cm]	Dial gauge Max deformation [mm]	Dial gauge Error [mm]	Mitutoyo Max defomation [mm]
1	77.8	21.38	0.031	*
2	77.8	21.52	0.117	21.59
3	77.8	*	*	21.37
4	44.3	*	*	16.62
5	44.3	16.77	0.034	*
6	22.2	12.9	0.031	12.91
7	11.8	9.96	0.027	10.01
12	44.4	16.82	0.069	16.8

*Not measured for these drop tests

Due to a tight time schedule, both of the measurement techniques were not performed for all of the tests. The deformations from the Mitutoyo machine are most accurate because the measurements are performed by a computer, while the dial gauge measurements are performed manually. For the tests measured by both machines, the results in table 7.4 show a negligible deviation between the two measuring techniques. The small deviation indicates that the dial gauge can be used as a sufficiently accurate estimation of the deformation for tests without the Mitutoyo scan. Three drop test impacts were performed at drop height 77.8 cm and 44.3 cm. The relative difference between the largest and smallest permanent deformation with identical impact conditions, was 0.9 % for 77.8 cm and 1.07% for 44.3 cm.

The small scatter in the results for the drop tests with equal impact conditions shows that the experiments are repetitive. In figure 7.11(b) the deformation profile along the middle of the plate in the direction of positive x-axis have been plotted for the flat impacts. The repetitiveness of the experiment is clearly shown for test 4 and 12 which have almost identical deformation profiles with the same drop test conditions.

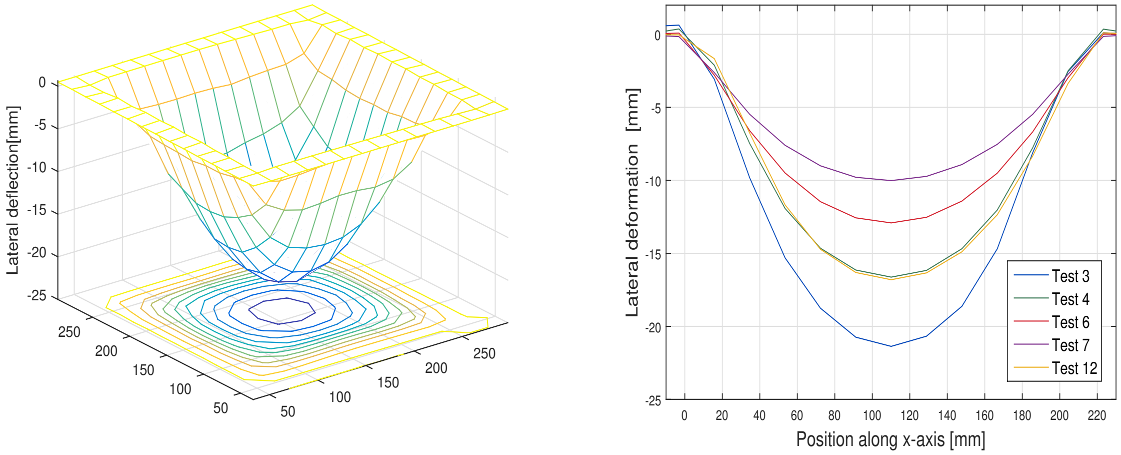

(a) Surface plot of test 3 from Mitutoyo

(b) Lateral deformation profiles along the middle of the plate in x-direction for drop tests with zero deadrise angle. The x-axis corresponds to the axis in figure 7.12(a)

Figure 7.11: Lateral plate displacement measured by Mitutoyo for drop tests with 0° impact angle

The permanent plastic deformations of the aluminium plate in test 2 is shown in figure 7.12(a). The coordinate system is drawn according to the global coordinate system shown in figure 7.7. The deformation patterns from Mitutoyo showed that the plate deforms in an approximately symmetric cosine shape. However, a small dent is observed at the left boundary in figure 7.12(a) and in the deformation profiles from Mitutoyo. The dent is located at the edge closest to the hinge between the impactor and the arm. The dent was present for most of the impacts, but was especially prominent for the drop tests with drop height 77.8 cm and zero impact angle.

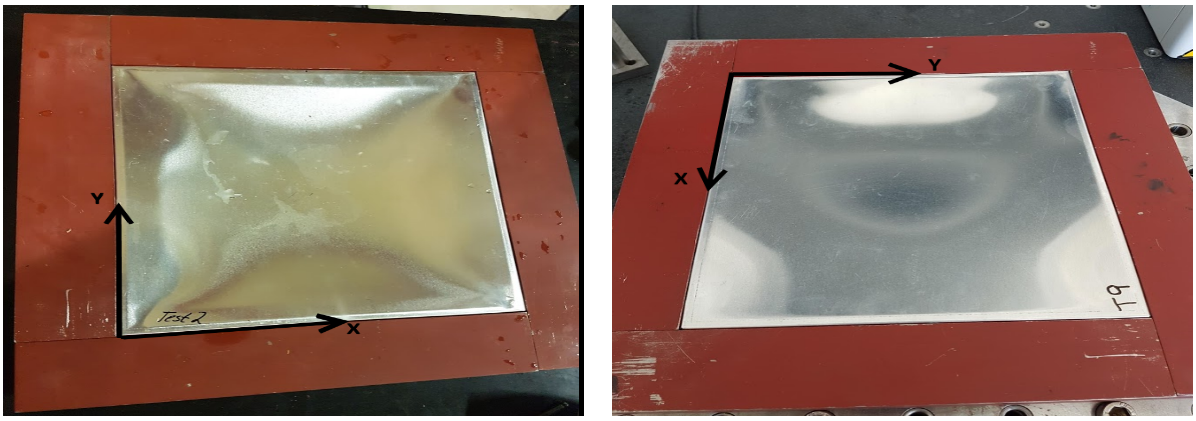

(a) Deformed aluminium plate from test 2 with zero impact angle and 77.8 cm drop height

(b) Deformed aluminium plate from test 9 with 4 degrees impact angle and 44.4 cm drop height

Figure 7.12: Deformed aluminium plates from drop test experiment

7.6.2 Deformations with 4 ° Impact Angle

Drop tests with a 4° impact angle were performed at two different drop heights. The impactor is inclined -4° with respect to the global coordinate system in figure 7.7. Contrary to the flat impact, the maximum deformation does not occur in the middle of the plate, but is slightly shifted towards the edge that is last submerged. In the y-direction, a symmetric cosine deformation pattern is obtained. The maximum deformations are summarised in table 7.5. For test 8, there is a 0.56 mm difference between the deformation predicted by dial gauge and the Mitutoyo. When the maximum deformation does not occur in the middle, it is more challenging to measure the maximum deformation accurately with manual measuring equipment. When the plates with 0° and 4° degrees impact angles were dropped from the same height, i.e. 44.4 cm, the maximum deformation in the inclined plates was on average 3.4 % larger than for the flat plates.

Table 7.5: Maximum permanent out-of-plane deformations with dial gauge and Mitutoyo measuring equipment for plate impacts with 4 ° deadrise angle

Test	Drop height [cm]	Dial gauge Max deformation [mm]	Dial gauge Error [mm]	Mitutoyo Max deformation [mm]
8	44.4	16.7	0.001	17.26
9	44.4	17.49	0.001	17.51
10	84.5	24.09	0.097	24.1
11	84.5	23.89	0.059	*

*Not measured for these drop tests

The deformation profiles and response plotted in figure 7.13 show the shifted maximum deformation that occurs when the plate is inclined. The repetitiveness of the drop tests is also emphasised by the good agreement between the permanent deformation profiles for test 8 and 9 from the same drop height in figure 7.13(b).

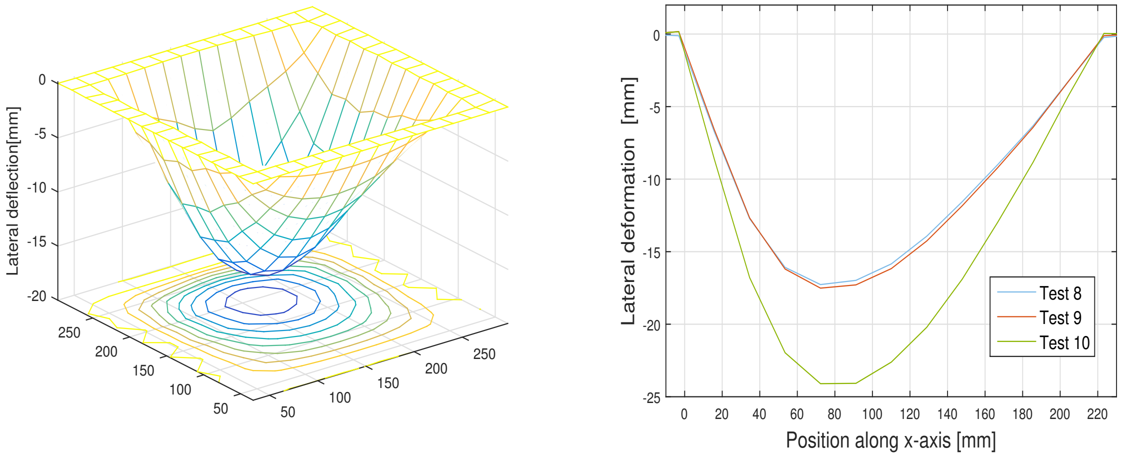

(a) Surface profile of test 9 from Mitutoyo

(b) Lateral deformation profiles along the middle of the plate in x-direction. The x-axis corresponds to the axis in figure 7.12(b)

Figure 7.13: Lateral plate displacement measured by Mitutoyo for drop tests with 4° impact angle

7.6.3 Results from DIC Measurements

SIMLAB NTNU performed the DIC measurements of the plate response and the post-processing of these results. The DIC cameras photograph at 37 000 Hz, hence, a large amount of data is generated from a single test. Figure 7.14 shows contour plots from DIC of the maximum out-of-plane deformations from test 3 with β=0°, and test 8 with $\beta = 4°$. The maximum deformation occurs in the middle of the plate for test 3, and the maximum deformation is shifted from the middle for test 8. The contour plots show the same pattern for maximum deformation as observed by the Mitutoyo measurements.

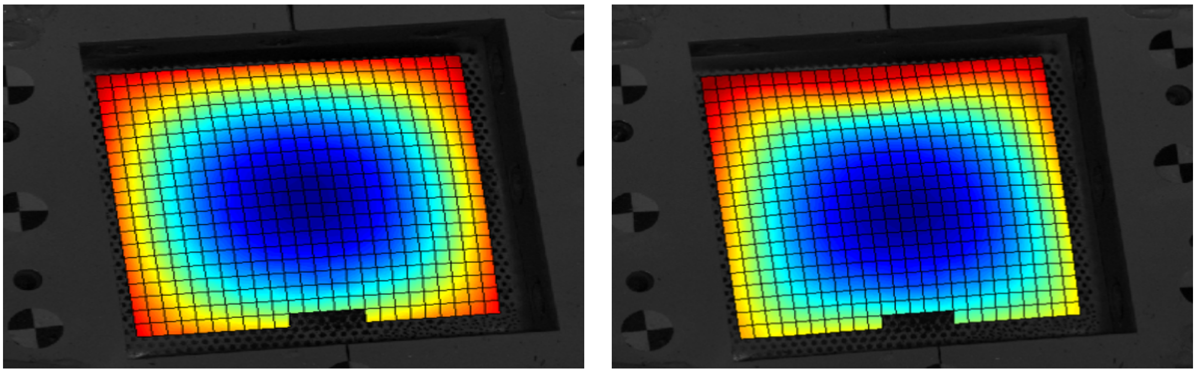

(a) Test 3 with zero impact angle

(b) Test 8 with 4° impact angle

Figure 7.14: Contour shapes of the out-of-plane deformations for the aluminium plates from DIC field measurements. The changes in the speckle pattern have beem calibrated to a finite element mesh

In table 7.6, the maximum and permanent deformations have been measured by DIC for each drop test. The deformations are taken as the average value of the four corner nodes of the element with the largest displacement. The permanent deformations have been calculated based on the difference in deformation between the photographs taken of the plate before and after the impact. There is no post-impact photograph of test 3, so this test does not have a valid estimation for the permanent deformations. The small deviations between the deformations measured by DIC and Mitutoyo indicate that the DIC measuring technique captures the response of the plate quite well.

Table 7.6: Maximum and permanent plastic deformations measured by DIC

Test	Max deformation [mm]	Permanent deformation [mm]	Deviation from permanent deformation with Mitutoyo [mm]
3	23.41	*	*
4	18.49	16.9	-0.33
5	19.1	16.81	0.03
6	14.77	12.55	0.3
7	10.82	9.32	0.48
8	18.12	16.99	-0.06
9	18.27	17.31	0.15
10	25.1	24.35	-0.29
11	25	24.14	-0.31
12	18.41	16.53	-0.29

*The duration of the DIC measurements were too short to capture the permanent plastic deformations

In figure 7.15, the permanent deformation profiles measured by Mitutoyo and DIC from test 12 and 8 are shown. The permanent deformation profiles almost coincide completely.

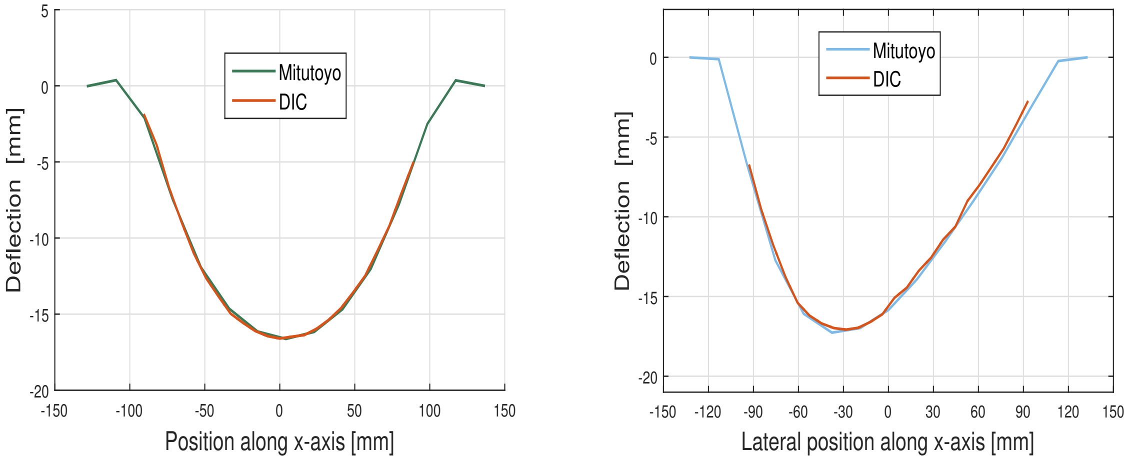

(a) Test 12 with $\beta = 0°$ and drop height 44.4 cm

(b) Test 8 with $\beta = 4°$ and drop height 44.4 cm

Figure 7.15: Deformation profiles from DIC and Mitutoyo

In figure 7.16 and 7.17, the DIC deformation of the node with largest deformation have been plotted for the drop tests. The DIC cameras measure z=0 at the position of the black and white circle stickers on top of the rigid steel box shown in figure 7.14. The distance from z=0 to the aluminium plate is approximately 57 mm. The z-coordinates of the nodes have been normalised with 57 mm so that the initial position of the aluminium plate is at z=0. The duration of the impact measured by DIC varied for the different drop tests. In figure 7.16 and 7.17, the time has been shifted for some of the tests so that the deformation could be compared more easily. The deformation curves show that the drop tests with identical impact conditions follow more or less the same deformation curves after the plate hits the water. The plates with zero impact angle have a larger difference between the permanent deformation and the maximum deformation than the plates with 4° impact angle. For the flat plates, the relative difference between permanent and maximum deformation is on average 7.8 %, while for the inclined plates the average relative difference is 1.3 %.

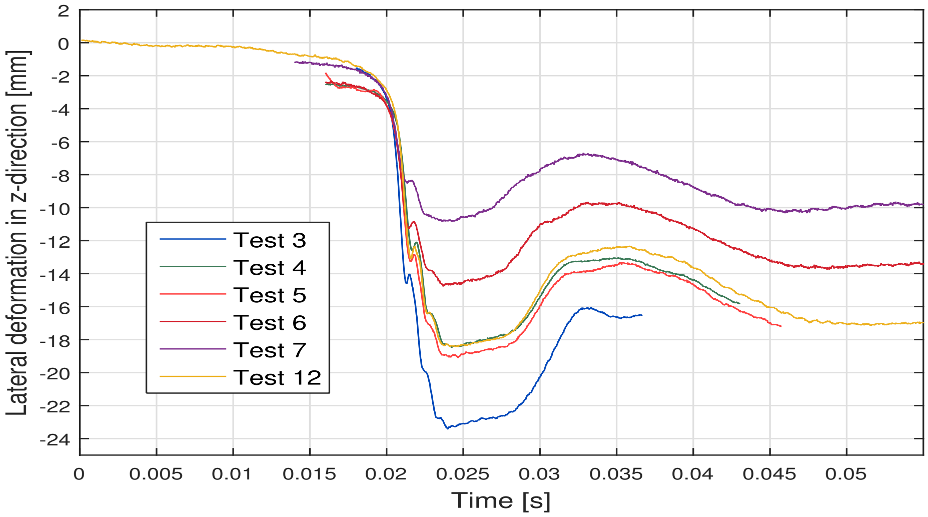

Figure 7.16: Lateral deformation for drop test impacts with zero deadrise angle

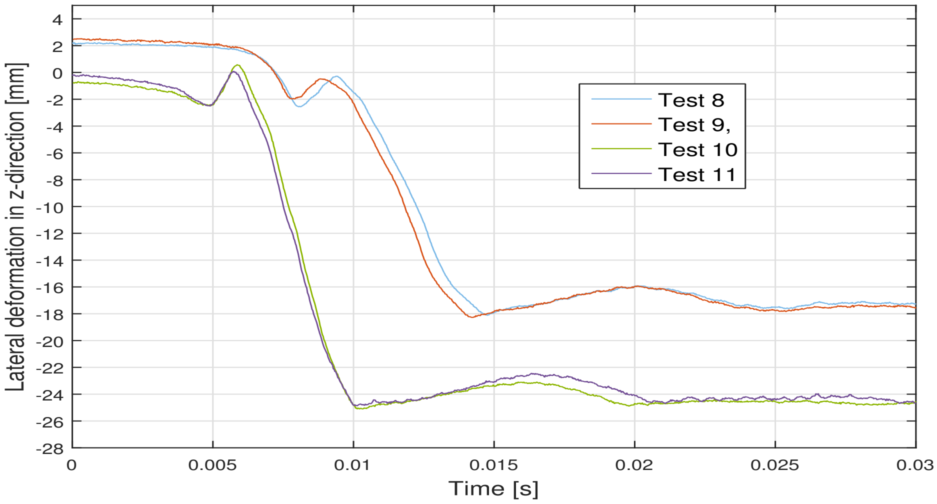

Figure 7.17: Lateral deformation for drop test impacts with 4° deadrise angle

The deformation curves in figure 7.16 and 7.17 show that although the z-location have been normalised by 57 mm, the initial position of the nodes is rarely zero, but ± 1-2 mm. The deformation profiles from the DIC calibrations showed that some of the plates have an initial surface curvature of 1-2 mm before the drop tests had started. For most of the tests, this initial bulk was in the negative z-direction, but for test 10 and 11 the bulk was in directed along the positive z-direction. It was discovered that the initial bulk was caused by thermal expansion of the plates due to the light from the lamps next to the DIC cameras. In test 12, the lamps were *only* turned on when the pictures were taken with the DIC cameras, and the initial position of the node in test 12 is therefore approximately at z=0. Even though test 4 and 5 has an initial curvature in the plate and test 12 does not, there is a negligible variation between their maximum deformation and deformation profiles. It is therefore assumed that the initial deformation due to thermal effects is negligible for the plastic deformations in the plate.

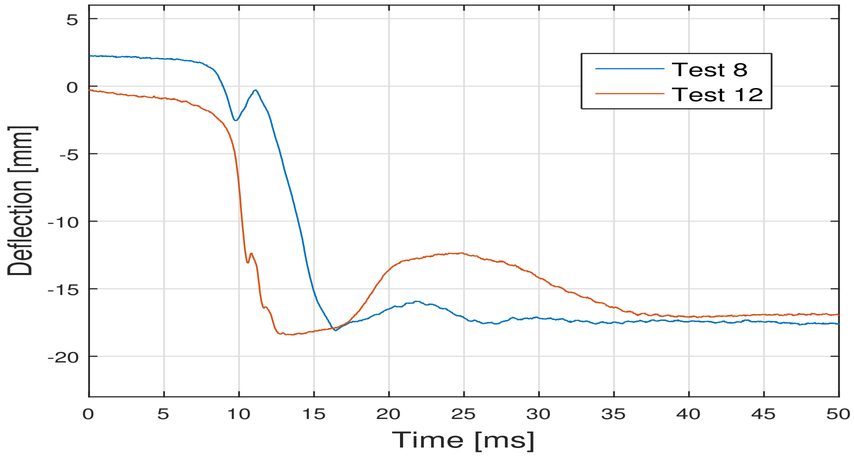

Figure 7.18: Comparison of maximum deformation for drop test 12 with 0 ° impact angle and test 8 with 3 ° impact angle

Figure 7.18 compares the deformation curve for 0 and 4 degree impacts angles with the same drop height. The maximum deformation is reached earlier for the flat plate, and the elastic recovery is also larger. The difference between the permanent plastic deformations for the two plates is small.

7.6.4 Results from High-speed Underwater Camera

Figure 7.19 shows photographs captured by the underwater high-speed camera. The pictures show the bottom of the aluminium plate in test 5 as it impacts the fluid surface with 0° deadrise angle. In figure 7.19(b), an air pocket is trapped beneath the plate. According to Faltinsen (1990), air may be entrapped under the plate surface if the deadrise angle is small. Four yield lines along the diagonals of the plate are observed. The formation of the hinges is consistent with the plastic yield line theory for a quadratic metal plate with clamped boundaries. Small air bubbles is visible in figure 7.19c. Air bubbles may be formed when the air cushion collapses. In figure 7.19d, the dent has been formed at the upper horizontal edge of the aluminium plate.

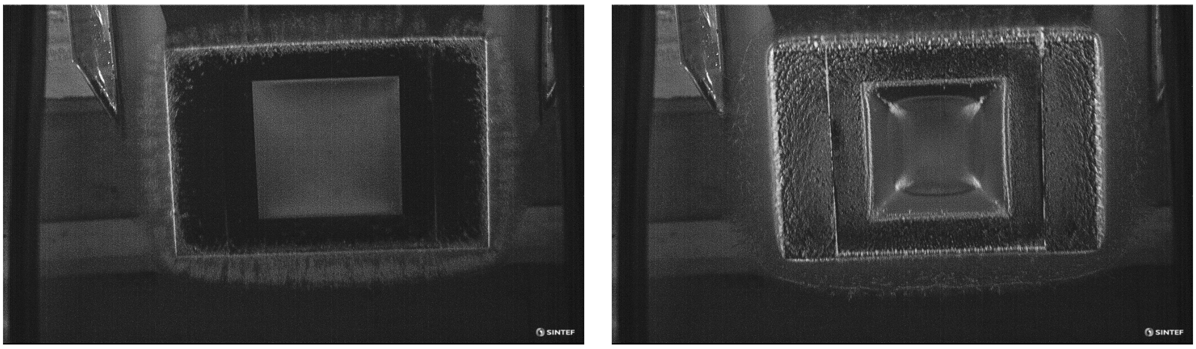

(a) t = 0 ms - The plate touches the water

(b) t = 1.67 ms - Air is entrapped beneath the plate

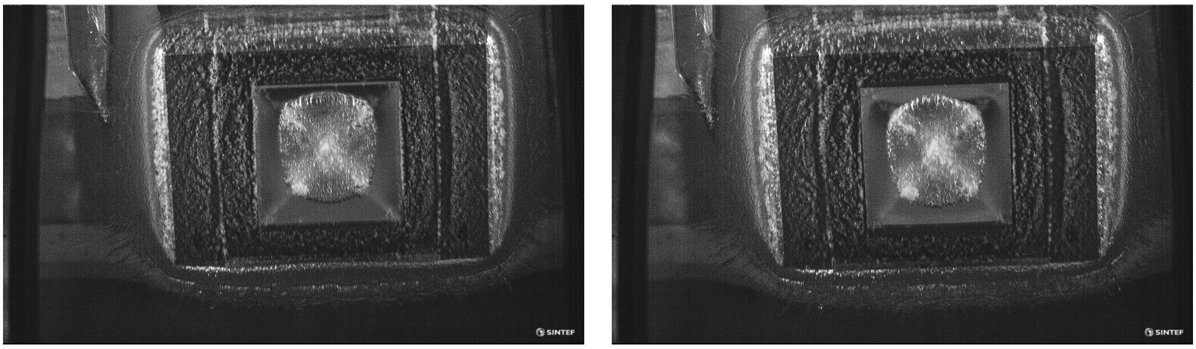

(c) t = 7 ms - The air divides into smaller bubbles. The plastic yield lines on the plate are clearly visible

(d) t = 9.67 ms - A dent is formed on the near the edge of the upper boundary

Figure 7.19: Pictures taken by the underwater high speed camera for drop test 12 with zero deadrise angle and drop height 44.4 cm

According to Faltinsen (2005), the importance of the entrapped air increases for decreasing impact angles. In figures 7.20, the plate is dropped from 44 cm, but with a deadrise angle of

4 degrees. As the plate is increasingly submerged, the air is pushed away from beneath the plate surface, and it is evident that the volume of entrapped air is much smaller compared to the flat plate. In figure 7.20d, the formation of the dent is observed.

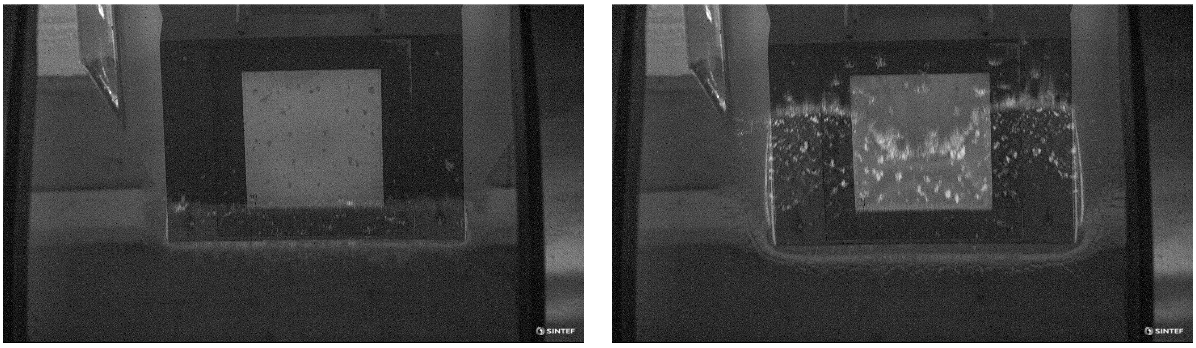

(a) t = 0 ms - The plate touches the water

(b) t = 3.3 ms - The plate is increasingly submerged

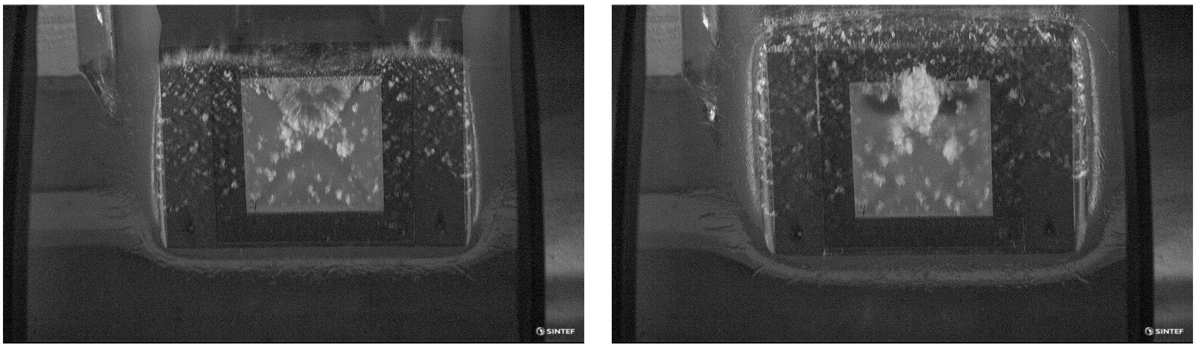

(c) t = 5.3 ms - The plate is almost completely submerged ms

(d) t = 11.3 ms - A dent is formed near the edge of the upper boundary. A small air pocket is entrapped near this edge

Figure 7.20: Pictures taken by the underwater high speed camera for drop test 9 with 4° deadrise angle and drop height 44.4 cm

7.6.5 Accelerometer and pressure sensors

The measured accelerations from 4 accelerometers at the bottom of the impactor are integrated with respect to time in order to estimate the impact velocities. The tangential impact velocity of test 3 is shown at t=0 in figure 7.21(b). The tangential velocity estimates from the accelerometers from test 3 are 3.71, 3.72, 3.61 and 3.61 m/s. A mid-plate tangential impact velocity of 3.81 m/s was calculated based on equilibrium between the kinematic and potential energy of the pendulum motion of the rig arm. The tangential velocities are calculated from equilibrium considerations for all the impact scenarios, and will be used as the initial velocity in the numerical simulations of the drop test experiments.

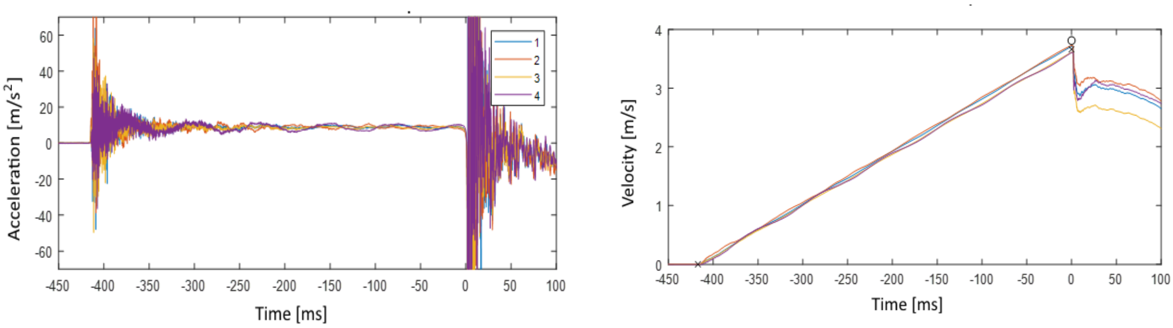

(a) Acceleration at the center of the plate measured by 4 accelerometers

(b) Tangential velocity at the center of the plate derived from the acceleration curves

Figure 7.21: Acceleration and velocity derived from the accelerometers. T=0 ms refer to global time t=20.13 s

Chapter 8

Drop Tests of Unstiffened Plate in LS-Dyna

In this chapter, finite element simulations of the experimental drop test have been performed in LS-Dyna with an explicit ALE formulation. The drop test rig is simplified to a deformable aluminium plate embedded in a rigid plate with the same outer dimensions as the bottom of the impactor. Gravity effects are not included, but the entire plate is instead given an initial velocity corresponding to the measured impact velocity from the experimental tests.

8.1 Modelling of Water and Air

Similarly to the drop test with the stiffened plate in chapter 4, the fluid-structure impact has been modelled with an ALE formulation and a FSI coupling algorithm. Water and air are modelled as Eulerian null materials, and the plate is Lagrangian. The fluid elements are masters, and both the deformable aluminium plate and the rigid steel plate are defined as slave elements. The parts that should be defined as slaves should be the model parts that impacts the fluid surface. If the rigid plate is not included in the slave formulation, the water jet acts as if the rigid plate is not there.

There are several different options for the ALE formulation of air and water. For the drop test performed with the stiffened plate, the air and water were modelled with *ALE single material and void*, where the air is approximated as a vacuum. The unstiffened plate is modelled with *ALE multimaterial* formulation where both water and air are modelled with individual material properties. The coupling of the fluid and structure can either be performed with both fluid materials or limited to the fluid with the highest density. For the drop tests in this chapter, the coupling is only activated between the water domain and the slave elements. Air and water are modelled as Eularian Null materials with properties from table 8.1 and with EOS Gruneisen parameters defined in table 2.2. The merging of surface nodes in the multi-material formulations enables modelling of the free surface with both air and water present in the same element.

Table 8.1: Material properties for water in LS-Dyna

	Material type	Density $\rho[kg/m^3]$	Dynamic viscosity μ at 25°C [-]
Fresh water	Null	1000	1.0E-03
Air	Null	1.18	1.84E-05

8.2 Material Calibration

8.2.1 Quasi-static Tensile Test

Uniaxial tension tests were performed on samples from the aluminium A1050 H111 plates. The experimental drop tests were performed with material 2, but the uniaxial tests are performed with material 1. The difference between material 1 and 2 is expected to be negligible. Tensile tests with a strain rate of 10 mm/min are performed on six samples shown in figure 8.1. Tests 1-3 have rolling direction along the length of the specimen, while the rolling direction for tests 4-6 is along the width of the specimen. The initial geometry of the test specimens are given in table 8.2 and illustrated in figure 8.2.

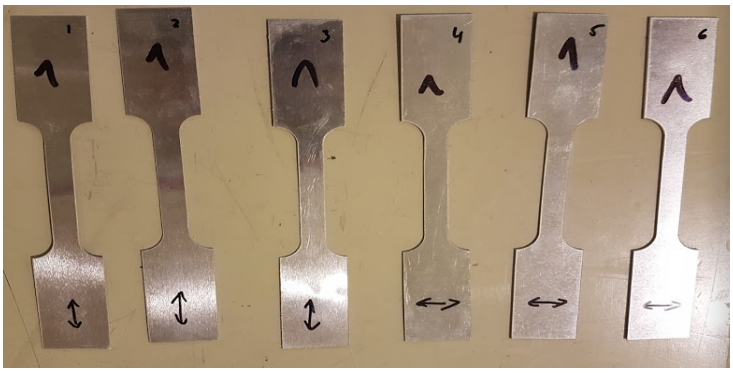

Figure 8.1: Tensile test samples nr. 1-6 of aluminium A1050 H111 with material 1 used in the tensile test

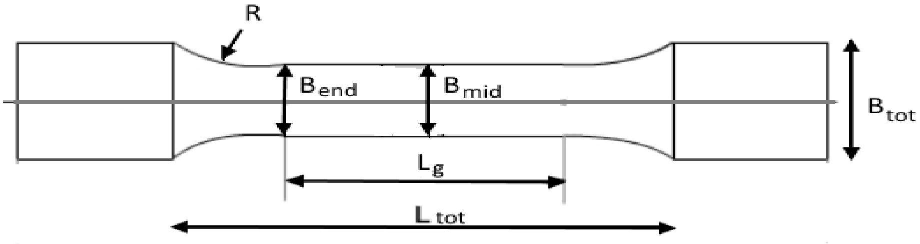

Figure 8.2: Main dimensions of the tensile test specimen

Table 8.2: Main dimensions of the test specimen

	L_g [mm]	L_{tot} [mm]	B_{mid} [mm]	B_{end} [mm]	B_{tot} [mm]	R [mm]	Pretension [N]
Test 1	49	68	10	9.9	28	9	-8.5
Test 2	49	68	10	9.9	28	9	50.8
Test 3	49	68	10	9.9	28	9	40.3
Test 4	50	68	9.95	9.9	28	9	57.3
Test 5	50	68	9.95	9.87	28	9	50.7
Test 6	50	68	9.95	9.87	28	9	56.7

The shoulders of the specimen are clamped and the gauge section is elongated until failure. The damaged test specimens after the tensile test are shown in figure E.1. The engineering stress-strain curves in figure 8.3 are established from the force-elongation curves from the tensile tests and the initial geometry of the specimen. The true stress- true strain curves are calibrated from the engineering stress-strain curves with equation 2.38 and 2.39. The engineering stress and strain curves show that the yield stress in the material is approximately σ_y = 35 MPa and that the ultimate tensile strength is σ_{ts}= 72 MPa.

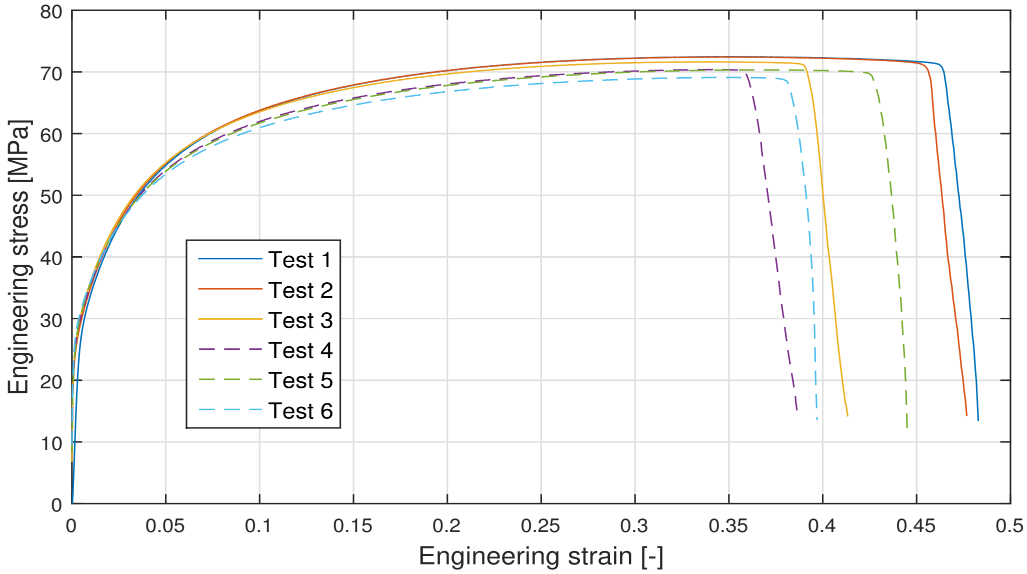

Figure 8.3: Engineering stress-strain curve calibrated from the tensile test

The curves show that the rolling direction of the specimens have an negligible effect on the strength of the material. An average sample test is found by multiplying the true stress-true strain curve from test number 2 with a factor of 0.985. The approximated curve in figure 8.4 is used as input for the stress-strain curve in the material formulation in LS-Dyna.

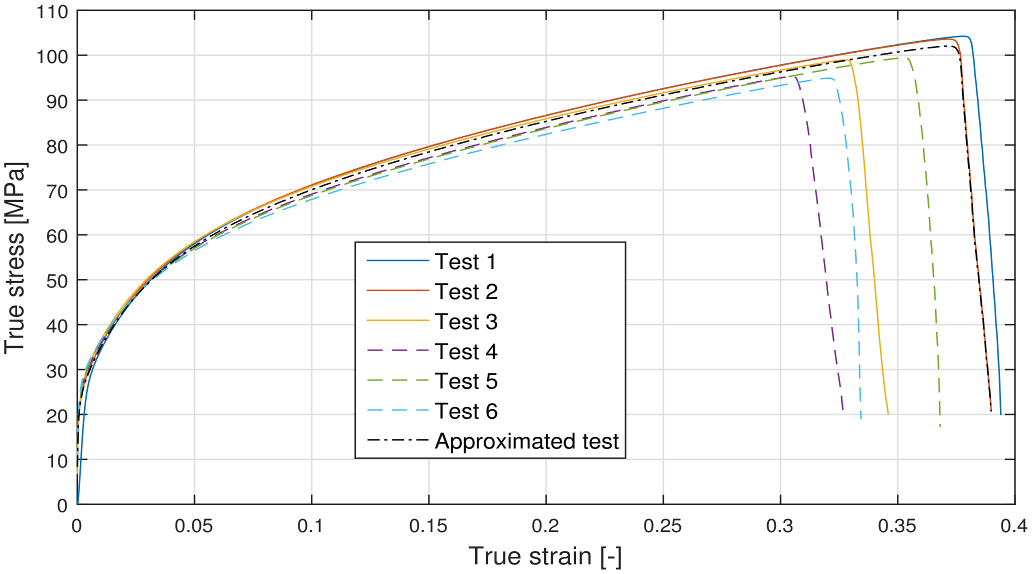

Figure 8.4: True stress - true strain curve calibrated from the tensile test

8.2.2 Calibration of Johnson-Cook Parameters

In LS-Dyna, a simplification of the Johnson-Cook constitutive relation may be applied if thermal effects and damage are unimportant. The term related to thermal softening is therefore omitted. According to Kılıçaslan et al. (2016), the strain rate sensitivity in aluminium alloys will be small up to strain rates of $1000s^{-1}$. By assuming that the aluminium plate is rate independent, the strain rate sensitivity constant C=0. Hence, the second term in the Johnson-Cook equation may also be neglected. The unknown parameters A, B and n are obtained by fitting the Johnson Cook equation for the flow stress to the true stress-effective plastic strain curve calibrated from the tensile tests. The closest fit is obtained by application of the problem solver function in Excel and the least square method. The fitted Johnson-Cook flow stress is shown in figure 8.5 with optimised parameters A = 0 MPa B = 124.7 MPa and n = 0.248.

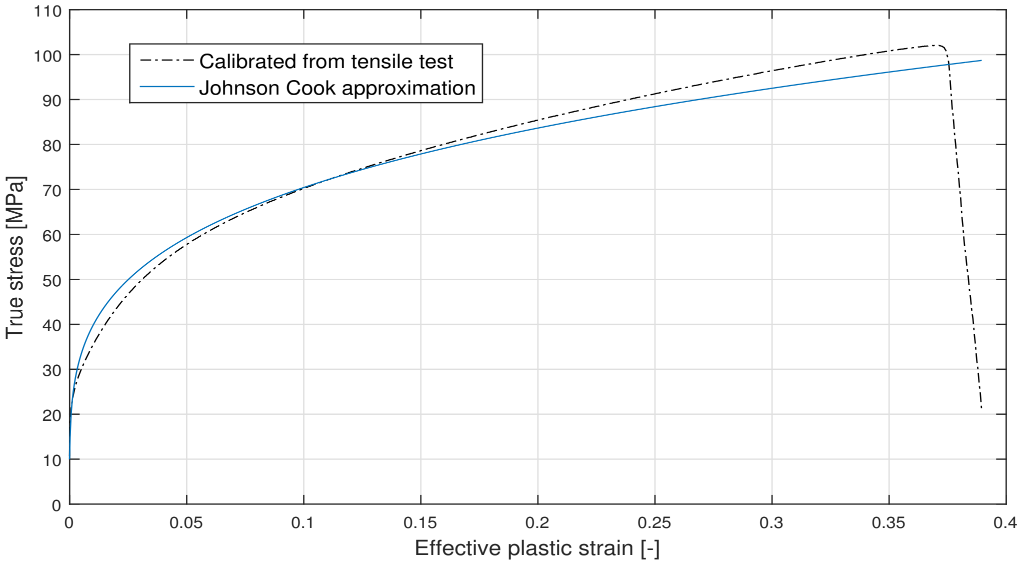

Figure 8.5: Calibration of Johnson Cook constitutive relation

8.3 Finite Element Model

The impactor in the experimental drop test has been simplified in the numerical simulations. The models in figures 8.6 and 8.7 were considered. Both of the models have the elasto-plastic aluminium plate mounted to the bottom of the structure. The aluminium plate has the same plate area and thickness as the experimental sample, but the bent edges are not included. Instead, the boundaries of the aluminium plate are directly clamped to the surrounding rigid plate. Both models hit the free surface with the same area as in the experimental impact. The FE model in figure 8.6 is a detailed representation of the experimental impactor. Although several details regarding material, stiffeners and other details have not been considered, the main structural dimension of the impactor are included. The rigid box is made of 8-noded solid elements of rigid S355 steel, while the upper part of the impactor is made of rigid shell elements. In figure 8.7, the entire impactor is simplified to a rigid steel plate with 4-noded shell elements. The rigid steel plate has the same plate thickness as the aluminium plate. Both of the impactor models have the same weight as the total weight of the experimental drop test rig. The density of the rigid parts of the structure is increased so that a total weight of 139.4 kg is obtained.

The impactor models estimated almost identical deformations and pressure variations across the deformable plate, but the CPU time of the detailed model in figure 8.6 was much more computationally demanding. The simple model was therefore chosen to represent the drop test impact. The fluid domains are modelled as two rectangular boxes discretised into quadratic solid elements with merged nodes at their intersecting surfaces.

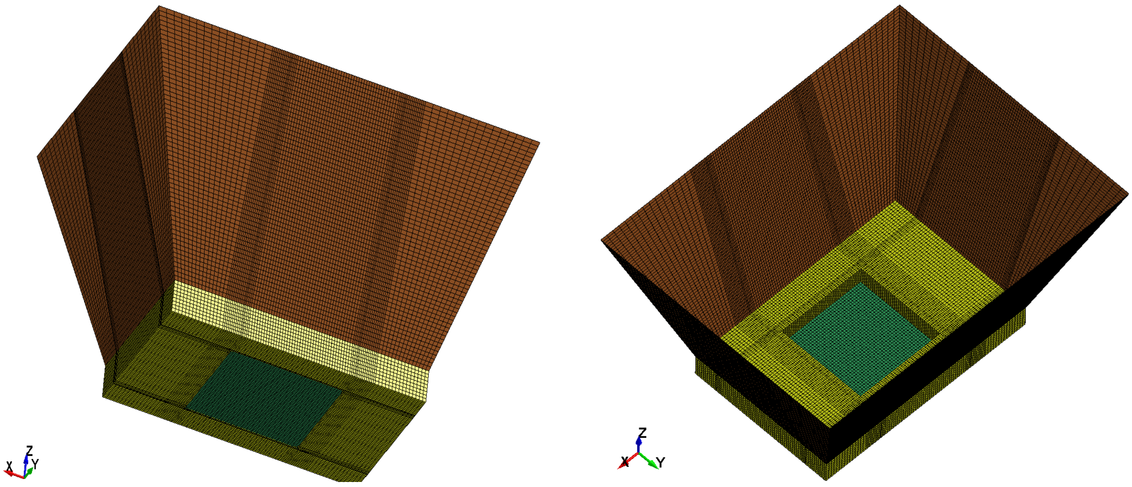

(a) (b)

Figure 8.6: Finite element model of impactor in LS-Dyna

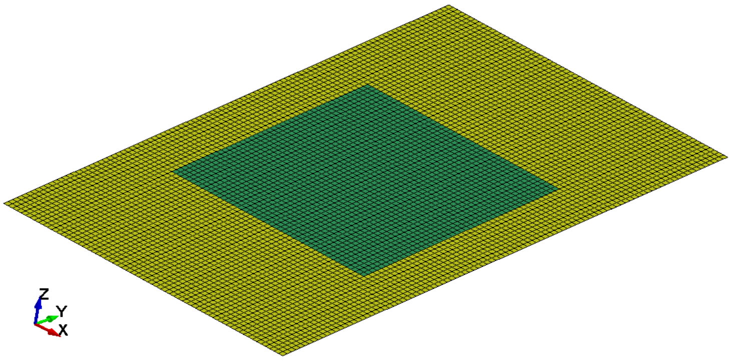

Figure 8.7: Simplified finite element model of impactor in LS-Dyna

The drop test mechanism in the numerical simulation is also a simplification of the experiment. Instead of starting the impact at a certain drop height and let the plate fall towards the surface, the impact velocity has been defined as the initial velocity of the plate. The starting position of the plate is then a less than a centimetre above the free surface. The idealisation of the impact reduces the computational time significantly because the free fall is neglected. In order to account for the rotational motion induced by the rotation of the drop test rig, the initial velocity has both a horizontal and vertical velocity component.

The elasto-plastic material of the aluminium plate is modelled with the *Piecewise linear plasticity* material in LS-Dyna. The calibrated true stress - true strain curve in figure 8.4 is used directly as input in the material model. The linear material parameters for the deformable and rigid plates are summarised in table 8.3. As for the previous tests, no damage model has been defined in the material formulation.

Table 8.3: Linear material properties for the unstiffened plate

Material	Behaviour	ρ [kg/m^3]	E [GPa]	ν [-]
Aluminium A1050 H11	Elasto-plastic	2720	72	0.32
Steel S355	Rigid	1.91E7	210	0.3

8.3.1 Convergence Tests

A comprehensive convergence test has been performed for finite element discretisation of the fluid domain and the structural parts. The model parts have only been discretized into quadratic shell or solid elements. Among the variables tested in the convergence study are the effect of changing the size of the fluid domain, mesh refinement with equal size of fluid and structural elements, and mesh refinement for either the fluid or the structural parts.

It should be noted that the convergence tests in figure 8.8 were performed before the final true stress - true strain curve was found. A comparable stress-strain curve for A1050 O from Zhang et al. (2014) was used instead. This curve had a higher resistance to plastic deformations than the calibrated curves, and thus the predicted lateral deformations from the convergence tests will be lower. In the convergence test, the aluminium plate has dimensions 20x20 cm^2 and the rigid impact area is 50x32 cm^2. The dimensions of the model was updated several times after the convergence test. A velocity of 3.8 m/s in the vertical direction has been applied for all the tests. In the convergence tests, only the deformable plate has been included as a slave. This error was discovered before the final simulation where both the deformable and rigid plate are defined as slaves. It was assumed that although these updates and errors will have a considerable effect on the maximum deformations, the optimum mesh and the effect of mesh refinement would not be changed.

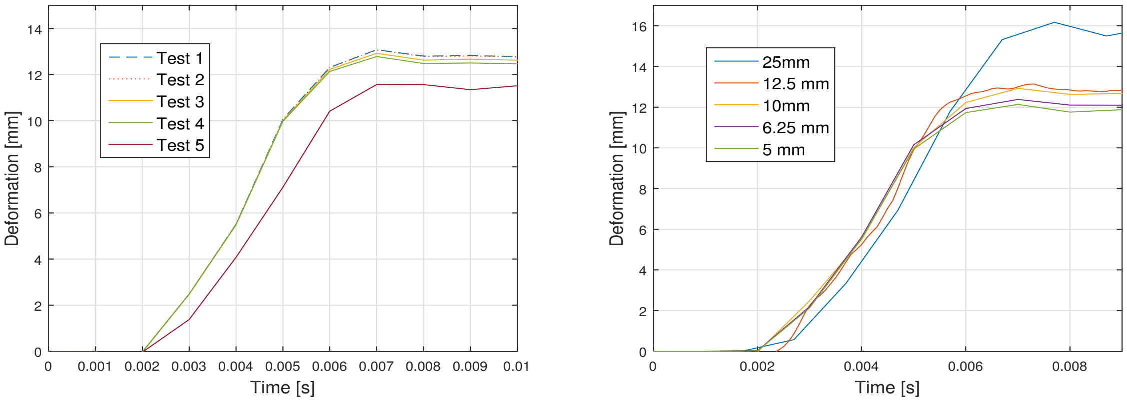

(a) Convergence of fluid domain. The mesh size of fluid and structure is constantly h_e=10mm

(b) Convergence of finite element discretization of fluid and structure with equal mesh size

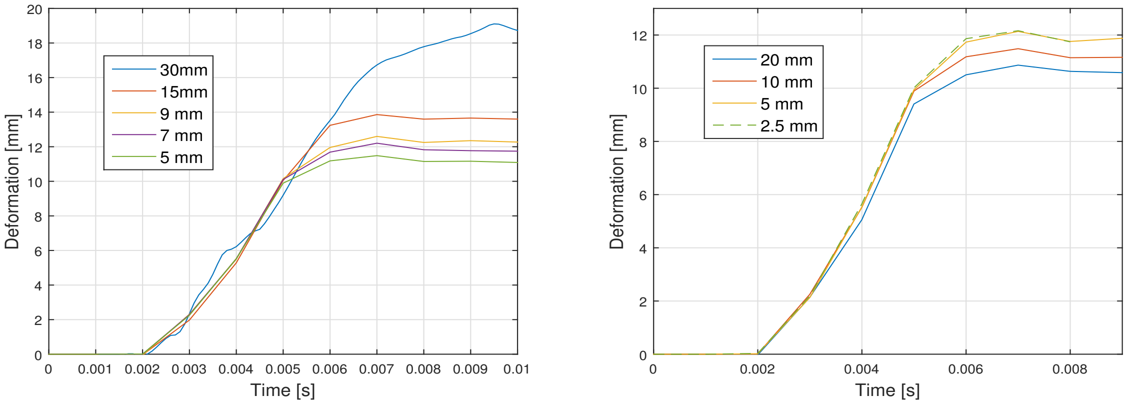

(c) Convergence of fluid domain. Mesh refinement are performed on the fluid elements with a constant structural mesh of h_e=10mm

(d) Convergence of structure. Mesh refinement are performed on the plates with a constant fluid mesh of h_e=10mm

Figure 8.8: Convergence tests for the numerical model of the drop test with the unstiffened plate with $\beta = 0$ and V=3.8 m/s

The various convergence tests for the unstiffened plate are shown in figure 8.8. The plots show the deformation of the middle of the plate as a function of time. In figure 8.8a, the effect of changing the size of the fluid domains has been tested. The mesh size of the fluid and structure elements are constant to h_e = 10mm. Test 1 has the largest domain of air and water with length, width and height equal to 1.23, 1.5 and 0.7 m, respectively. The smallest fluid domain is modelled in test 5, where the length is 0.5 m, the width is 0.65 m and the height is 0.22 m. The length refers to the direction parallel to the x-axis of the plate. The results in figure 8.8a show that the optimum fluid domain should be larger than test 5. Test 3, with length = 0.7 m, width = 0.9 m and height = 0.35 m, is therefore chosen as a sufficiently large area for the fluid domain. The dimensions of this fluid domain have been applied for the following convergence tests and numerical simulations.

Figure 8.8b shows the results from a convergence test where the mesh size of the fluids and plates have been kept equal. To reduce the computational time for the smallest meshes, the fluid area that is not in direct contact with the impacting plate has twice as large finite element size as in the finite elements in the impact area. The numerical solution has converged when the element size is smaller or equal to 6.25 mm.

In the numerical FSI problem, the coupling between the master and slave elements depends on the relation between the size of the structure and fluid elements. In LSTC (2003) is has been recommended to use the same mesh for the master and slave parts.

In Cheon et al. (2016), slamming drop tests with a stiffened plate with zero impact angle were performed in LS-Dyna. It was found that when the Eulerian mesh size was much larger than the Lagrangian mesh, the coupling began too early. When the Lagrangian elements were larger than the fluid mesh, leakage in the structural elements was observed. In the converge tests for the unstiffened aluminium plate, neither early coupling nor leakage have been observed. In figure 8.8c, the structural mesh is 10 mm, while the mesh of the fluid is refined. When the fluid mesh is 3 times larger than the structural mesh, the response is overestimated. The deformation converges as the fluid mesh approaches the structural mesh, but as the fluid discretisation gets even finer than the structure, the deformations continue to decrease.

In figure 8.8(d), the size of the fluid elements is 10 mm, while the structural mesh is refined. The results have converged when the structural mesh is 5 mm, which is half the size of the fluid elements. This result contradicts the results in figure 8.8(c) where the results converge as the size of the fluid elements become smaller than the structural mesh. A possible reason for this could be that the convergence is caused by decreasing the mesh, and not due to the ratio between size of the master and slave elements. In Cheon et al. (2016), the optimum finite element discretization was obtained with equal mesh size for both the structure and fluid model. Based on the convergence test, the optimum mesh for all elements is chosen to be 5 mm. The model of the impactor with the ideal mesh is shown in figure 8.7, and the optimum mesh sizes have been summarised in table 8.4.

Table 8.4: Summary of dimensions and finite element discretization for numerical drop test simulation with unstiffened plate

Part	Length [mm]	Width [mm]	Height/thickness [mm]	Mesh size [mm]
Aluminium plate	220	220	0.6	5
Rigid plate	340	500	0.6	5
Water domain	700	900	250	Inner = 5, outer = 10
Air domain	700	900	100	Inner = 5, outer = 10

8.4 Drop Test Conditions

The drop tests in LS-Dyna have been performed for all the combinations of drop heights and impact angles that were tested in the experiment. The first number in each category in table 8.5 represents the rest of the impacts in that category. This means that the tests in LS-Dyna are denoted 3, 4, 6, 7, 8 and 10. Based on the equilibrium between the potential and kinetic energy of the pendulum motion of the rig, the horizontal and vertical velocity component in the middle of the impactor may be calculated. For each of the drop heights, the velocity components just before the impacts have been calculated and used as input for the initial velocity in LS-Dyna.

Table 8.5: Calculated impact velocities from experimental drop test

"Drop heigth" [cm]	Angle	Test number	Horizontal velocity [m/s]	Vertical velocity [m/s]
77.8	0	3, 1, 2, 12	-0.334	-3.796
44.3	0	4, 5	-0.253	-2.873
22.2	0	6	-0.179	-2.038
11.8	0	7	-0.131	-1.487
44.4	4	8, 9	-0.237	-2.699
84.5	4	10, 11	-0.326	-3.712

8.5 Results

8.5.1 Simulations in LS-Dyna

The maximum deflections of the aluminium plates are summarised in table 8.6. For the flat plate, the maximum deformation occurs in the middle of the plate. For the inclined plate, the maximum deformation is shifted from the middle and towards the end of the plate that hits the plate last. The maximum deformation increases for increasing impact velocity. For a drop height of 44.3 cm, the maximum deformation for the flat plate is 24.8% larger than for the inclined plate.

Table 8.6: Maximum deformations from drop tests simulated in LS-Dyna representing the experimental drop tests

Test	"Drop height" [cm]	Max deformation [mm]
3	77.8	26.74
4	44.3	21.09
6	22.2	15.54
7	11.8	11.39
8	44.4	15.85
10	84.5	22.12

Figure 8.9 shows the lateral deflection of the plates dropped with a zero impact angle. After the maximum deformation is reached, there are almost no elastic vibrations in the material. The permanent plastic deformations are only slightly smaller than the maximum deformations. The deformation profiles have a symmetric cosine shape. The x-axis in figure 8.9 corresponds to the x-axis in figure 7.12(a).

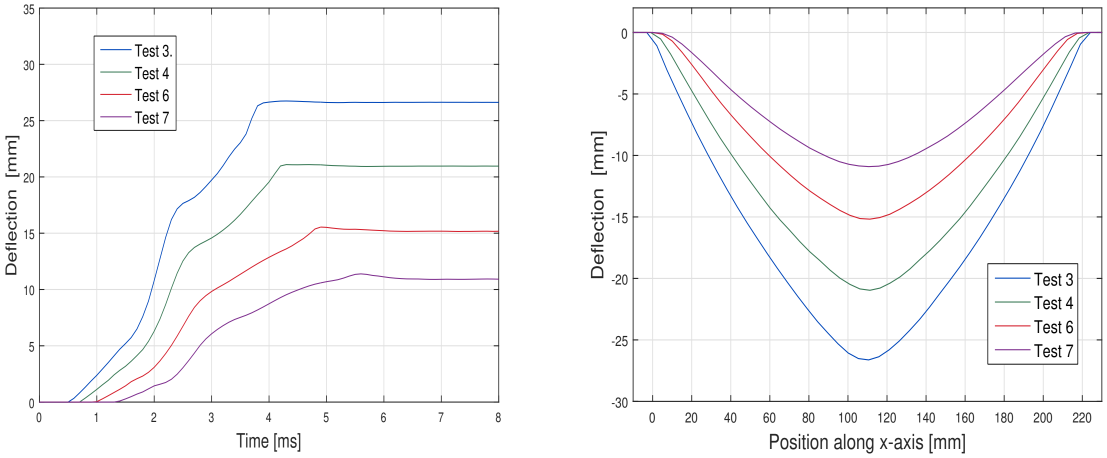

(a) Temporal displacement variation during the drop test impact

(b) Deformation profiles in the in the middle of the plate along in positive x-axis direction

Figure 8.9: Maximum out-of-plane deflection for drop tests with zero impact angle in LS-Dyna

Contrary to the flat impact where the deformation profile has a cosine shape, the maximum displacement travels across the inclines plate as a skewed cosine wave. The final deformation shape along the global x-axis can be seen in figure 8.10(b). The maximum deformation does not occur in the middle of the plate, but is shifted. Figure 8.10(a) shows the lateral deformation of the plates with an impact with a 4° deadrise angle. A small bump in the deformation curve is observed at the beginning of the impact. When lower edge of the flexible plate first impacts the free surface, a small pulse is sent through the plate causing a deformation wave across the plate. As an increasing part of the plate gets submerged, a larger deformation wave travels across the plate and causing permanent plastic deformations. There are little elastic vibrations in the material after impact, so the permanent plastic deformations are approximately equal to the maximum deformations.

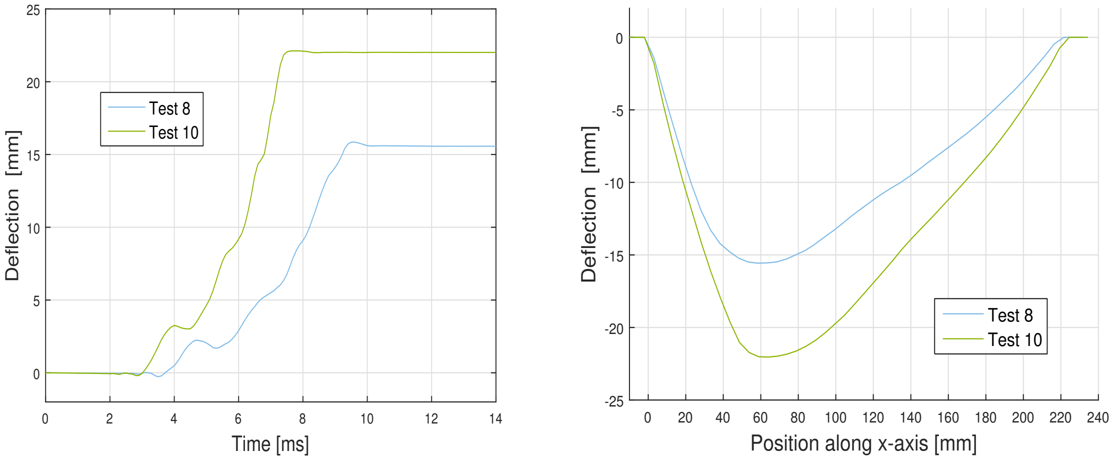

(a) Temporal displacement variation during the drop test impact

(b) Deformation profiles in the in the middle of the plate along in positive x-axis direction

Figure 8.10: Maximum out-of-plane deflection for drop tests with plates with 4 degree impact angle in LS-Dyna

In figure 8.11, several time steps during the submersion of the plate have been marked along the deformation curve at the node with maximum lateral displacement in LS-Dyna. The location of maximum deformation is located 16.1 cm from the end of the aluminium plate that first hits the water. The graph shows that no significant deformation is introduced to the node at the position of maximum deformation before the fluid has reached more than 1/3 of the plate.

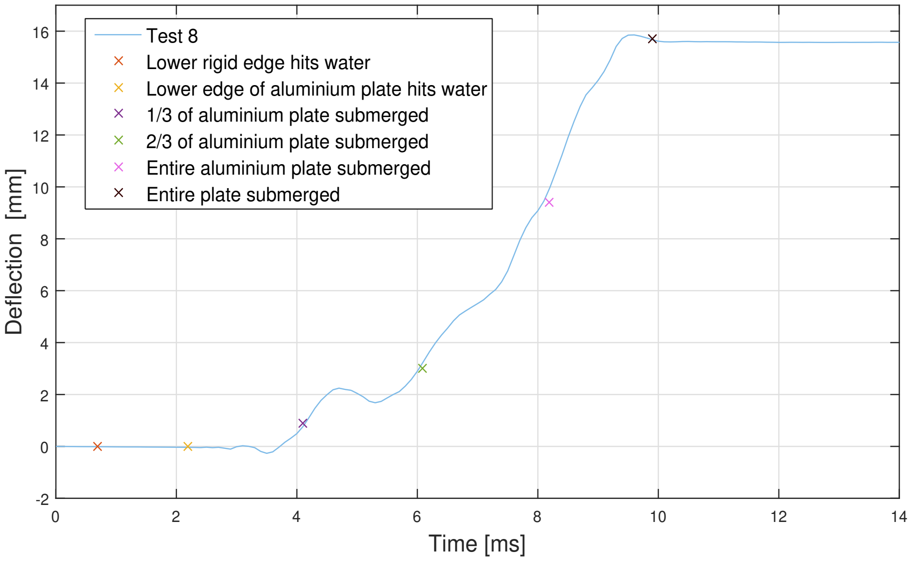

Figure 8.11: Displacement of the inclined plate in drop test 8. The submersion of the plate is marked on the deformation curve

The ALE material formulation of the Eulerian fluid elements and the Lagrangian structural elements can be modelled with air as a void or with its real material properties. Drop test 3 has been modelled with both *ALE multi-material* and *ALE single material and void* formulation in figure 8.12. Although the properties of air are defined in the multi-material formulation, the penalty coupling algorithm is restricted to coupling between the plates and water. When the air is modelled as a void, the maximum deformation is 1.14 mm larger. The deformation curve for the multi-material formulation is smoother than the single material formulation. There is no deformation of the plate for neither of the formulations before the plate hits the water at t=0.5 ms. This means the effect of air on the plate before it hits the water has not been properly accounted for.

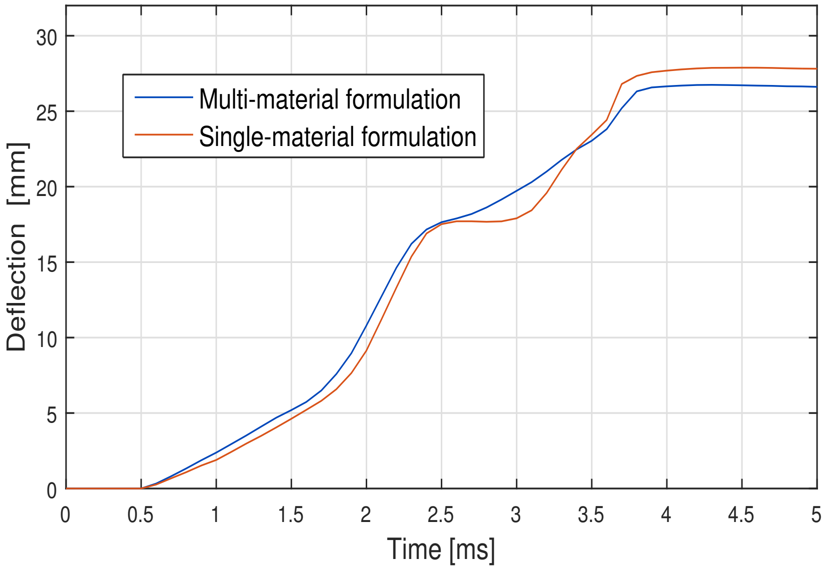

Figure 8.12: Comparison between *ALE single material and void* and *ALE multimaterial* formulation for drop test 3 in LS-Dyna

8.5.2 The Effects of Strain Rate Sensitivity in Johnson-Cook

In drop test 3, the DIC cameras measured that a maximum deformation of 23.41 mm had been reached 4 ms after impact. The engineering strain in the plate due to the lateral deflection was $\varepsilon = 0.0223$. The strain rate is found as $0.0223/0.004 = 5.57\ s^{-1}$. According to Kılıçaslan et al. (2016) strain rate effects in aluminium are not important for strain rates lower than 1000 s^{-1}. Even though strain effects are not expected to be important for the deformation of the aluminium plates, the Johnson-Cook material model was applied for simulations with test 3. In figure 8.13, the Johnson-Cook material model with different strain rate sensitivity constants have been compared with the piece-wise linear plasticity model with the calibrated true stress-true strain curve. When C=0, the strain rates effects have been neglected in the Johnson-Cook formulation. The difference between the linear plasticity model and the Johnson-Cook material model is less than 1 mm. Some discrepancy is expected because the true stress- effective plastic strain curves in figure 8.5 does not coincide completely. According to Hopperstand and Børvik (2017), typical values of C for aluminium and steel at room temperature range between 0.001 and 0.01. It is observed that increasing the value of the strain rate sensitivity parameter to C=0.01 or C=0.015 has a negligible impact on the maximum deformation.

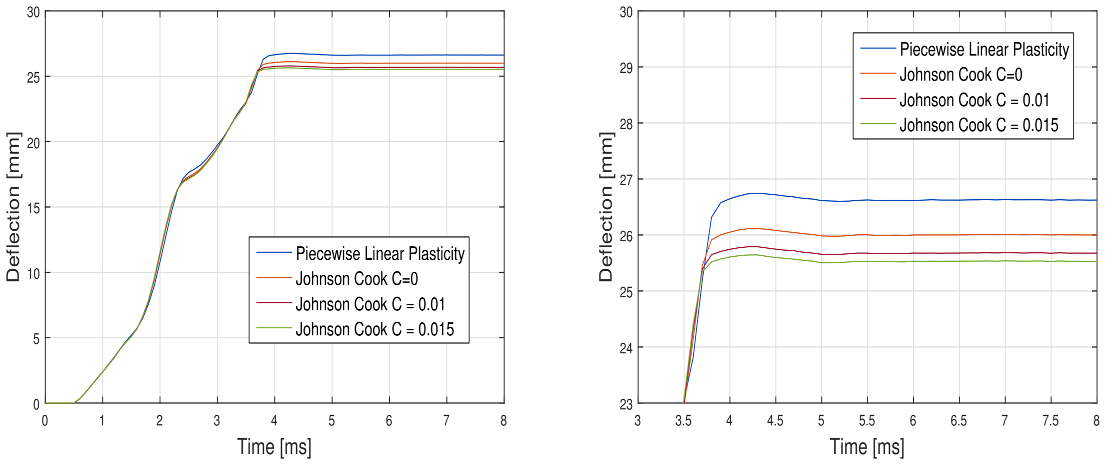

(a) (b)

Figure 8.13: Maximum deformations for test 3 with Johnson Cook material formulation with various values for the strain rate sensitivity parameter C

8.5.3 Comparison of LS-Dyna and DIC Measurements

Maximum Deformation

The estimated lateral deformations of the flexible plates in LS-Dyna and DIC have been compared. The difference between the maximum displacements has been summarised in table 8.7. For the flat plate impacts, the numerical simulations overestimate the displacement, while for the inclined plates, the deformation is underestimated. The results coincide best for the impacts with the smallest drop heights.

Table 8.7: Comparison between the maximum displacements predicted by LS-Dyna and measured by DIC cameras

Test	Relative difference between max deformation from LS-Dyna and DIC [%]	Difference between max deformation from LS-Dyna and DIC [mm]
3	14.22	3.33
4	14.09	2.60
5	10.45	1.99
6	5.21	0.77
7	5.27	0.57
8	-12.53	-2.27
9	-13.24	-2.42
10	-11.87	-2.98
11	-11.52	-2.88
12	14.59	2.69

The maximum lateral deflections of the plates with zero deadrise angles found by DIC and LS-Dyna are plotted in figure 8.14. Before the plate has penetrated the water, the DIC measures an initial deflection of the plates which is not observed in the simulations in LS-Dyna. The effect of thermal heating of the plates has already been discussed. However, for some of the drop tests, the displacement has increased from the initial DIC photograph and the photograph taken just before impact. This indicates that the pressure of the air trapped beneath the plate might contribute to deformation of the plate before the actual impact. The deformation curves coincide well during the first phase after the impacts. The DIC deformation has more elastic vibrations before the maximum deformation is reached. Contrary to the results in LS-Dyne, a large elastic strain recovery after the maximum deformation is observed in the DIC deformations.

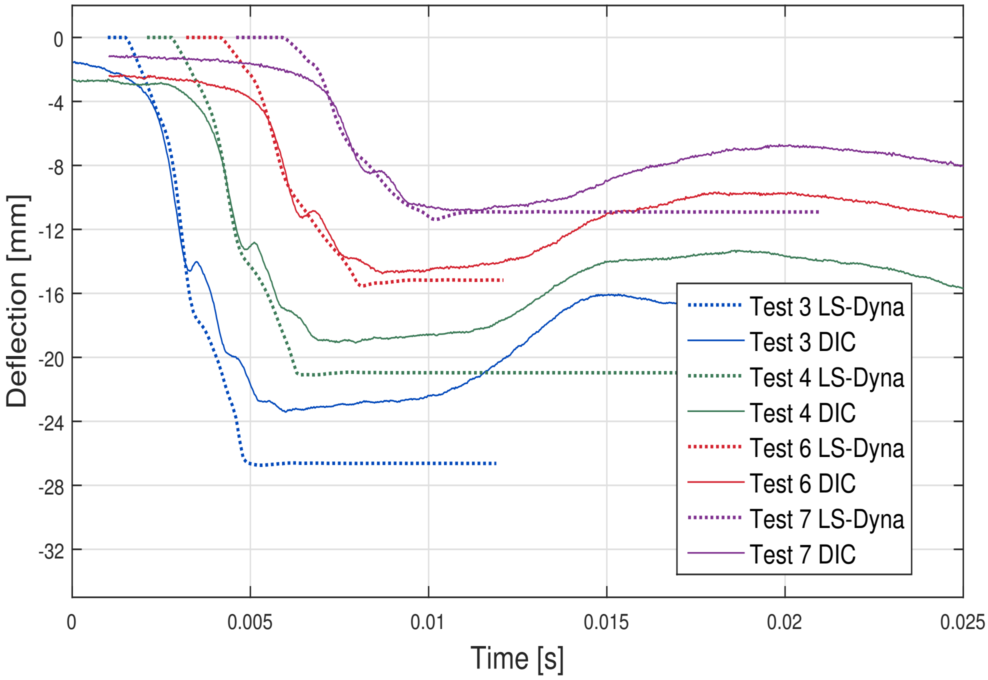

Figure 8.14: Comparison of maximum lateral plate deflection from LS-Dyna simulations and DIC measurements for drop tests of plates with zero impact angle

In figure 8.15, the deformation curves coincide well for the majority of the impact for drop test with 4° impact angle. The simulations in LS-Dyna do not fully capture the early deformations in the plates, or the elastic recovery after the maximum deformation has been reached.

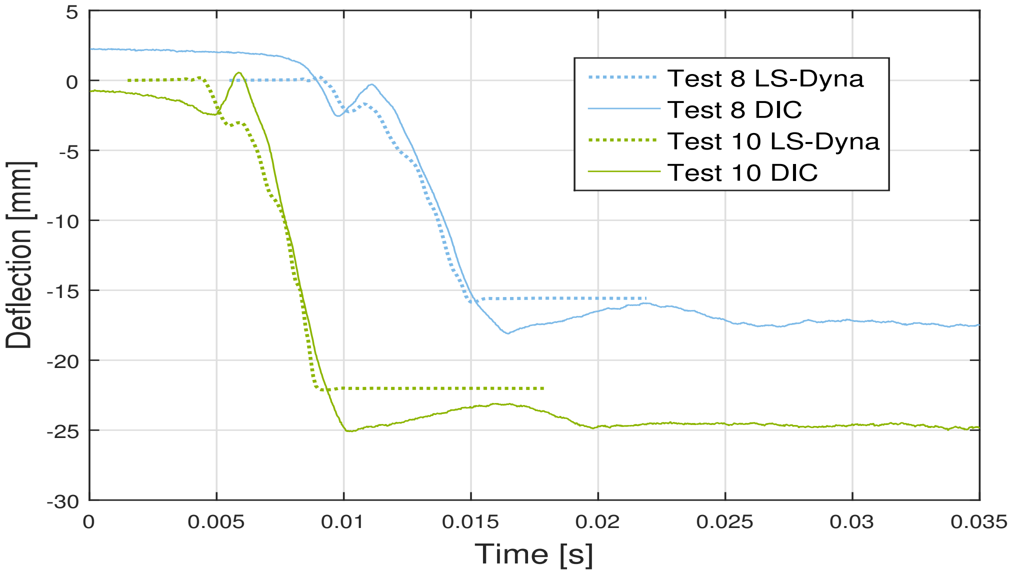

Figure 8.15: Comparison of maximum lateral plate deflection from LS-Dyna simulations and DIC measurements for drop tests of plates with 4° impact angle

8.5.4 Deformation Profiles

The deformation profiles for test 12 and 8 have been plotted at different points in time during the deformation. These time instants have been marked by dotted lines in the time scale for the maximum deformation in figure 8.16 and 8.18. The deformation profiles for test 12 and 8 are shown at in figure 8.17 and 8.19, respectively. In the plots of the deformation profiles, the lateral deflection in z-direction is plotted along the middle of the plate parallel with the x-axis. The curve for the DIC profiles has a smaller span along the x-axis than the deformation profiles from LS-Dyna. This was because boundaries of the rigid steel box made it impossible to photograph the entire effective area of the flexible plate. However, the mid-points of the plates from DIC and LS-Dyna are both located in x = 0. The structural response from LS-Dyna and DIC show that for the flat drop test impacts, the plate will deform in a cosine pattern with increasing maximum amplitude in the centre of the plate. For the inclined plate in test 8, the deformation travels across the plate like a wave, and the maximum does not occur in the middle.

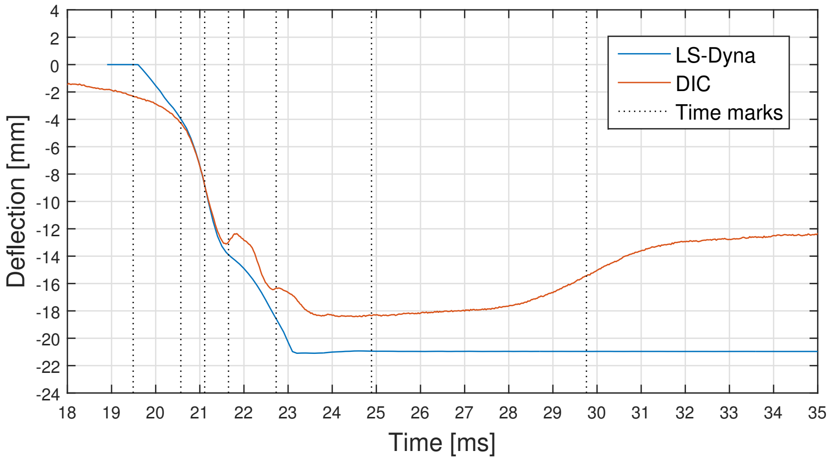

Figure 8.16: Deformation profiles from LS-Dyna and DIC for test 12 with drop height 44.4 cm and zero impact angle

Figure 8.17(a) shows the initial deformation before the drop test for the plate with β=0° in test 12. As previously mentioned, the thermal effects were limited for test 12. The DIC measurements show that there is almost no curvature of the plate prior to the drop test impact. Figure 8.17(b) shows the plate deflection right before the plate hits the water. Here, a cosine curvature of 2 mm is observed from the DIC measurements. It has been argued that a probable cause of this deflection is due to entrapped air. The deformation profile from LS-Dyna will not be deformed by the air pressure, and hence has zero deflection before the plate hits the water.

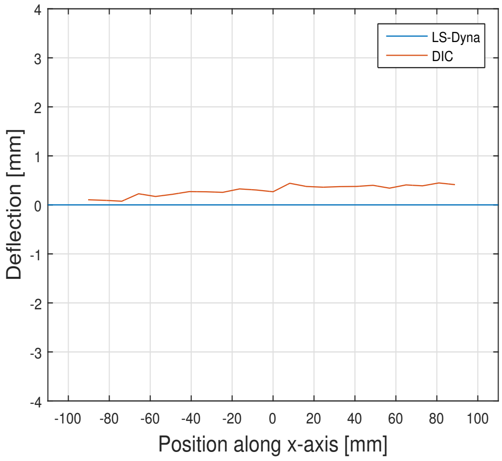

(a) Initial t=0

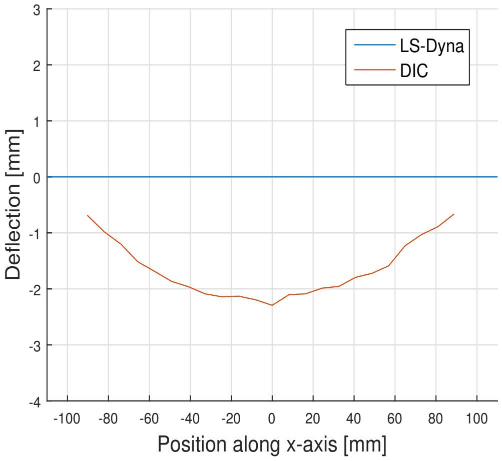

(b) t = 19.5 ms

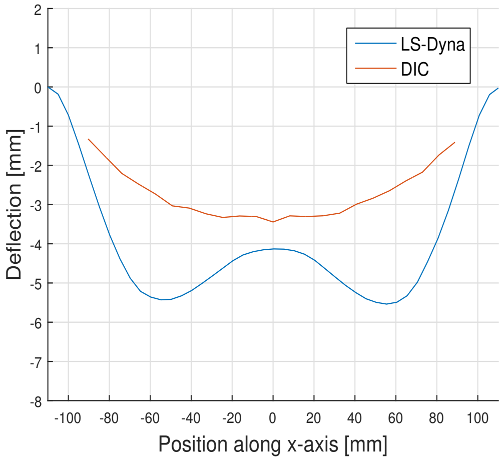

(c) t = 20.57 ms

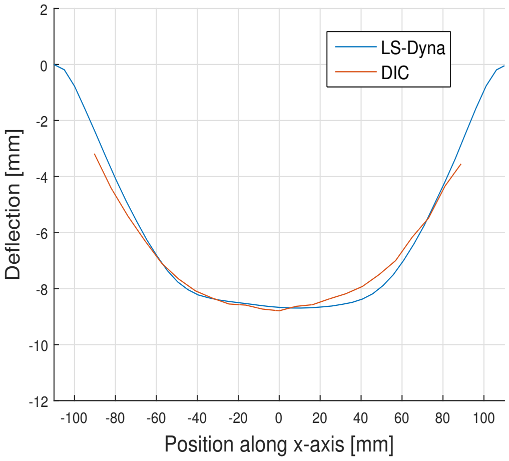

(d) t = 21.1

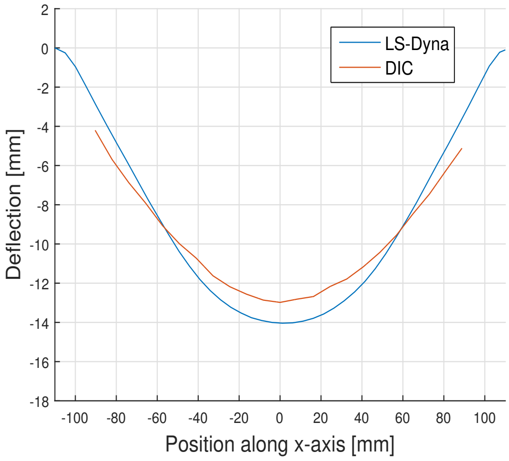

(e) t = 21.65 ms

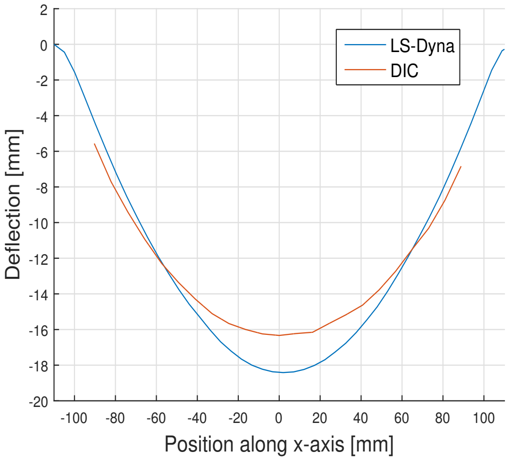

(f) t = 22.73 ms

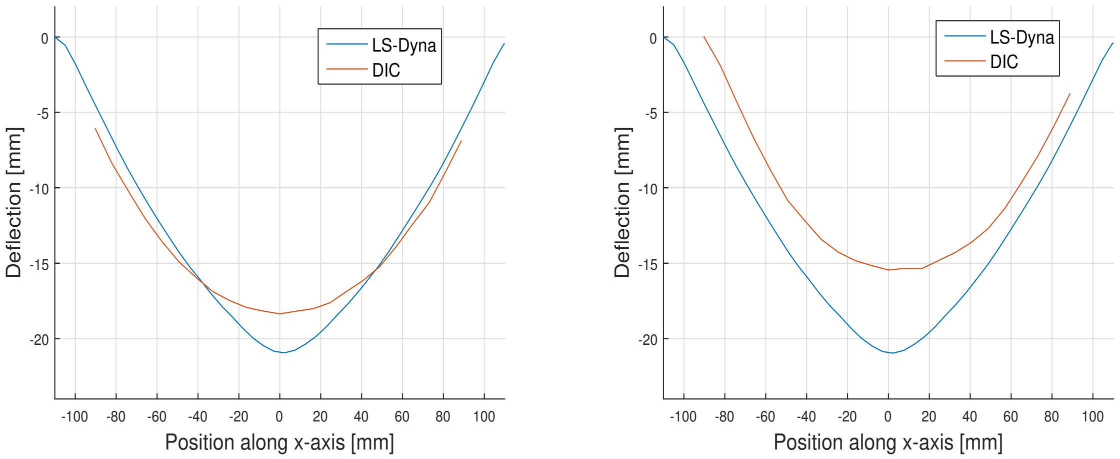

(g) t = 24.9 ms

(h) t = 29.76 ms

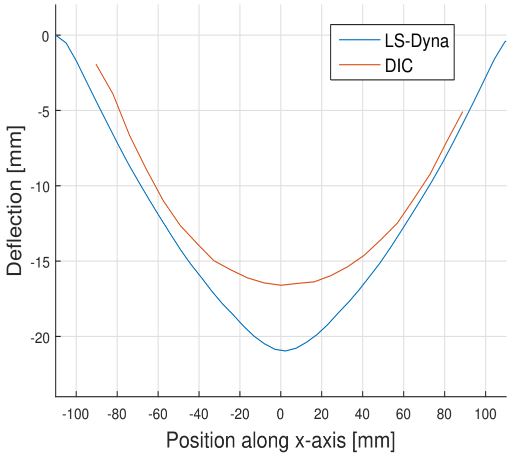

(i) Permanent deformations

Figure 8.17: Deformation profiles from LS-Dyna and DIC for test 12 in the xz-plane along the middle of the plate. The deformation profiles are plotted for the dotted time steps in figure 8.16

The graphs in 8.16 coincide completely between t = 20.6-21.5 ms. As predicted by the graphs, the profile deformations from DIC and LS-Dyna at t=21.1 ms in figure 8.17(d) agree well. As the deformation approaches maximum, the plate deforms in a cosine pattern. The profiles are similar for most of the time steps, but the mid-plate deformation is overestimated by LS-Dyna. The deformation profile at maximum deformation is shown in figure 8.17(g). After the maximum deformation has been reached, DIC measurements show that the plate retracts and a dent is formed. At t=29.76 in figure 8.17(h) the dent has been formed at the plate boundary at x=-80mm. When the final plastic deformation pattern is reached in figure 8.17(i), the retraction has been relaxed. However, the dent has not recovered completely and there is an asymmetry in the cosine deformation pattern from DIC.

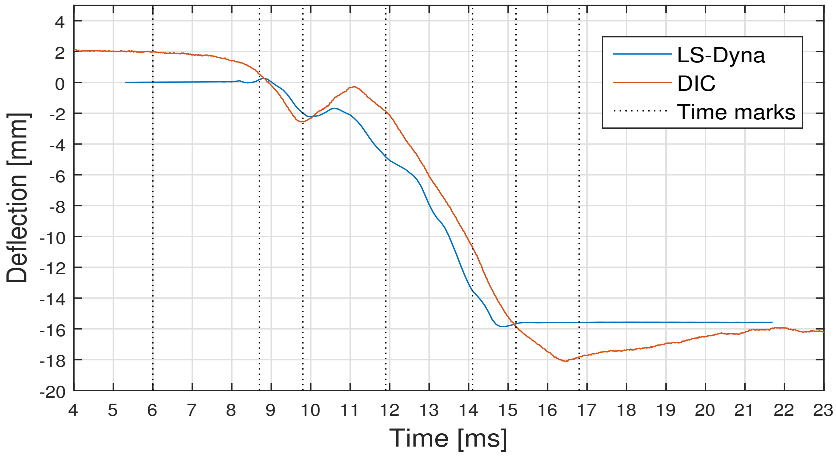

Figure 8.18: Deformation profiles from LS-Dyna and DIC for test 8 with drop height 44.4 cm and 4 ° impact angle

Contrary to test 12, test 8 has an initial curvature of 2 mm due to thermal expansion. The initial deformation profile prior to the drop tests is shown in figure 8.19(a). Figure 8.19(b) shows the deformation profile in the beginning of the submergence of the plate. It is observed that the deflection of the profile has not changed from the initial curvature during the free fall through water. The small change in deflection indicates that the air has a negligible effect on the deformation of the inclined plate.

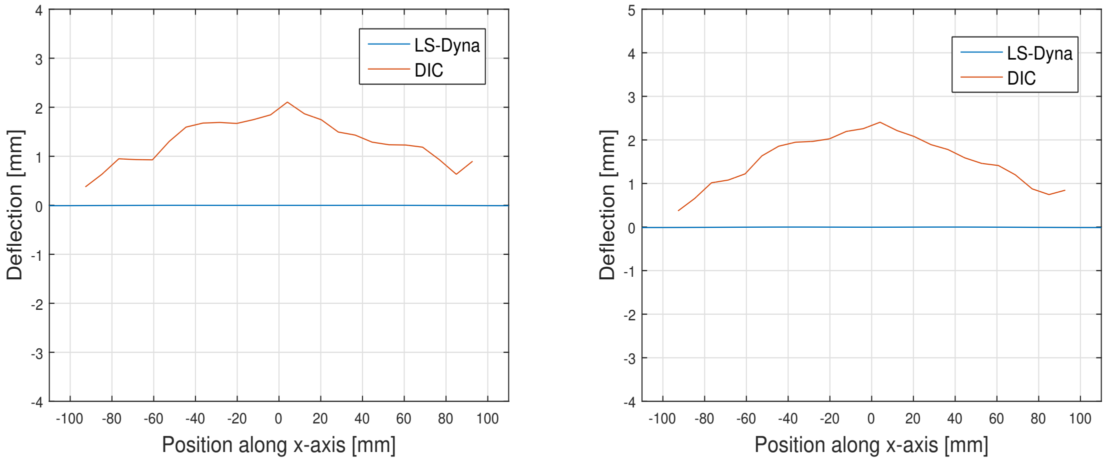

(a) Initial t=0 **(b)** t = 6 ms

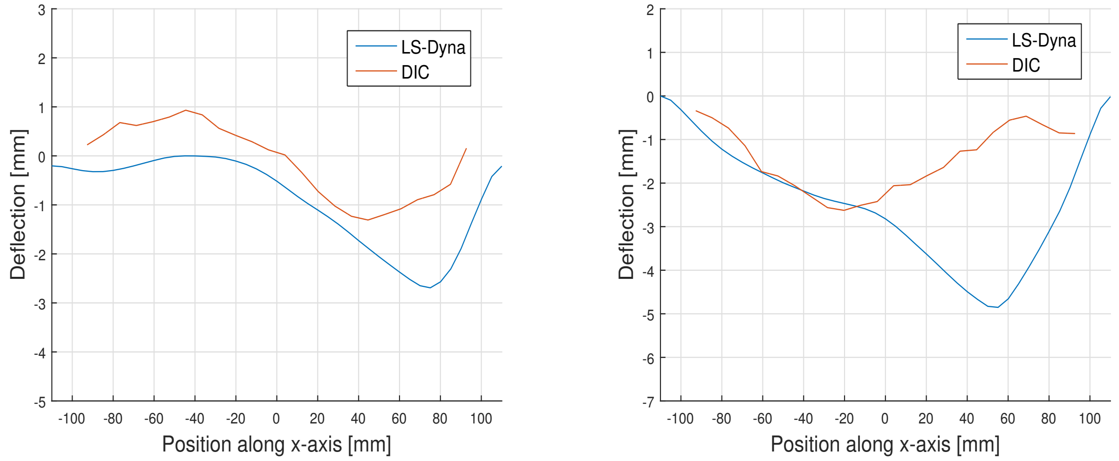

(c) t = 8.7 ms **(d)** t = 9.8 ms

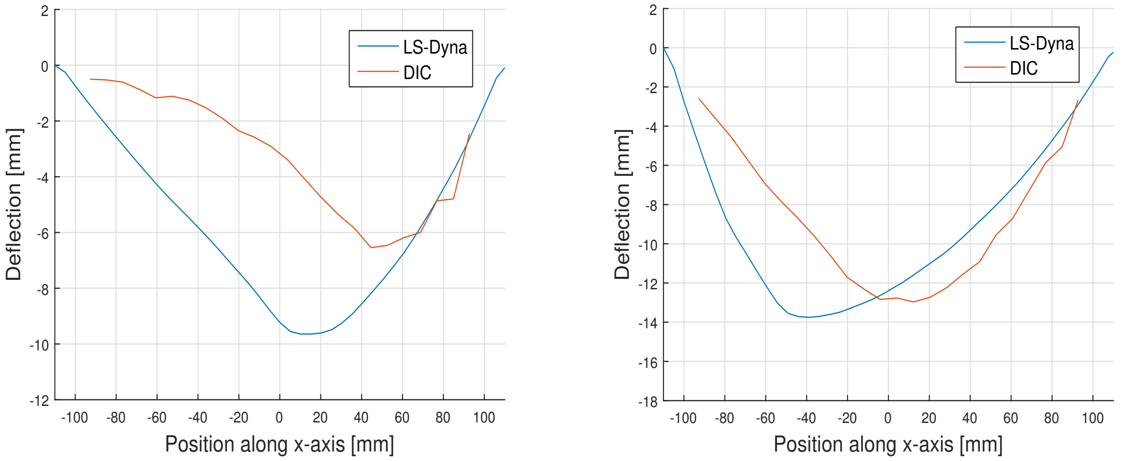

(e) t = 11.9 ms **(f)** t = 14.1 ms

For the inclined plate, the maximum deformation travels across the plates as a skewed cosine wave. As the flexible plate hits the surface, approximately between figure 8.19(b) and (c), a small disturbance is created in the plate profile. In the LS-Dyna simulation, a large deflection immediately builds up near the end that first impacts the water. This deflection travels across the plate with increasing amplitude until the plastic deformation pattern is reached. In the deformation measured by DIC, a smaller deflection wave is sent across the plate. This can be seen from figure 8.19(c) to 8.19(d). In figure 8.19(e), the main deformation from DIC builds up near the lower edge.

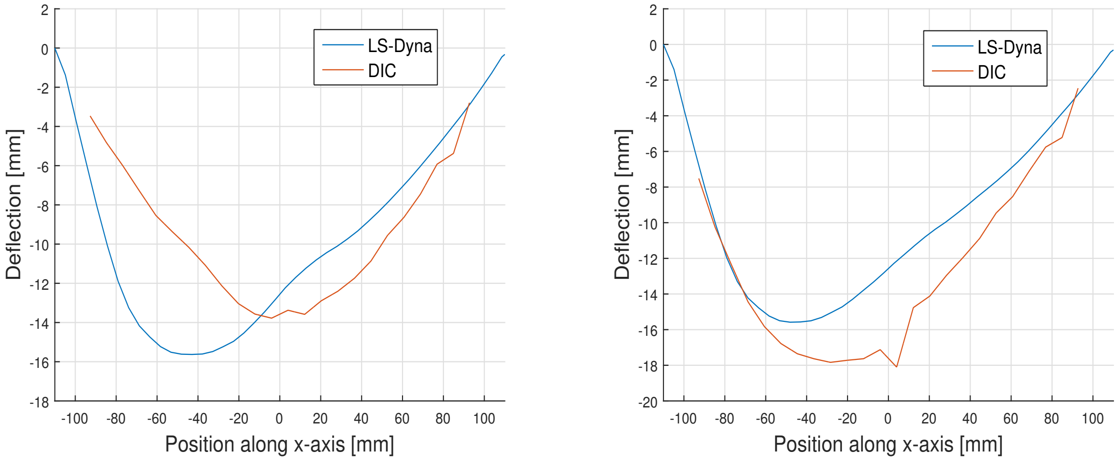

(g) t = 15.2 **(h)** t = 16.8 ms

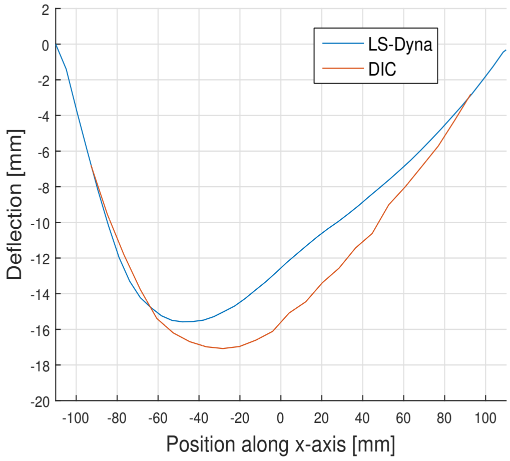

(i) Permanent deformation

Figure 8.19: Deformation profiles from LS-Dyna and DIC for test 8 in the xz-plane along the middle of the plate. The deformation profiles are plotted for the dotted time steps in figure 8.18

The maximum deformation for both curves are shown in figure 8.19(h). There is an error peak in the DIC plot at x=5 which should be ignored. Contrary to the flat impact, LS-Dyna *underestimates* the maximum deformation for the inclined plate. The maximum response of the DIC deflection is located more towards the centre of the plate. The deformation profiles for the inclined plate did not coincide as well as for the flat plate.

Chapter 9

Discussion

Model tests and numerical simulations have different advantages when it comes to representation of the slamming impact event. The benefit of the model tests is that most physical phenomena, such as air entrapment and the spray root, will be included for a realistic model. The main disadvantages are little flexibility in changing impact conditions, high costs and time. Numerical simulations offer high flexibility, low cost and will normally be less time-consuming. However, the numerical code needs to be validated by experimental data to ensure that the results are consistent with physical reality. To perform an accurate validation of the numerical code, possible sources of error and uncertainties in both the finite element program and the model test must be evaluated.

9.1 Experimental Drop Tests

9.1.1 Effect of Impact Conditions and Measurement Techniques

During the assembly of the drop test rig, the aluminium plate was bolted to the rigid steel box and then mounted to the bottom of the impactor. Both of these procedures were performed manually, which makes it more challenging to ensure identical initial conditions for drop tests at the same height and impact angle. To minimise the occurrence of these errors, the impact surface of the aluminium plate and rigid steel box was ensured to be completely smooth before the assembly was mounted to the impactor. The entire rig was then lowered to the waterline level to check that the impact position of 0 or 4° was correct. The differences between the permanent deformations found by the Mitutoyo measuring machine, the dial gauge and by DIC were small. This indicates that the accuracy of the DIC measurements is good. The accuracy of the DIC measurements was emphasised by the comparison of the permanent deformation profiles from DIC and Mitutoyo in figure 7.15 which coincide exactly. The distance between the top of the rigid box and the aluminium plate was measured to be 57 mm. This distance was assumed to be constant for all of the drop tests. If there are any variations during the assembly of the rigid-flexible plate structure, this length will vary and the assumption of a constant distance of 57 mm will yield inaccurate calibration of the DIC response. The largest deviation between the permanent deformations from Mitutoyo and DIC is 0.48 mm. For most of the drop tests, the deviation between the permanent deformations measured by Mitutoyo and DIC were minimal. The error in the mounting of the plate is included in this deviance. The small differences in the predicted response indicate that the differences in initial impact conditions are negligible.

Drop tests with the same height and impact angle have a small scatter in the permanent deformation profiles measured by Mitutoyo. The DIC measurements of the maximum deflection in figure 7.16 and 7.17 also show that the deformation history for equal impact conditions follows the same curve. The structural response show that the experiment is repetitive. For identical impact conditions, the measured elasto-plastic response falls within a small scatter.

9.1.2 Scale Effects

According to Steen (2014), some of the most important sources of error in model testing are scale effects and incorrect modelling of structure and environment. At small scales, it is challenging to build models that are geometrically similar. The model will be more complicated to assemble and all of the structural components must be correctly scaled so that they have the same structural contribution in the model and full-scale. In the drop tests in this thesis, the full scale stiffened steel plate field has been modelled as an equivalent unstiffened aluminium plate. The stiffeners increase the stiffness of the plate field. When a stiffened plate is subjected to lateral loads, the bending of the stiffener will cause membrane effects in the stiffener and plate, which will increase the capacity of the panel. If the stiffeners are neglected, the structural capacity of the plate field will be lowered. When the response from the model tests are scaled back to full scale, the effect of the stiffeners must be included.

If the plate is fixed against in-plane displacements, the lateral displacements will be supported mainly though membrane action. Thus, the unstiffened plate is scaled with respect to the membrane capacity so that the correct plastic response can be found. The bending stiffness of the plate has not been scaled correctly, which means that deformations in the elastic region will not be accurately represented by the drop tests. The model test is therefore limited to impacts from drop heights causing large plastic strains.

9.1.3 Effect of Initial Curvature from Thermal Expansion

Most of the aluminium plates had an initial curvature caused by thermal expansion due to heating from lamps. The initial curvature in the deformation profile of test 8 is shown in figure 8.19(a). It is observed that the thermal effects have caused a curvature of 2 mm. For test 12, the lamps were turned off when possible, and thus the initial deflection is almost zero as shown in figure 8.17(a). Test 4 and 5 were dropped from the same height with the same impact angle as test 12, but have initial deformations from thermal expansion. However, the initial curvature in test 4 and 5 did not result in a maximum deformation that differed significantly from test 12. The elastic behaviour for small deformations may be too soft since the elastic properties of the plate have not been scaled correctly. The effect of the initial deflections appears to have a negligible effect on the plastic response of the plate.

9.1.4 Effect of Entrapped Air

Even though test 12 has no initial curvature, the plate has a deflection of 2 mm before the plate hits the water. The deformation prior to the impact could be caused by entrapped air beneath the plate. The plate approaches the surface before the air is able to escape. The pressure from the captured air deforms the plate. Photographs taken by the high-speed camera show that a large air pocket is captured beneath the plate, and that this air pocket is especially prominent for the flat impacts. The high-speed cameras shows that for the inclined plate, the magnitude of entrapped air is smaller. During the submersion of the inclined plate, the air cushion was pushed away from the impact region. The deformation profile of test 8 in figure 8.19, shows that although the plate has an initial deflection due to thermal expansion, the deflection does not increase a lot during the free fall through the air. The curvature in figure 8.19(b) taken right before the impact does not differ from the initial deformation in figure 8.19(a). This result indicates that the entrapment of air is less severe for inclined impacts.

Although the presence of the air has been proven by the high-speed cameras, another challenge is how to quantify the effect of the air cushion before and during the submersion of the plate. In order to properly identify how the air cushion contributes to the structural response, one must know how the air cushion is compressed and how the pressure from the air acts on the plate surface. A theoretical calculation of the entrapped air has not been performed in this thesis, but would be of interest in future work.

9.1.5 Effect of the Dent in the Plate

After the maximum deformation of the plate has been reached, the displacement of the plate decreases and the boundaries are pushed back above their initial position. After this retraction, the deformation increase until the permanent plastic deformation is reached. After the retraction, the deformation profile is not as symmetrical as before the maximum deformation was reached. This is shown in figure 8.17(h) and (i). A dent is shown along the edge closest to the rig arm. The dent may have been caused by the hinged connection to the rig arm or the decelerating mechanism from the ropes that also are connected close to the hinge.

9.2 Numerical Simulations of Experimental Drop Tests

9.2.1 Limitation of LS-Dyna

According to Day (2009), the ALE compressible flow solver in LS-Dyna is suitable for simulation of rapid impacts in the order of milliseconds with high pressure and velocity gradients. From this description, it is expected that LS-Dyna will be a suitable choice for the simulation of slamming impacts. The explicit integration scheme used for transient nonlinear problems in LS-Dyna sets a limit for the time step based on the relationship between element size and the speed of sound through the material. The boundary layer effects in LS-Dyna are only defined in terms of kinematic viscosity. If the purpose of the numerical simulation is to capture the details of the water jet, a more detailed description of the surface should be introduced with a finer mesh. However, the details of the spray root were not the focus of the numerical simulations performed in this thesis.

9.2.2 Simplification of Drop Test Impact

A fluid-structure impact in LS-Dyna is a very computationally demanding simulation. Thus, several simplifications of the dimensions of the impactor and the physical details of the slamming impact were implemented in the numerical model. The impactor was simplified to a rigid steel plate with an aluminium plate clamped in the centre. The mass of the drop rig, and the area of the impacting surface are the same in the experiment and LS-Dyna. In the numerical model, the mass has been evenly distributed in the rigid and flexible plate so that the centre of gravity is located in the middle of the deformable plate. In the real model, the centre of gravity is located closer to the rig arm.

The same initial velocity has been defined for the entire plate surface. The initial tangential velocity consists of the calculated horizontal and vertical velocity components in the middle of the flexible plate from the experimental drop tests. This simplification is somewhat unphysical for the pendulum motion of the rig because the tangential velocity will vary in x-direction. Although the pendulum motion is not fully represented, it is assumed that the simplification will provide sufficiently accurate results for the drop test impact.

In the model tests, climbing ropes have been applied to stop the motion of the drop rig before it hits the bottom of the basin. The sudden retardation by ropes has not been modelled in LS-Dyna. In the numerical simulation, the only deceleration of the plate is caused by the viscosity of the water. In the experimental drop test, the inclined impactor walls and the rig arm provide additional buoyancy during the impact. In LS-Dyna, the total weight of the drop rig is equal to the experiment, but only the surface of the impactor that first hits the water is included. When the deformation variation measured by DIC and LS-Dyna is compared, the lateral displacement from DIC decreases as the ropes decelerate the impactor. The dent near the hinge of the impactor is also created during the deceleration process of the drop test impact.

In LS-Dyna, the deformation does not decrease after maximum deformation. The most probable reason for the discrepancy between the graphs after maximum deformation is the difference in damping mechanisms in the models. After the maximum plastic deformation has been reached for the drop tests in LS-Dyna, there are no elastic recovery of the material and no elastic vibrations. In order to study the elastic recovery, the elasto-plastic pressure pulse was applied to the finite element model with an added mass of 1.21 kg assuming a constant elastic 1st mode shape. Approximately the same maximum deformation was obtained, but there was not any elastic recovery in this simulation either. In appendix D, a study on the structural response for an unstiffened aluminium plate with linear plasticity has been performed for different plate thickness and yield stress. In the study, it was observed that the elastic vibrations in the material are more prominent for higher yield stress and larger thickness. The aluminium plate in the drop test has a small thickness and low yield stress at approximately 35 MPa. According to the results from the parameter study, the elastic vibrations in the material should thus not be prominent.

9.2.3 Simplification of Material Formulation

Several assumptions have been introduced to the material model of aluminium A1050 H111 in LS-Dyna. A damage model has not been implemented in the material formulation because the structural response was far from fracture. Thermal softening and strain rate effects have also been neglected. Although thermal effects were demonstrated due to the heating of the DIC lamps, the adiabatic heating *during* the impact is neglected. According to Hopperstand and Børvik (2017), the deformation process in metallic materials will generally not be adiabatic for rates lower than $10^2\ s^{-1}$. The strain rate from the drop test with highest drop height was 5.6 s^{-1}, which is considerably lower than this limit. The investigation of the strain rate sensitivity of the material with the Johnson-Cook formulation indicated that the drop test impacts were not affected by strain rates. This result agreed well with Kılıçaslan et al. (2016) stating that strain rate effects may be neglected for strain rates less than $10^3\ s^{-1}$. In conclusion, the effects that have been neglected in the material should not have a significant effect on the elasto-plastic response.

9.2.4 Effect of ALE formulation and Entrapped Air

In the ALE formulation of the fluids, an ALE multi-material formulation with air and water have been applied. The structural slave elements are only coupled with the water master elements. This means that the effect of the air pressure on the plate is not taken into account during the fluid-structure interaction. According to LSTC (2003), if one of the Eulerian materials dominates the loads imparted to the Lagrangian structure, it is a valid assumption to only have coupling between the dominant master part and the slave elements. The response in the slamming impact is dominated by the water impact and not the air entrapment.

When the structure is not coupled with air, the plate will not be deformed by air before it hits the water. This is clearly shown in figures 8.14 and 8.15, where the deflection curve in LS-Dyna is zero before the flexible plate impacts the water. The air pocket will also not impose any pressures on the plate during the impact.

In Cheon et al. (2016), it was found that air cushions in numerical analyses of slamming impacts with flat plates reduce the impact pressure and the structural response compared to simulations which neglected the effect of air. However, the reduction in response was not severe, and the effect of the air cushion was most important for small deadrise angles. The entrapped air was also found to reduce the maximum deformation by Bereznitski (2001). The numerical simulations showed that the effect of neglecting air was substantial if hydroelastic effects were neglected, but quite small if hydroelastic effects were included.

According to Faltinsen (2005), air cushions are important at the beginning of the impact, and often in a time scale smaller than the time scale for the local maximum strains to occur. The deformation curves from the maximum impact measured by DIC and LS-Dyna coincide best during the rise time of the impact. During this phase, the effect of the entrapped air will be most severe for the impact based on theory and observations from high speed cameras. Even though the air pocket is observed in the experimental drop test, the small discrepancy between the response curves indicates that the presence of the air pocket does not affect the deformation of the plate during the rise time. The results coincide well during the start of the impact even though the entrapped air has not been included in LS-Dyna. This implies that neglecting the effect of air in the numerical code can be a valid assumption.

In conclusion, LS-Dyna provide a fair approximation of the maximum deformation and manages to capture the important effects, although the elastic recovery differs between experiments and results. The differences between the FE displacements and the experimental displacements are most prominent after the maximum deformation. Several simplifications have been applied in the numerical model. Neglecting thermal softening, rate effects and damage model for the material have no significant effect on the result. The coinciding response curves from DIC and LS-Dyna during the first part of the impact indicate that the effect of entrapped air may be neglected. However, a more detailed evaluation of the entrapped air should be performed in order to draw any definite conclusions. Among the demonstrated causes of error, the most probable reason for the discrepancies in the response between LS-Dyna and DIC is the due to the simplifications of the drop impact mechanism.

9.3 Discussion of Design Procedure for Slamming Loads

In this thesis, simplified methods have been applied to estimate the deformation resistance of a stiffened plate subjected to lateral loads, and the largest out-of-plate deformation due to slamming loads. The analytical approach for calculating the deformation capacity to lateral loads provided a conservative estimation of the resistance curve for the stiffened plate. A perfectly plastic material have been assumed in the simplified method. This assumption leads to an underestimation of the capacity of stiffened plates with realistic materials with hardening. Strain rate effects in the material have not been accounted for either. The underestimation of the resistance is especially evident in the pure membrane stage where plastic hardening may be significant. The deformation capacity was also underestimated for a biaxial membrane stress state in the panel. If in-plane displacements are restricted in both longitudinal and transverse direction of the plate, the stiffened panels can, according to Amdahl et al. (2017), not be properly treated as beams if the deformations are large for the span in both directions. The present model can be further developed to account for the transverse membrane effects. For materials with a small amount of material hardening and only longitudinal membrane stresses, the method can provide reasonable results. In Amdahl et al. (2017), the simplified formulation provided better predictions of the lateral deformation resistance to point loads than uniformly distributed loads.

The SDOF analogy for estimation of response to explosion loads in RP C204 (DNVGL, 2016a) was applied to estimate the maximum displacement of the stiffened plate subjected to slamming loads. In the simplified approach, the stiffened plate was transformed into a simple mass-spring system subjected to an equivalent triangular load pulse. For modified resistance curves and load histories, the estimated response from the Biggs charts agreed well with the maximum deformation from LS-Dyna.

Both the FEA and analytical resistance curves were applied in the Biggs charts. Even though the analytical curve was more conservative than the resistance curve from LS-Dyna, the difference in predicted response from the two curves was only 1.3 mm. Since the membrane effects are much smaller in the analytical resistance curve, it was expected that the estimation of the maximum response should be larger. The simplified methods were susceptible to changes in the variables used in the Biggs charts. Small changes to the resistance and load curves resulted in quite big differences between the maximum response. The analytical wet eigen period was larger than the observed wet eigen period in LS-Dyna. This could indicate that the calculated stiffness and/or the added mass are not correct.

The effect of hydroelasticity was significant for the fluid-structure impacts with the stiffened panel. Among the tested impact scenarios, the hydroelastic interaction was most severe for 0° and 3° impact angles, and with increasing impact velocity. When the hydroelastic effects were not accounted for, the maximum response was overestimated. Thus, hydroelastic effects should be taken into account so that the structure is not designed too conservative. When the elasto-plastic plate was subjected to the elastic pressure history, the plastic response was also overestimated. The elasto-plastic response from the ULS pressure history can be used as a conservative limit for the ALS design criteria.

From these observations, it can be concluded, that by applying the elastic or rigid pressure variations to an elasto-plastic plate, a conservative estimation of the elasto-plastic deformation history can be found. The simplified method for the assessment of the resistance of stiffened panels will, in general, provide a conservative estimate for the resistance, but is more accurate for materials with low degree of hardening and a uni-axial membrane stress state. The maximum response from the SDOF analogy for estimation of response for explosion loads agreed well with the maximum dynamic response from LS-Dyna.

9.4 Validation of Design Method

In this thesis, experimental and numerical methods have been applied to the unstiffened aluminium plate model, while numerical and simplified methods have been applied to the stiffened steel plate. In RP C204 (DNVGL, 2016a), the characteristic resistance curve can also be calculated for an unstiffened plate. However, due to the small plate thickness, the membrane effects in the plate are too large to be captured by the standard tri-linearisation of the stiffness curve in LS-Dyna. The simulations in LS-Dyna were not able to provide a valid resistance curve for the unstiffened plate either. Due to limited time, other theoretical models were not applied for the unstiffened drop test impact. Theoretical methods can be validated with the obtained experimental data, and will be investigated further in the SLADE-project.

The numerical method in LS-Dyna is almost identical for the unstiffened aluminium plate and the stiffened steel plate. The only major difference is in the ALE formulation, where water is modelled as a void for the stiffened plate and with its own material properties for the drop test with the unstiffened plate. However, for the unstiffened plate, there was a minimal difference in response between the ALE single material and void and ALE multi-material coupled with water.

Experimental data from the drop test impact was applied to validate the numerical code. The unstiffened plate response in the finite element simulations agreed well with the measured experimental response by DIC. This indicates that the simulation in LS-Dyna is able to capture the slamming impact phenomenon quite well. Once the numerical code in LS-Dyna has been validated, the precision level of the simplified methods can also be determined. The estimated response from the Biggs design charts are close to the maximum response in LS-Dyna. The small discrepancy between the response from experiment and LS-Dyna, and LS-Dyna and simplified methods, indicate that both the simplified methods and LS-Dyna has provided an sufficiently accurate prediction of the maximum structural response.

Chapter 10

Conclusion and Recommendations for Further Work

10.1 Conclusion

In this thesis, experimental model tests, numerical simulations in LS-Dyna and theoretical methods have applied to estimate the structural response of plates subjected to abnormal wave slamming events. The slamming impact phenomenon is best represented in the experimental drop tests. A major benefit of the model tests was that different physical aspects of the fluid-structure interaction could be easily identified during the impact. From the high-speed camera, it was possible to observe the presence of air cushions beneath the plate and how the plastic yield lines were formed during the impact. The DIC cameras proved to be an extremely valuable tool for estimation of the structural instantaneous response of the plate. When DIC was validated with the manual measuring equipment, the scatter in the structural response was small. DIC field measurements have previously been limited to solid impacts, but is very well suited for slamming impacts as well.

Many different impact scenarios had to be studied before the experimental drop tests were carried out. A major benefit of the numerical simulations in LS-Dyna was the flexibility in changing the material behaviour, boundaries and impact conditions. The added mass did not have to be specified by the user, but was automatically present during the FSI simulation. The uncertainty of the estimated added mass is thus eliminated in the simulation in LS-Dyna which is a major benefit compared to simplified methods. Some of the physical aspects of the real slamming event, such as cavitation, entrapped air and spray root details, are challenging to include in the numerical code. Without a comparison with experimental tests, it would have been challenging to evaluate which physical effects to include in the simulation. Even though the model simplifies some aspects of the impact, LS-Dyna provides a good prediction of the structural response to slamming.

The theoretical methods provided a reasonable estimation of the structural response of the stiffened panel, but the results were more uncertain than the experimental and numerical methods. Parts of the uncertainty is introduced to the simplified methods because approximate values of added mass, resistance curves, structural stiffness and load histories were applied. Simplified formulations can provide a fast and realistic estimate of the structural response and behaviour for many cases depending on the required level of accuracy. The theoretical methods should be verified with numerical simulations and experimental data, if available.

10.2 Recommendations for Further Work

10.2.1 Numerical Model in LS-Dyna

There are several aspects of the numerical model that can be improved to enhance the complexity of the fluid-structure impacts. The deceleration mechanism of the impactor induced by the ropes is not simulated in LS-Dyna. The deceleration effect could be simulated by attaching damping springs to the plate and activate these at the same time as the ropes would stop the motion of the drop test rig.

In the LS-Dyna software, there are available options for coupling between an incompressible computational fluid dynamics, henceforth CFD, solver and a solid mechanics solver. When the structural solver is coupled with a CFD code, the fluid flow can be modelled with more details. In the current numerical simulations, the plate impacts a calm, free surface. A more realistic representation of the sea water surface should be modelled with irregular waves. Instead of the simplified drop test impacts, the slamming event could be modelled with the more realistic conditions of a breaking wave hitting the structural component. To model the kinematics and behaviour of the breaking slamming wave, a CFD solver is required.

The execution of the drop test experiments in the SLADE-project began in the middle of May. In this thesis, only the results from the hydro-plastic impacts have been included. As the project continues, drop tests with elastic and rigid plates will also be performed. In further work, it would also be interesting to simulate a full-scale unstiffened plate in order to compare the scaling effects with the small model.

10.2.2 Theoretical Methods

The simplified formulation for resistance curves for stiffened plates subjected to lateral loading underestimated the capacity of materials with hardening and bi-axial membrane states. The formulation does not properly account for the strengthening effect from membrane action during the plastic collapse. In future work, the approach could be further developed to also take bi-axial membrane stress states and plastic hardening of the material into account.

The elasto-plastic response of the unstiffened plate has not been estimated with theoretical methods. Neither the resistance curves for unstiffened plates from RP C204 (DNVGL, 2016a) nor the resistance curves from LS-Dyna provided reasonable results for a plate with 0.6 mm plate thickness. The theoretical methods for the unstiffened plate were investigated towards the end of the master thesis, and was not further studied due to limited time.

In addition to the established engineering practice in the RP, other approaches for the estimation of the response to slamming loads could be investigated. Less time-consuming alternatives to the numerical drop tests impact could be simulated in LS-Dyna. These alternatives do not include FSI and ALE formulations, which will reduce the computational time considerably. One method is to apply a triangular load pulse with a given duration and a peak pressure to the plate. Another method is to induce a free oscillation in the plate by applying the impact velocity as an initial velocity field to the plate. The added mass should be added to the density to the plate for both of the simulations. These simplified methods may also be solved in another programming language such as Matlab or Python with numerical integration and plastic theory, but will require more work.

References

Aarsnes, J. (1994). An experimental investigation of the effect of structural elasticity on slamming loads and structural response. Technology Report MT60 A95-0053 602119.00.01, Norwegian Maritime Technology Research Institute A/S, MARINTEK.

Amdahl, J. (2005). *TMR4205 Buckling and Ultimate Strength of Marine Structures*. MTS.

Amdahl, J., Yu, Z., and Sha, Y. (2017). Large inelastic deformation resistance of stiffened panels subjected to lateral loading. *Marine Structures*.

Aquelet, N., Souli, M., and Olovsson, L. (2006). Euler-lagrange coupling with damping effects: Application to slamming problems. *Computer methods in apllied mechanics and engineering*, 195:110–132.

Bereznitski, A. (2001). Slamming: The role of hydroelasticity. *Int. Shipbuild. Progr.*, 48:333–351.

Brett, J. (1998). Numerical modelling of shock wave and pressure pulse generation by underwater explosions. Technical report, Maritime Platform Divisions.

Cheon, J., Jang, B., Yim, K., Lee, H., Koo, B., and Ju, H. (2016). A study on slamming pressure on a flat stiffened plate considering fluid-structure interaction. *Journal of Marine Science and Technology*, 21:309–324.

Cowper, J. and Symonds, P. (1957). Strain-hardening and strain-rate effects in the impact loading of cantilever beams. Technical Report 28, Division of Applied Mathematics, Brown University.

Day, J. (2009). Guidelines for ale modelling in ls-dyna. Technical report, Livermore Software Technology Corporation.

DNVGL (2013). Determination of structural capacity by non-linear structural analysis methods. Technical Report DNV-RP-C208, Det Norske Veritas (DNV).

DNVGL (2014). Dnv-rp-c205 environmental conditions and environmental loads.

DNVGL (2015). Dnv-os-c101 design of offshore steel structures, general - lrfd method.

DNVGL (2016a). Dnv-rp-c204 design against accidental loads.

DNVGL (2016b). Dnvgl-otg-13 prediction of airgap for column stabilised units.

DNVGL (2016c). Dnvgl-otg-14 horizontal wave impact ,load for column stabilised unit draft.

Dynamore (2018). Ls-dyna introductory course. Technical report, Dynamore Nordic.

Faltinsen, O. (1990). *Sea Loads on Ships and Offshore Structures*. Ocean Technology. Cambridge University Press.

Faltinsen, O. (1997). The effect of hydroelasticity on slamming. *Philosophical Transactions: Mathematical, Physical and Engineering Sciences*, 355:575–591.

Faltinsen, O. (1999). Water entry if a wedge by hydroelastic othotropic plate theory. *Journal of Ship Research*, 3:180–193.

Faltinsen, O. (2000). Hydroelastic slamming. *Journal of Marine Science and Technology*, 5:49–65.

Faltinsen, O. (2005). *Hydrodynamics of High-Speed Vehicles*. Cambridge University Press.

Faltinsen, O., Kvålsvold, J., and Aarsnes, J. (1997). Wave impact on a horizontal elastic plate. *Journal of Marine Science and Technology*, 2:87–100.

Hopperstand, O. and Børvik, T. (2017). *Impact Mechanics: Modelling of plasticity and failure with explicit finite element methods*. Structural Impact Laboratory (SIMLAB), Department of Structural Engineering, NTNU.

Kılıçaslan, C., Odacı, I., and Güden, M. (2016). Single- and double-layer aluminum corrugated core sandwiches under quasi-static and dynamic loadings. *Journal of Sandwich Structures and Materials*, 81:667–692.

Kvålsvold, J. and Faltinsen, O. (1995). Hydroelastic modelling of wetdeck slamming on multihull vessels. *Journal of Ship Research*, 39:225–239.

Kvålsvold, J., Faltinsen, O., and Aarsnes, J. (1995). Effect of structural elasticity on slamming wetdecks on multihull vessels. *Proceedings of PRADS'95, Korea. Society of Naval Architects of Korea*, pages 1684–1699.

Langseth, M., Børvik, T., and Aune, V. (2016). *Impact Mechanics: An Introduction to Blast Mechanics.* Structural Impact Laboratory (SIMLAB), Department of Structural Engineering, NTNU.

Larsen, C. (2014). *TMR4180 Marin Dynamikk.* Akademika.

Lian, G., Økland, O., and Vestbøstad, T. (2015). Impact loads from drop test of a circular section with 42 force transducers. Technical Report OMAE2015-41491, ASME 2015 34th International Conference on Ocean, Offshore and Arctic Engineering.

LSTC (2001). Ls-dyna support. `http://www.dynasupport.com/tutorial`. Accessed: 2017-10-13.

LSTC (2003). Ls-dyna support - eulerian method; basics. `http://www.dynasupport.com/howtos/material/eulerian-method-basics`. Accessed: 2018-02-13.

Luo, H., Wang, H., and Soares, C. (2012). Numerical and experimental study of hydrodynamic impact and elastic response of one free-drop wedge with stiffened panels. *Ocean Engineering*, 40:1–14.

Megson, T. (2005). *Structural and Stress Analysis.* Butterworth-Heinemann, 2 edition.

Norman, J. (1971). A theoretical study of the dynamic plastic behavior of beams and plates with finite-deflections. *International Journal of Solids and Structures*, 7:1007–1029.

Norsok Standard (2013). N004 design of steel structures.

Seo, B., Truong, D., Cho, S., Kim, D., Park, S., and Shin, H. (2018). A study on accumulated damage of steel wedges with dead-rise 10° due to slamming loads. *International Journal of Naval Architecture and Ocean Engineering*, pages 1–9.

Skjeggedal, E. (2017). Wave-in-deck forces and response of semi-submersibles. Master's thesis, NTNU.

SLADE (2018). Slamming loads in structural design (slade): Hydro-plastic drop test of plates. Unpublished technical report, SINTEF Ocean.

Steen, S. (2014). *Lecture Notes: Experimental Methods in Marine Hydrodynamics.* Faculty of Engineering Science and Technology, NTNU.

Stenius, I., Rosén, A., Battley, M., and Allen, T. (2013). Experimental hydroelastic characterisation of slamming loaded marine panels. *Ocean Enginering*, 74:1–15.

Stenius, I., Rosén, A., and Kuttenkeuler, J. (2011). Hydroelastic interaction in panel-water impacts of high-speed craft. *Ocean Enginering*, 38:371–381.

Von Kármán, T. (1929). The impact on seaplane floats during landing. *NACA Tech Note*, 321:309–313.

Wagner, H. (1932). Über stoß- und gleitvorgänge an der oberfläche von flüssigkeiten. *ZAMM*, 12:193–215.

Zhang, K., Holmedal, B., Hopperstad, O., and Dumoulin, S. (2014). Use of plane-strain tension and shear tests to evaluate yield surfaces for aa1050 aluminium sheet. *Materials Science Forum*, 794-796:596–601.

Zhao, R. and Faltinsen, O. (1993). Water entry of two-dimensional bodies. *Journal of Fluid Mechanics*, 246:593–612.

Appendix A

Convergence tests for stiffened plate

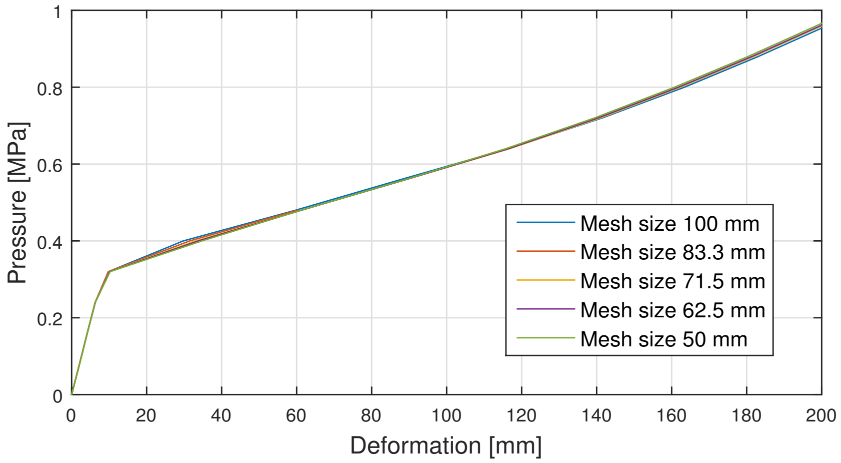

Figure A.1: Convergence test for static analysis of stiffened plate

Appendix B

Transformation Factors For Beams

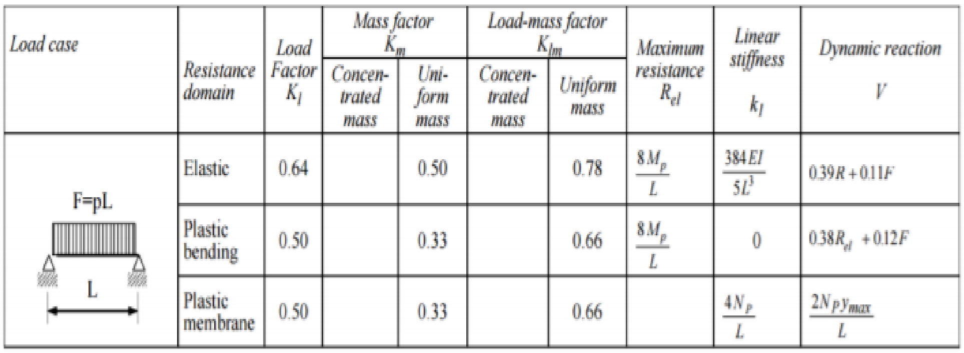

Load case	Resistance domain	Load Factor K_l	Mass factor K_m		Load-mass factor K_{lm}		Maximum resistance R_{el}	Linear stiffness k_l	Dynamic reaction V
			Concentrated mass	Uniform mass	Concentrated mass	Uniform mass			
F=pL L	Elastic	0.64		0.50		0.78	$\frac{8M_p}{L}$	$\frac{384EI}{5L^3}$	$0.39R+0.11F$
	Plastic bending	0.50		0.33		0.66	$\frac{8M_p}{L}$	0	$0.38R_{el}+0.12F$
	Plastic membrane	0.50		0.33		0.66		$\frac{4N_P}{L}$	$\frac{2N_p y_{max}}{L}$

Figure B.1: Transformation factors for a simply supported beam in SDOF system

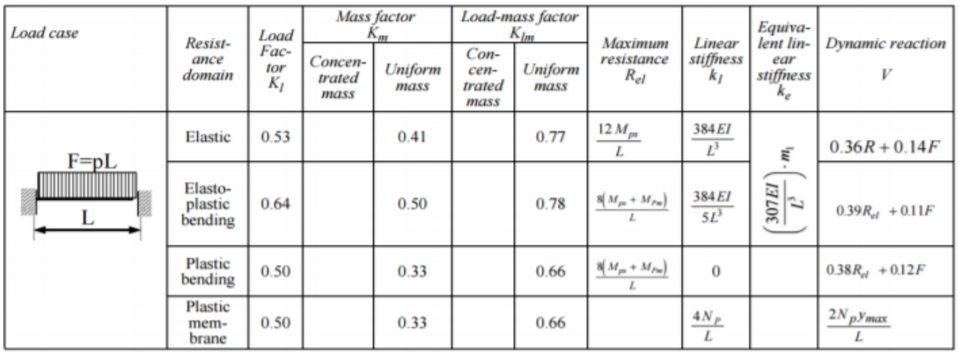

Load case	Resistance domain	Load Factor K_l	Mass factor K_m		Load-mass factor K_{lm}		Maximum resistance R_{el}	Linear stiffness k_l	Equivalent linear stiffness k_e	Dynamic reaction V
			Concentrated mass	Uniform mass	Concentrated mass	Uniform mass				
F=pL L	Elastic	0.53		0.41		0.77	$\frac{12M_{ps}}{L}$	$\frac{384EI}{L^3}$	$\left(\frac{307EI}{L^3}\right)\cdot m_l$	$0.36R+0.14F$
	Elasto-plastic bending	0.64		0.50		0.78	$\frac{8(M_{ps}+M_{pm})}{L}$	$\frac{384EI}{5L^3}$		$0.39R_{el}+0.11F$
	Plastic bending	0.50		0.33		0.66	$\frac{8(M_{ps}+M_{pm})}{L}$	0		$0.38R_{el}+0.12F$
	Plastic membrane	0.50		0.33		0.66		$\frac{4N_P}{L}$		$\frac{2N_p y_{max}}{L}$

Figure B.2: Transformation factors for a clamped beam in SDOF system

Appendix C

Stress-strain curves for steel S355

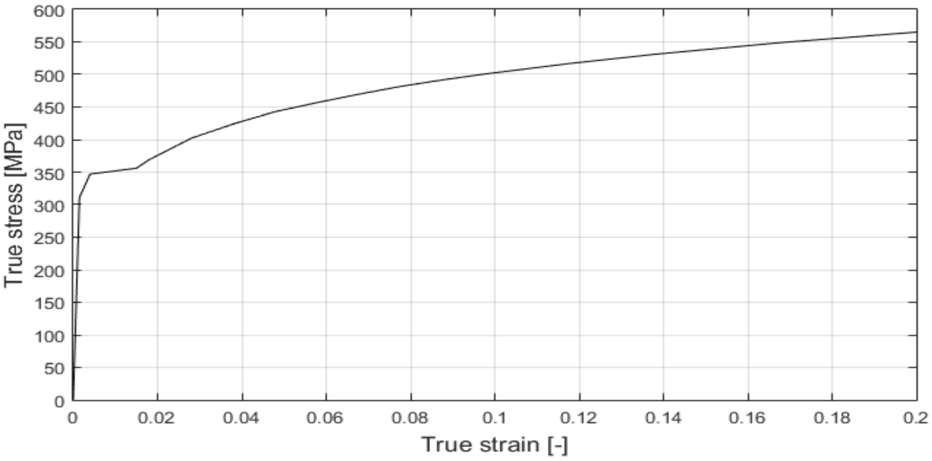

Figure C.1: Stress-strain curve for steel S355 according to DNV C208 t ≤ 16 mm

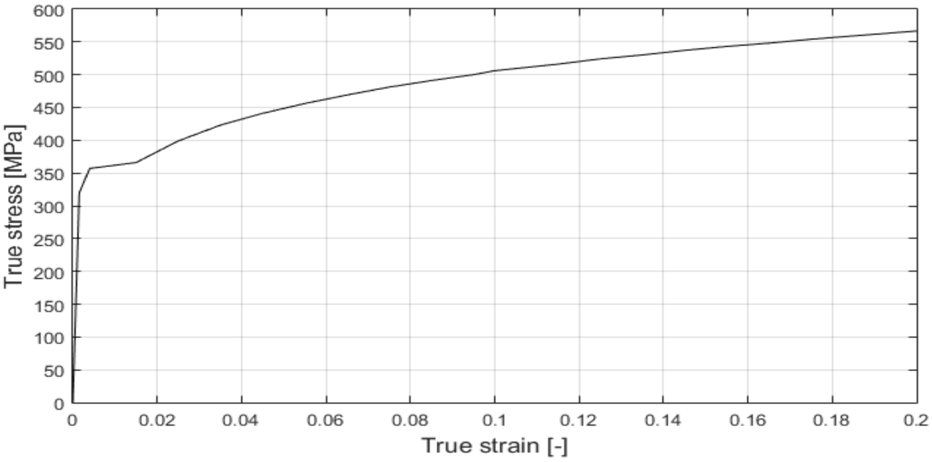

Figure C.2: Stress-strain curve for steel S355 according to DNV C208 16 < t ≤ 40 mm

Appendix D

Parameter tests for unstiffened plate

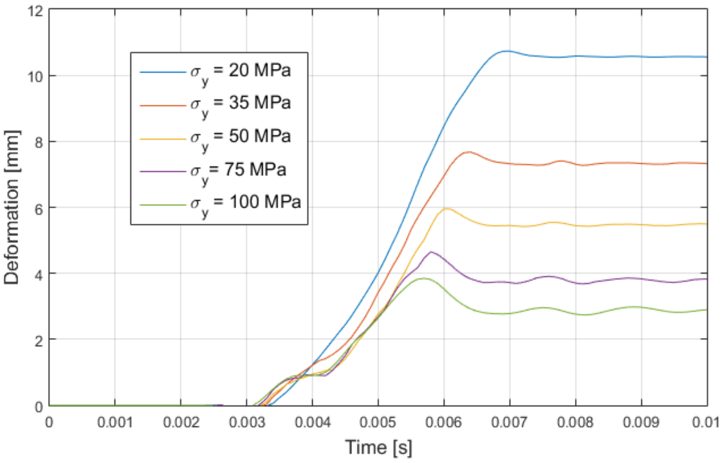

(a) Maximum deflection

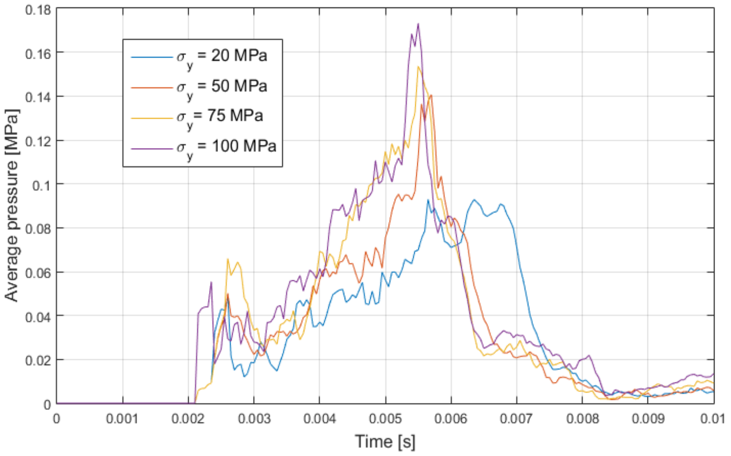

(b) Average pressure on plate

Figure D.1: Variation of yield stress for aluminium plate with plate thickness t = 2 mm 4° impact angle

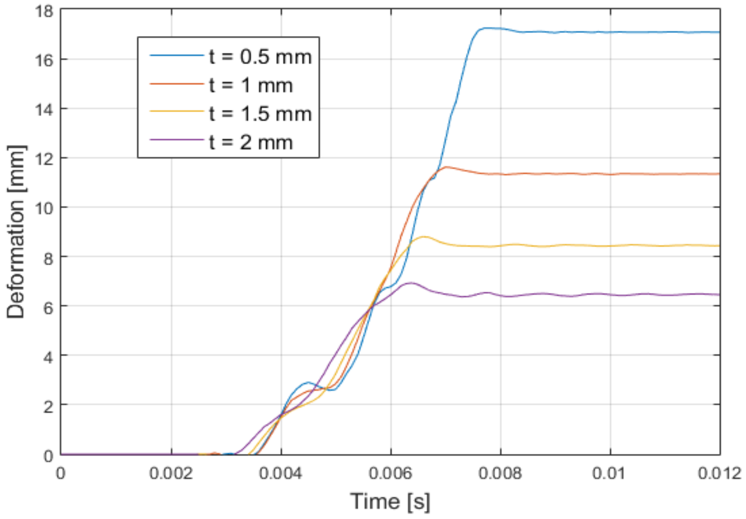

(a) Maximum deflection

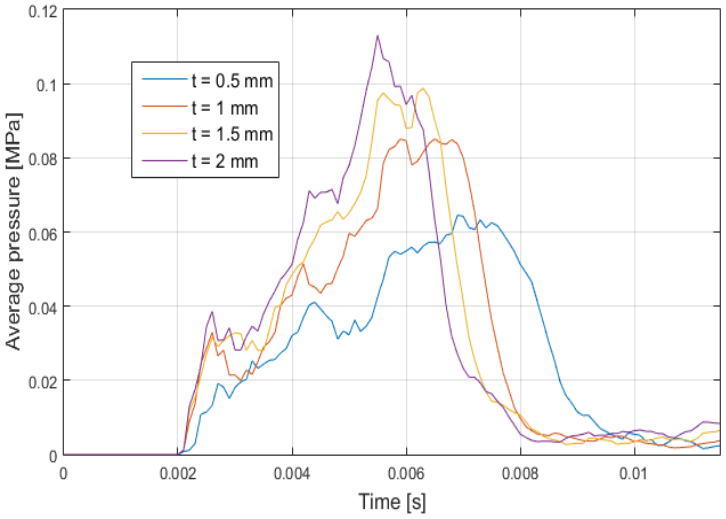

(b) Average pressure on plate

Figure D.2: Variation of plate thickness for aluminium plate with σ_y = 40 MPa and 4° impact angle

Appendix E

Tensile test specimens of A1050 H111

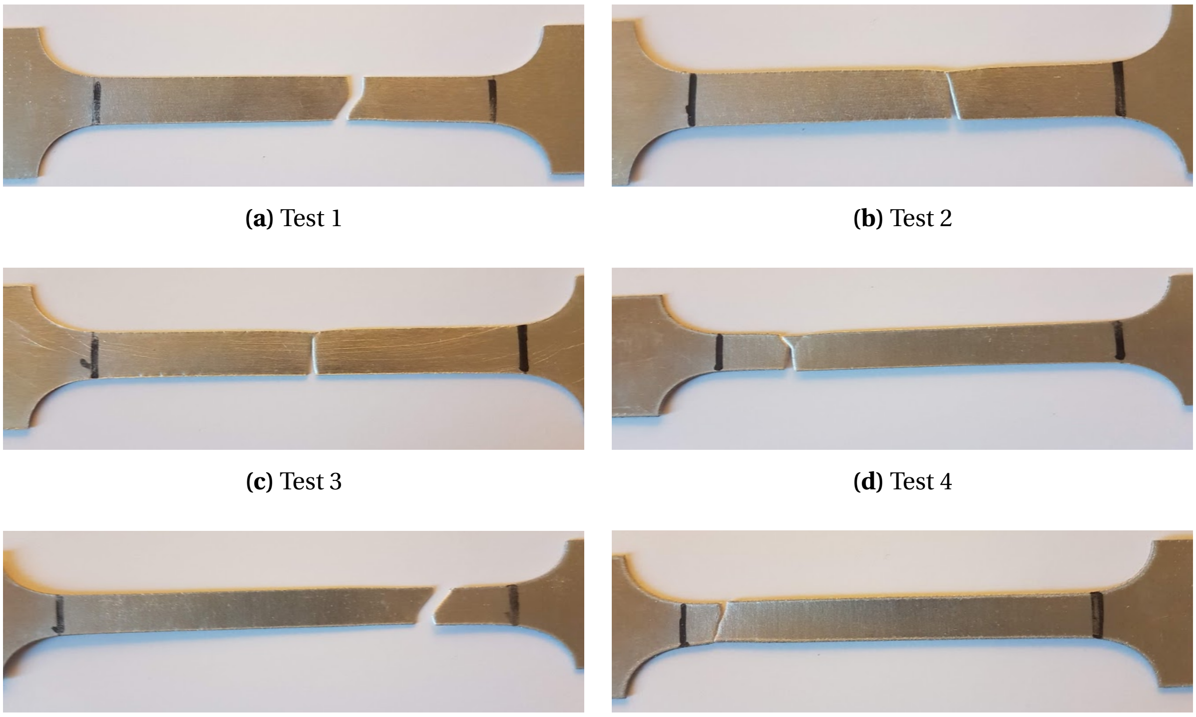

(a) Test 1

(b) Test 2

(c) Test 3

(d) Test 4

(e) Test 5

(f) Test 6

Figure E.1: Results from quasi-static tensile test from A1050 H111 Material 1

Appendix F

Deformation profiles from LS-Dyna and Mitutoyo

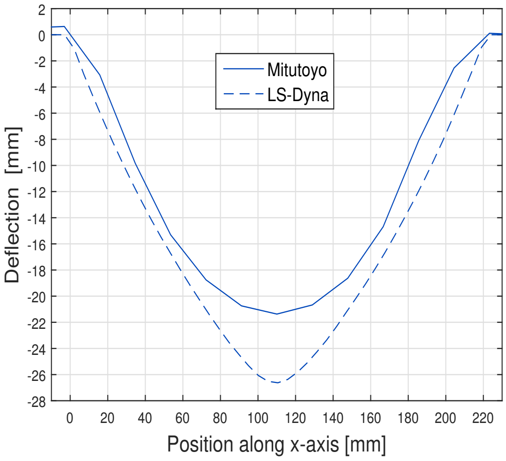

(a) Test 3: Drop height 77.8 cm and β=0

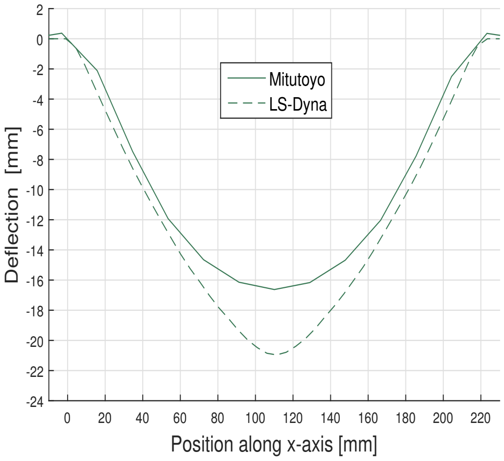

(b) Test 4: Drop height 44.3 cm and β=0

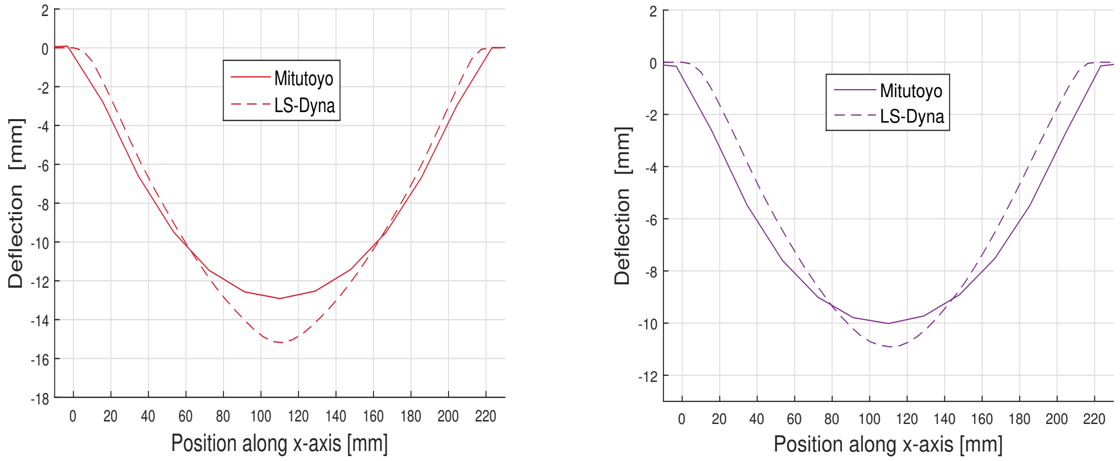

(c) Test 6: Drop height 22.2 cm and β=0

(d) Test 7: Drop height 11.8 cm and β=0

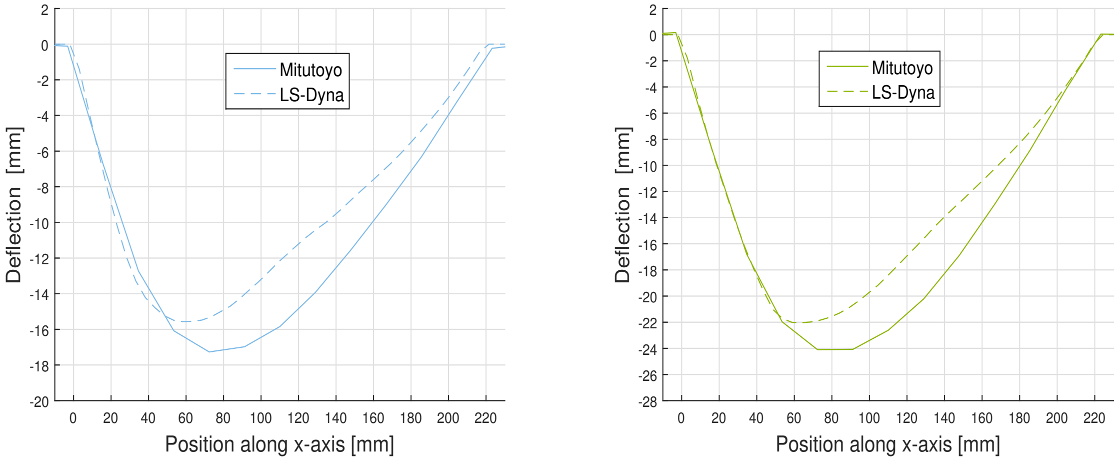

(e) Test 8: Drop height 44.4 cm and β=4

(f) Test 10: Drop height 84.5 cm and β=4

Figure F.1: Deformation profiles in the xz-plane from simulations in LS-Dyna and measurements by Mitutoya